AN ATMOSPHERIC CORRECTION ALGORITHM FOR HYPERSPECTRAL IMAGERY

by

Lee C. Sanders

Bachelor of Science Rochester Institute of Technology (1994)

A dissertation submitted in partial fulfillment
of the requirements for the degree of Ph.D.
in the Chester F. Carlson Center for Imaging
Science in the College of Science of the
Rochester Institute of Technology

September 1999

Signature of the Author____

Accepted by ____
Coordinator, Ph.D. Degree Program

CHESTER F. CARLSON
CENTER FOR IMAGING SCIENCE
COLLEGE OF SCIENCE
ROCHESTER INSTITUTE OF TECHNOLOGY
ROCHESTER, NY

CERTIFICATE OF APPROVAL

Ph.D. DEGREE DISSERTATION

The Ph.D. Degree of Dissertation of Lee C. Sanders
has been examined and approved by the
dissertation committee as satisfactory for the
dissertation requirement for the
Ph.D. degree in Imaging Science

Dr. John Schott, Dissertation Advisor

Dr. Roger Easton

Dr. Zoran Ninkov

Dr. Russell Kraus

1 September 1999

DISSERTATION RELEASE PERMISSION
ROCHESTER INSTITUTE OF TECHNOLOGY
COLLEGE OF SCIENCE
CHESTER F. CARLSON CENTER FOR IMAGING SCIENCE

Title of Thesis: An Atmospheric Correction Technique for
Hyperspectral Imaging

I, Lee C. Sanders, hereby grant permission to the Wallace Memorial Library of R.I.T. to reproduce my thesis in whole or in part. Any reproduction will not be for commercial use or profit.

Signature:____

Date: 1 September 1999

AN ATMOSPHERIC CORRECTION TECHNIQUE
FOR
HYPERSPECTRAL IMAGERY

by Lee C. Sanders

Submitted to the Chester F. Carlson Center for Imaging Science
in the College of Science
in partial fulfillment of the requirements
for the Ph.D. Degree
at the Rochester Institute of Technology

ABSTRACT

Radiometrically calibrated hyperspectral imagery contains information relating to the material properties of a surface target and the atmospheric layers between the surface target and the sensor. All atmospheric layers contain well-mixed molecular gases, aerosol particles, and water vapor, and information about these constituents may be extracted from hyperspectral imagery by using specially designed algorithms. This research describes a total sensor radiance-to-ground reflectance inversion program. An equivalent surface-pressure depth can be extracted using the NLLSSF technique on the 760nm oxygen band. Two different methods (APDA, and NLLSSF) can be used to derive total columnar water vapor using the radiative transfer model MODTRAN 4.0. Atmospheric visibility can be derived via the NLLSSF technique from the 400-700nm bands or using a new approach that uses the upwelled radiance fit from the Regression Intersection Method from 550nm-700nm. A new numerical approximation technique is also introduced to calculate the effect of the target surround on the sensor-received radiance. The recovered spectral reflectances for each technique are compared to reflectance panels with well-characterized ground truth.

Acknowledgements

I wish to thank all of my family, both the Sanders' and the Haywards for their unwavering support during all these college years. I thank Dr. John Schott for believing in me enough to take me on as one of his Ph.D. students, for his willingness to share and teach his extensive technical expertise, and for his sense of humor. A hearty thank you to my associate Rolando Raqueno who wrote the IDL routines for the MODTRAN 4.0 LUT generator, with whom I have worked with these last five years on different contracts, and who has put up with me constantly barging into his office. Thanks to Scott Brown who has endured my constant questioning on MODTRAN and grills a really mean smoked pork. Thank you to Tim Gallagher and Bryce Nordgren, my associates in developing the MISI; I learned a lot from both of you. Thank you to Dr. Robert Green, Dr. Daniel Schläepfer, and Dr. Chris Borel for sharing your algorithms and your time so I could include them in this research project. Thank you to Lex Berk and Dr. Steven Adler-Golden for helping me to understand MODTRAN better and having the patience to return my numerous e-mails. Thanks to Jim Chetwynd for all the help with MODTRAN and helping me with the Mie scattering codes. A very special thank you to CIS system administrators Sue Michel and Bob Krzaczek for keeping my computers available and running optimally and answering all my stupid Unix questions. Thank you Sue Chan for being such a warm, charming person and a treasured friend (who always made sure I took care of things like register for classes). Finally, thank you to all the students, faculty, and staff of the CIS for making it such a fun and wonderful place.

Dedication

I wish to dedicate this research to my loving and patient wife, Vivian, who has sacrificed as much as I have in order to produce this scientific work.

TABLE OF CONTENTS

Table of Figures

1. Introduction

For many years, the astronomical community has used spectroscopy to determine the chemical composition of stellar objects. The atomic and molecular constituents of stars, planets, and nebulae have been revealed by their unique spectra that in turn are due to their different properties of absorption and emission of electromagnetic energy. The spectral signatures of these elements arise from their electronic, vibrational, and rotational transitions. This information is also being extracted from air and space-borne instruments to access properties about earth's surface structure and the composition of the atmosphere.

The analysis of stellar spectra is relatively straightforward because stars are composed almost exclusively of elements in atomic form. Any molecules have dissociated due to the extremely high temperatures. The spectra thus exhibit the well-defined narrow absorption lines of their constituent elements. Based on the same spectral features, laboratory analysis can be used to determine elemental constituents of a material. Spectra may be scanned at high resolution (i.e., narrow wavelength intervals) to measure the fine structure. Because these spectra are well documented, chemical analysis is simple and repeatable.

It would be useful if the controlled approach of spectroscopy could be applied to airborne or space-based imaging spectrometry of the earth. The calculus of atmospheric characterization and identification of the constituents of ground objects would be simplified. Unfortunately, this calculation is not trivial. The earth's atmosphere is a complex mix of molecular and larger sized compounds that are in flux spatially and temporally. To determine the scene content of an image with confidence, the atmosphere must be characterized to sufficient accuracy to obtain ground reflectance units to a half a reflectance unit or to estimate temperature parameters to a tenth of a Kelvin.

To date, the best methods for extracting atmospheric information rely heavily on the combination of ground-truth measurements of targets in the scene and ground-based atmospheric measurements (for aerosol and water vapor determination) made with sun-photometers and radiosondes. These measurements may be made only on days with high visibility. These truth data allows an atmospherically corrected radiance image to be produced. The atmospheric data so gleaned may be useful to climatologists for predicting and characterizing weather patterns, to environmentalists for air pollution studies, and to the remote sensing scientist to remove the effects of the atmosphere from the image in order to classify ground targets correctly.

Obtaining ground truth is an expensive, laborious, and time-consuming task. For physical and economic reasons, few multispectral or imaging spectrometer missions measure actual conditions simultaneously with image acquisition. To fill this computational void, algorithms have been developed to extract atmospheric data directly from the spectra of individual pixels in the hyperspectral image. All such algorithms use some form of radiative transfer model of the atmosphere. These programs make certain assumptions about important radiometric parameters that may result in gross errors in the attributes of the corrected image.

The purpose of this research is to further contribute to the precision of atmospheric characterization by developing a total inversion algorithm that derives the estimated ground reflectance of an object from the calibrated radiance at the sensor. This algorithm utilizes existing atmospheric correction techniques, is radiometrically correct, is modular so that additional techniques may be added, and is more rigorous in its treatment of radiometric parameters than previous methodologies. Presently, there are different methods that are considered to be "state of the art" for hyperspectral information extraction: the NonLinear Least Squares Spectral Fit method for surface-pressure depth, columnar water vapor, and atmospheric visibility described by Green, (1989), and the Atmospheric Pre-corrected Differential Absoprtion method for columnar water vapor developed by Borel and Schläepfer, (1996). These algorithms have been tested in well-characterized remote sensing environments and both are incorporated into the new atmospheric correction algorithm.

In addition to the aforementioned methods, a new atmospheric visibility algorithm is added which uses the atmospheric path radiance computed by the Regression Intersection Method. This algorithm requires fewer computations (and thus shorter computation times) than NLLSSF and does not require any user estimate of atmospheric visibility. Also, a new method to compute the target surround contribution to upwelled radiance has been developed which utilizes the calculated aerosol phase function parameters inside MODTRAN 4.

2. Background

2.1 A History of Hyperspectral Imaging

The advent of modern imaging spectrometry for earth remote sensing began at the Jet Propulsion Laboratory about 1980. Prior to this time, remote sensing was limited to the analysis of photographs of the earth based on a few algorithmic approaches to extract quantitative data. To a large extent, the early efforts to develop sophisticated analytical techniques were hampered by the limits to computing power and by the existing hardware technologies. The first device capable of obtaining calibrated spectral information was the Thematic Mapper on Landsat 4 (1982) which covered seven spectral bands in the visible, infrared, and far-infrared regions of the spectra. The TM system delivered higher ground resolution, greater separation between spectral bands, and better radiometric accuracy than previous space-based instruments (Kastner, 1985).

It was soon apparent to image analysts that the fuller spectral coverage and narrower spectral bandwidths revealed much more information about the scene than previous designs. The green (0.52-0.60µm) and red (0.63-0.69µm) bands could be used to distinguish differences in vegetation and chlorophyll absorption better than ever before. Light in the blue-green band penetrates water and therefore this band is used for oceanographic and hydrologic studies; data in the SWIR (1.6µm) band could be used to differentiate snow and clouds, while spectra in the 2.2µm band can be used to differentiate different types of soil and rock. Thermal information from band 6 spanned 10.4µm to 12.5µm; this band provided information about vegetation stress as well as geologic and man-made structures (Kastner, 1985).

The success of the Landsat program spawned the further development of imaging spectrometry culminating with the Shuttle Multispectral Infrared Spectrometer in 1981. SMIRR acquired data over a 100-km wide ground track in 10 channels, three of which had narrow bandwidths of 10nm located in the vicinity of 2.35 µm. They allowed the first spaceborne identification of kaolinite and limestone by discriminating the unique absorption characteristics of those minerals (Goetz, 1982).

Airborne Imaging Spectrometer (AIS)

The next phase in imaging spectrometry development was the AIS (Figure 2.1-1). This instrument was designed explicitly for multispectral infrared imaging and used a 32x32 element HgCdTe detector array with 10-bit quantization. The resolution of the spectrum was 9.3nm in the 1.2µm - 2.4 µm range (La Baw, 1987). Results obtained during terrain overflights indicated significant geologic information potential. The spectra were sampled sufficiently finely for analysts to identify spectra of specific minerals for unambiguous classification. At that time, atmospheric models were not available so analysts used running averages of the acquired data (over all pixels); the spectra were divided by this mean value which was an estimate of the atmospheric/solar continuum. The result yielded a sampled spectrum with sufficient resolution for classification.

The early successes of AIS enabled NASA to upgrade the instrument (AIS II) with a 64x64 element HgCdTe array that extended the spectral range into the visible region of the spectra from 0.8 - 2.4 µm. AIS images definitely distinguish the different radiometric characteristics of ground targets at altitude, but the performance was limited by its 7.3° FOV, low spatial resolution, and the fact that it was not radiometrically calibrated.

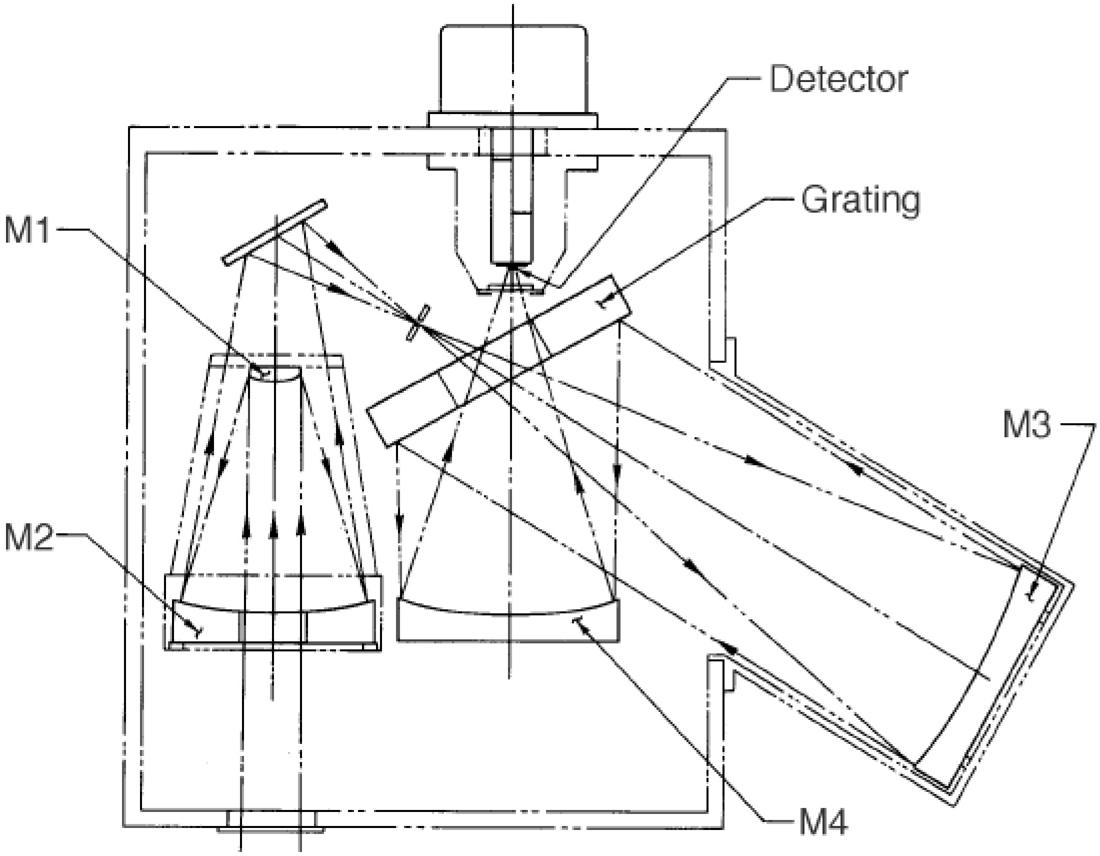

Figure 2.1-1. Internal schematic of the AIS

The Airborne Visible/Infrared Imaging Spectrometer (AVIRIS)

The success of AIS encouraged a demand for upgraded instrumentation to improve mineral identification from spectral signatures. Further advances in infrared detector and scanner designs led to the development of the prototype airborne VIS/NIR imaging spectrometer, which is identified by its acronym AVIRIS (Figure 2.1-2). While AIS was built as an engineering testbed to demonstrate that imaging spectrometers could acquire useful scientific data, AVIRIS was proposed as a facility that would generate fully calibrated data to stimulate development of data utilization and analysis methods (Vane, 1993). The emphasis had dramatically shifted from proving the viability of image spectrometry to creating a scientific distribution resource with high-quality calibrated data.

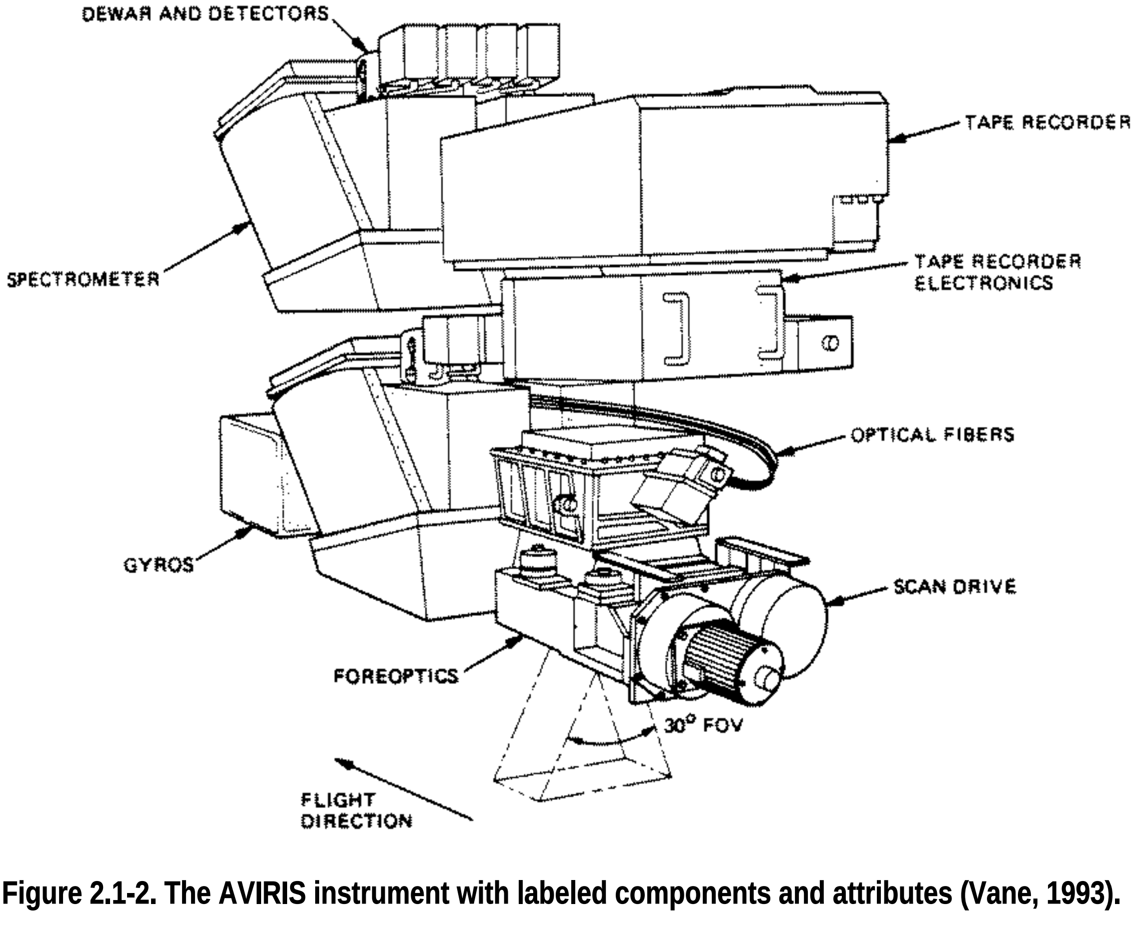

Figure 2.1-2. The AVIRIS instrument with labeled components and attributes (Vane, 1993).

AVIRIS includes a modified Kennedy-type optical scanner (Vane, 1993) fitted with custom scanning and relay optics. The focal plane consisted of six 200µm diameter anti-reflection-coated optical fibers connected to four spectrometers. The design gives greater area coverage and spatial, spectral, and radiometric resolution. The Airborne Visible/Infrared Imaging Spectrometer, in operation since 1987, utilizes detectors based on both silicon (for visible light) and indium antimodide arranged in a line array to cover the spectral region from 0.41µm to 2.45µm in 224 channels with a resulting bandwidth of 0.010µm. NIST-traceable standards and state-of-the-art field equipment were used for in-flight calibration. AVIRIS was designed to fly aboard NASA's ER-2 aircraft at an altitude of 20 km, thus generating an GIFOV of 20 meters and swath width of 12 km (Porter, 1987).

An AVIRIS hyperspectral image is displayed somewhat differently than the typical 2-dimensional RGB spatial image. The data output is in the form of an image cube; two axes of the 3-D data set are spatial, the third is spectral. Inherent in the spectral data is information about the composition of the ground target and the atmosphere between the sensor and target. In fact, the spectral sampling for AVIRIS was made fine enough to detect shifts in the chlorophyll spectrum of the order of 0.010 to 0.040 µm at 0.7µm and resolve spectral features as narrow as those found in minerals such as the kaolinite doublet at 2.2µm.

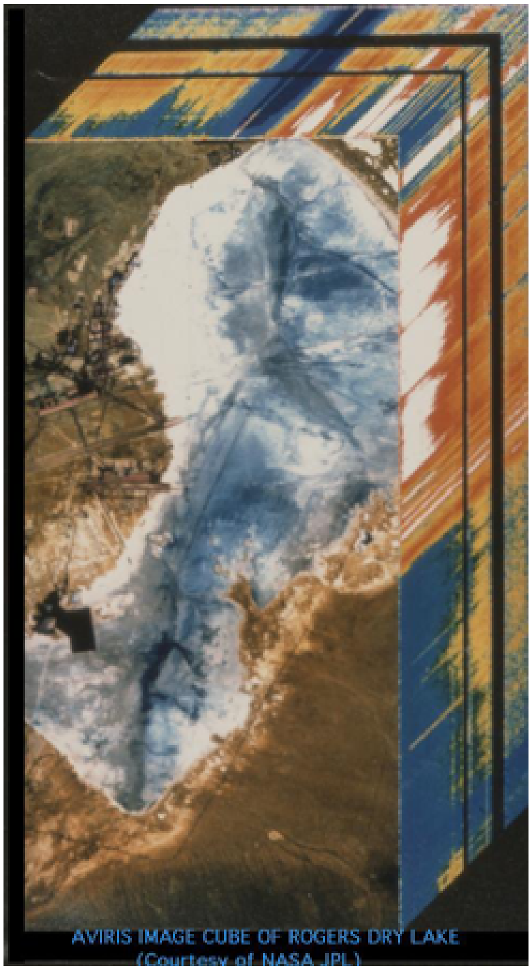

Figure 2.1-3. An AVIRIS image cube that shows spatial and spectral dimensions.

Imaging spectrometer data from AVIRIS has been applied to many other uses since its acceptance by environmental scientists. The research communities in atmospheric science, botany, hydrology, oceanography and remote sensing are applying this new imaging tool to gain more information about the world.

The Hyperspectral Digital Imagery Collection Experiment (HYDICE)

The most advanced hyperspectral imaging spectrometer developed to date is the Hyperspectral Digital Imagery Collection Experiment sensor (HYDICE) that was designed to evaluate the utility of imaging spectroscopy in the area of civil applications (Rickard, 1993). Specific applications include:

Environment - pollution detection

Geology - mineral detection and classification, surface materials, major rock types, altered rocks

Hydrology - water quality, point and no point pollution

Archaeology - further characterization of known area, localize dig

Agriculture - type-Structure, texture, moisture of soils

Forestry - vegetation type mapping, quantification of biomass, stress detection

Oceanography - bathymetry, mapping littoral areas, water characteristics

Marine biology - characterizing surface environment

Endangered species - characterizing known environment

The sensor is a nadir-viewing pushbroom imaging spectroradiometer with a cryogenically cooled InSb focal-plane array (Figure 2.1-4). It has a rather narrow ground swath of one kilometer at its designed operating altitude of six kilometers; the linear dimension of a ground sample (pixel size) is one to four meters depending on sensor altitude. The spectrum is sampled contiguously from 0.40 to 2.5 microns with spectral channels of nominal width 10nm. The most recently reported signal-to-noise ratio was approximately 300 in the visible spectrum and close to 100 in the NIR @ 5% reflectance, which is very close to AVIRIS. Major improvements in spatial resolution, signal-to-noise ratio, and radiometric accuracy make HYDICE an ideal instrument for determining the applicability of hyperspectral imaging to the civil and military arenas. Hyperspectral imaging has advanced to the state where development is not primarily for testbed instrumentation, but is now for evaluating the use of the data and building operational systems (Rickard, 1993).

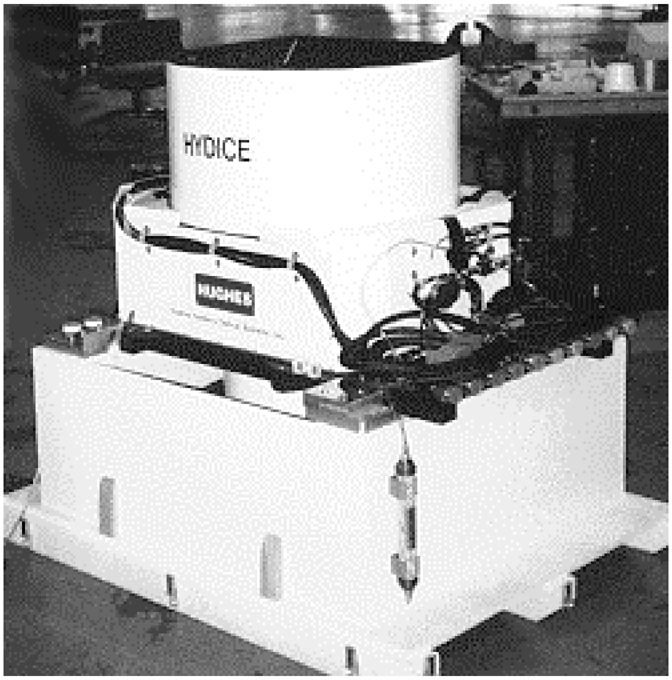

Figure 2.1-4. The HYDICE instrument

The Modular Imaging Spectrometer Instrument (MISI)

This research will use the latest in available technology to acquire the hyperspectral data needed to study the atmosphere. The Digital Imaging and Remote Sensing Group at RIT has constructed an imaging spectrometer called the Modular Imaging Spectrometer Instrument (MISI, Figure 2.1-5) which is a line scanner with a 6” rotating mirror coupled to a Cassegrain telescope of focal ratio 3.3. Two 0.5mm square silicon detectors for the measurements in the broad-band visible spectrum and two 1.5mm fiber optics are placed at the primary focal plane to give a GIFOV of 0.3 m and 1.0 m respectively at 0.3 km of altitude. The fibers lead to two separate 32-channel spectrometers to cover the EM spectrum from 0.410µm to 1.020µm in 0.010µm spectral bands. A pyramid mirror diverts some photons from the primary focal plane to five HgCdTe detectors for the long-wave infrared region; secondary focal planes will be available in the SWIR and MWIR for future use (Feng, 1995). An on-board calibration system consisting of two blackbodies for the LWIR and a tungsten source for the visible completes this imaging system for gathering absolute radiometrically calibrated data for remote sensing applications.

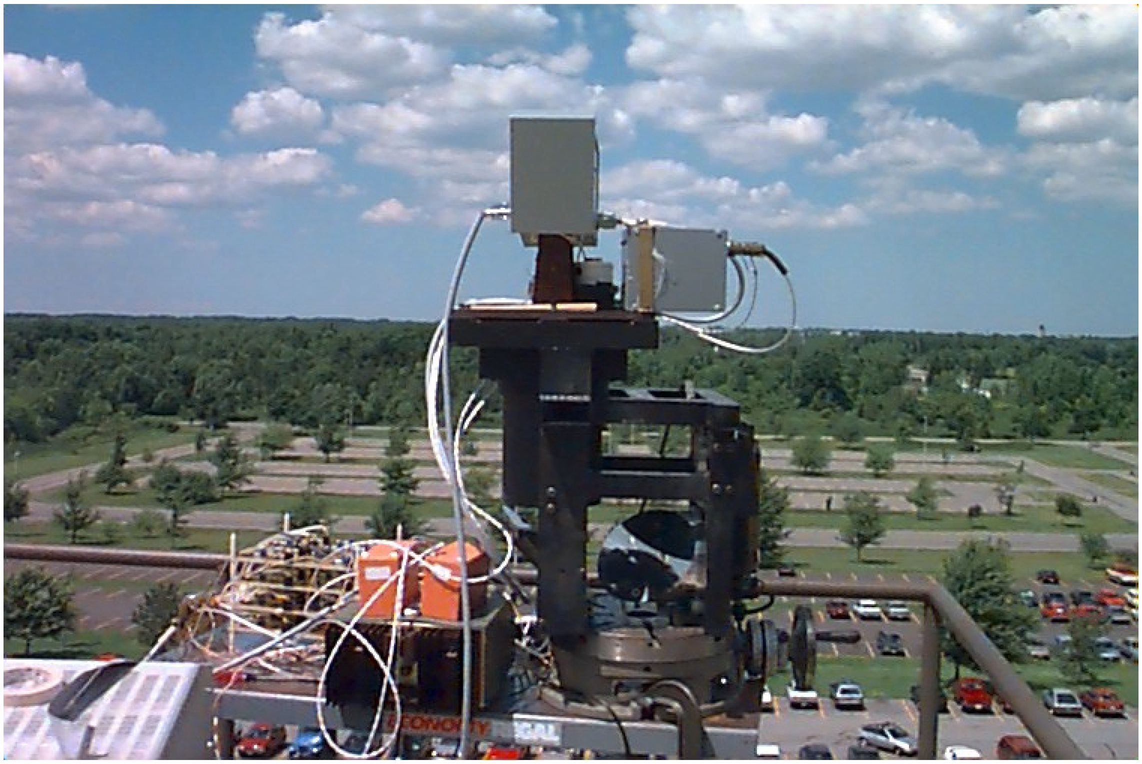

Figure 2.1-5. The Modular Imaging Spectrometer Instrument (MISI)

2.2 Information Extraction from Hyperspectral Data

Before delving too deeply into the technical aspects of imaging spectrometry, the definition of hyperspectral imaging must be clear. Devices that collect multichannel, contiguous, narrow-band imagery from the visible to the infrared portion of the electromagnetic spectrum are generally referred to as "hyperspectral" sensors. In "ultraspectral" imaging, the bands cover a similar range but are extremely narrow (on the order of 1-2nm in the visible and near infrared). In "multispectral" imagery, the bandwidths typically are tens of nanometers wide and not necessarily contiguous. An example of a hyperspectral sensor system is AVIRIS with 224 spectral bands, each with a 10nm bandwidth, and covering the spectral range is 0.4µm to 2.4µm (Figure 2.2-1).

The power of the hyperspectral sensor rests in its ability to record an electromagnetic profile with fine spectral resolution at each pixel within its field of view. Wavelength-dependent characteristics in the reflectance or absorption spectra reveal important information about the chemical make-up and types of atomic and molecular bonding in the material being targeted (Goetz, 1985). Spectral features are the direct result of electronic and/or vibratory orbital energy transitions at the atomic and/or molecular level due to photon absorption. Thus, the combination, placement, and relative strength of the absorption feature(s) can be exploited for surface material identification, evaluation, and analysis of internal processes.

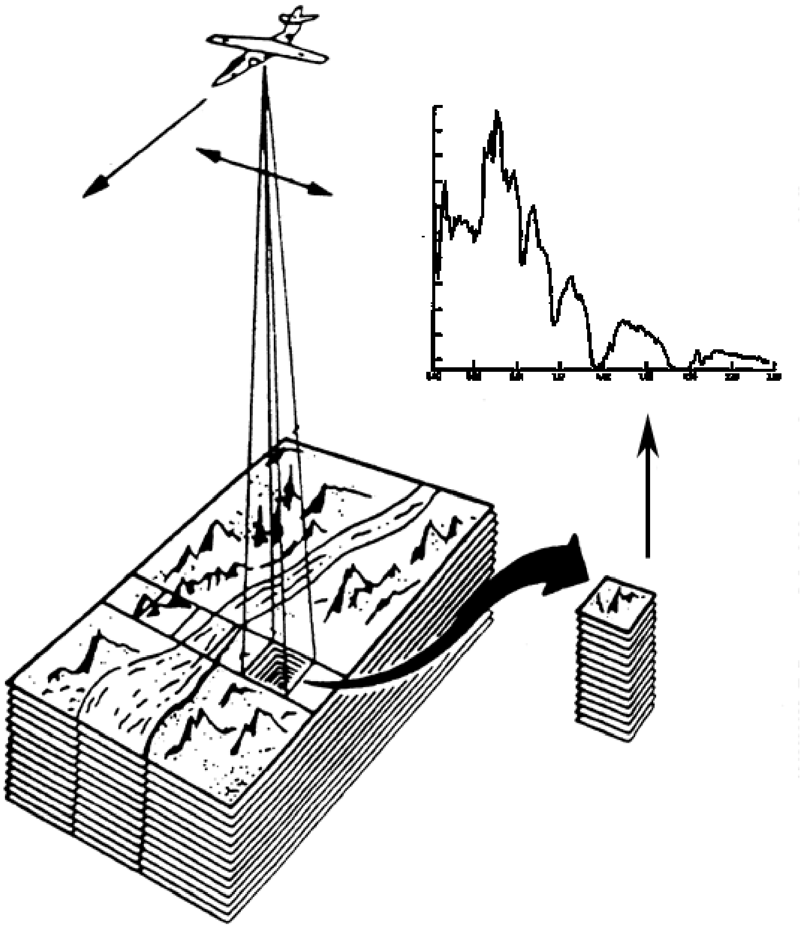

Figure 2.2-1. Aerial spectral sampling of an AVIRIS scene showing the ground field of view, spectral pixel samples, and sample spectrum.

Absorption is not the only determinant of the shape of the reflectance spectrum of a material. Photon scattering, particle size, and porosity effects can cause linear and nonlinear mixes of reflectance information. The path of a photon may resemble a random walk; a certain percentage of photons are absorbed and the remainder are scattered in random directions by each particle center. Larger particle grains have longer optical paths resulting in a higher probability of absorption (Clark, 1984). With smaller grains, there are proportionally more surface reflections per unit area compared to large grain sizes. Thus, as the grain size decreases, the reflectance increases.

Spectral contrast is maximized (*i.e.* the absorption feature is more apparent) when the particle diameter and the optical depth are approximately equal. Contrast depends strongly on the difference between the absorption maximum and the absorption of the adjacent continuum (Pieters, 1993). The continuum is defined as the “background absorption” onto which the other absorption features are superimposed. For example, in Figure 2.2-2, the 2.2µm absorption doublet is clearly seen against the continuum in the spectrum of the mineral "kaolinite". Because of the complex, nonlinear scattering process, weak features not normally seen in transmittance are sometimes enhanced in absorption and consequently spectral reflectance spectroscopy becomes valuable as a diagnostic tool for target chemical make-up.

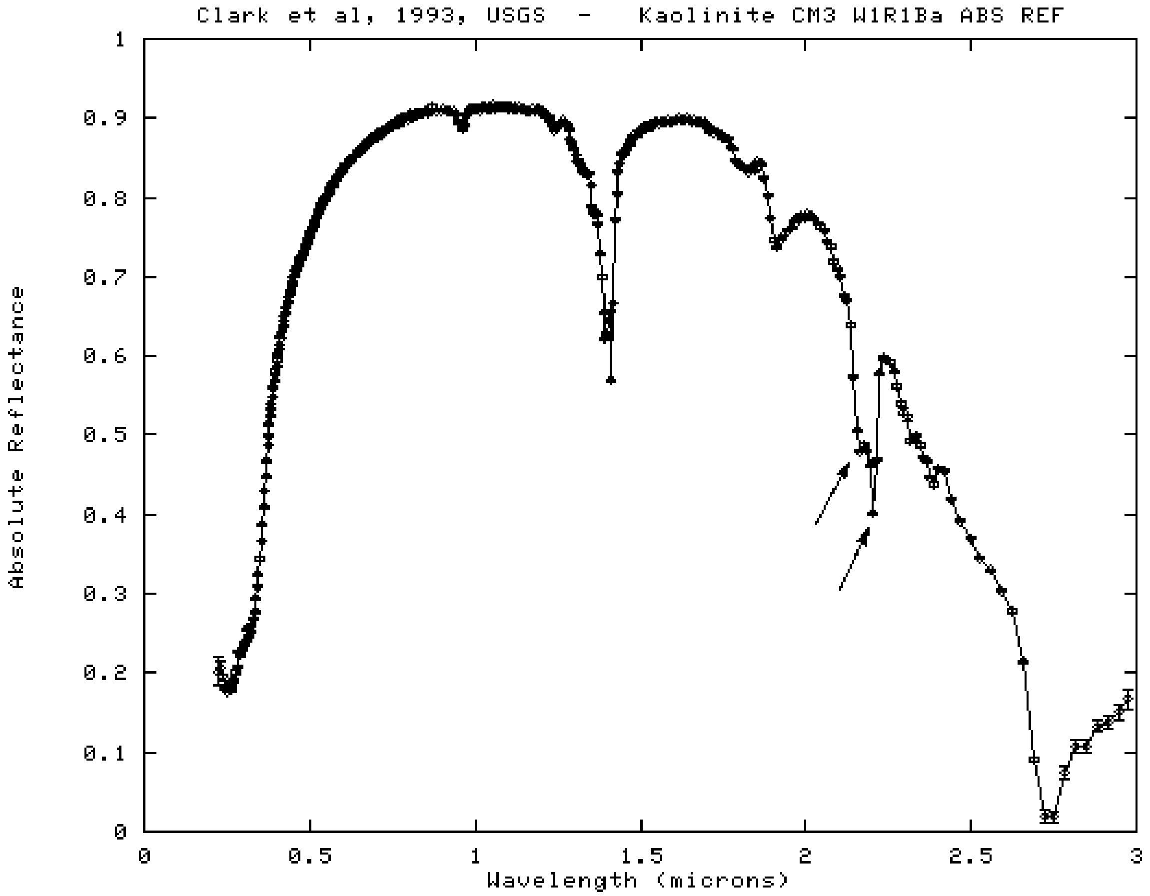

Figure 2.2-2. Laboratory spectrum of kaolinite showing the absorptions at 1.4µm and the doublet at 2.2µm (arrows).

The complete utilization of hyperspectral reflectance spectroscopy is still developing. Geologists are now able to map minerals in regions (*e.g.*, the Cuprite Mining district in Nevada) by employing imaging spectrometers such as AVIRIS (Figure 2.2-3).

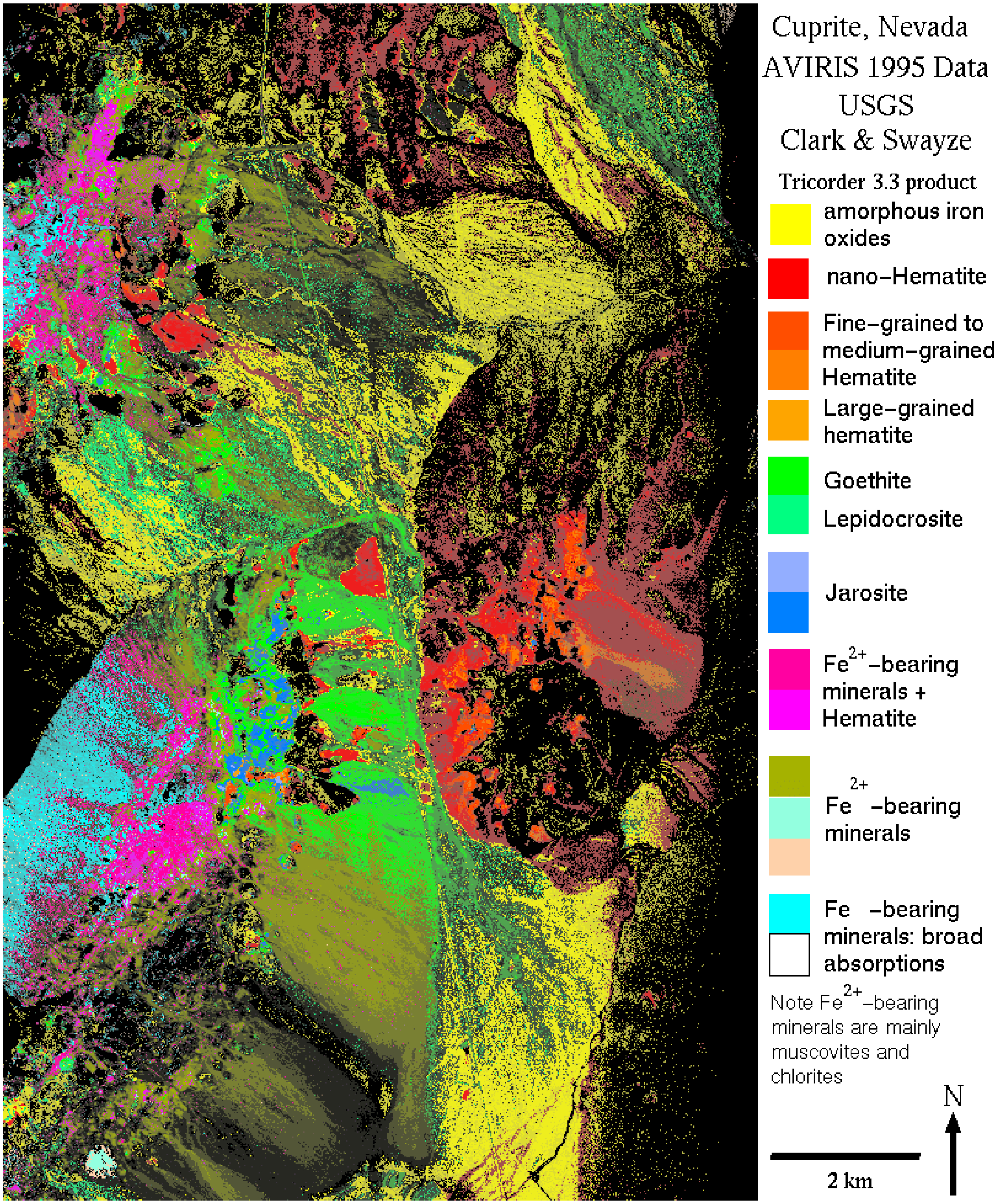

Figure 2.2-3. Mineral mapping of the Cuprite mining region, Nevada with the Tricorder algorithm (courtesy of Clark, USGS)

Algorithms such as "Tricorder" (Clark, 1991) compare the continuum-removed spectral features from imaging spectrometer data to continuum-removed spectra from a reference library of materials. Multiple absorption features are examined and the pixel is classified to the material in the library data set with the most similar spectral absorption features.

Mineral mapping is only one of many uses of imaging spectrometer data. Plant species and their condition also may be assessed using this technique (Figure 2.2-4). Potatoes sprayed with defoliant show decreased overall absorption and a shift of the red edge of the chlorophyll absorption to shorter wavelengths (Clark, 1995). Species differences can be discriminated by the Tricorder algorithm based on shapes of the absorption spectra. For accurate classification, it is important to have as complete a spectral reference library as possible.

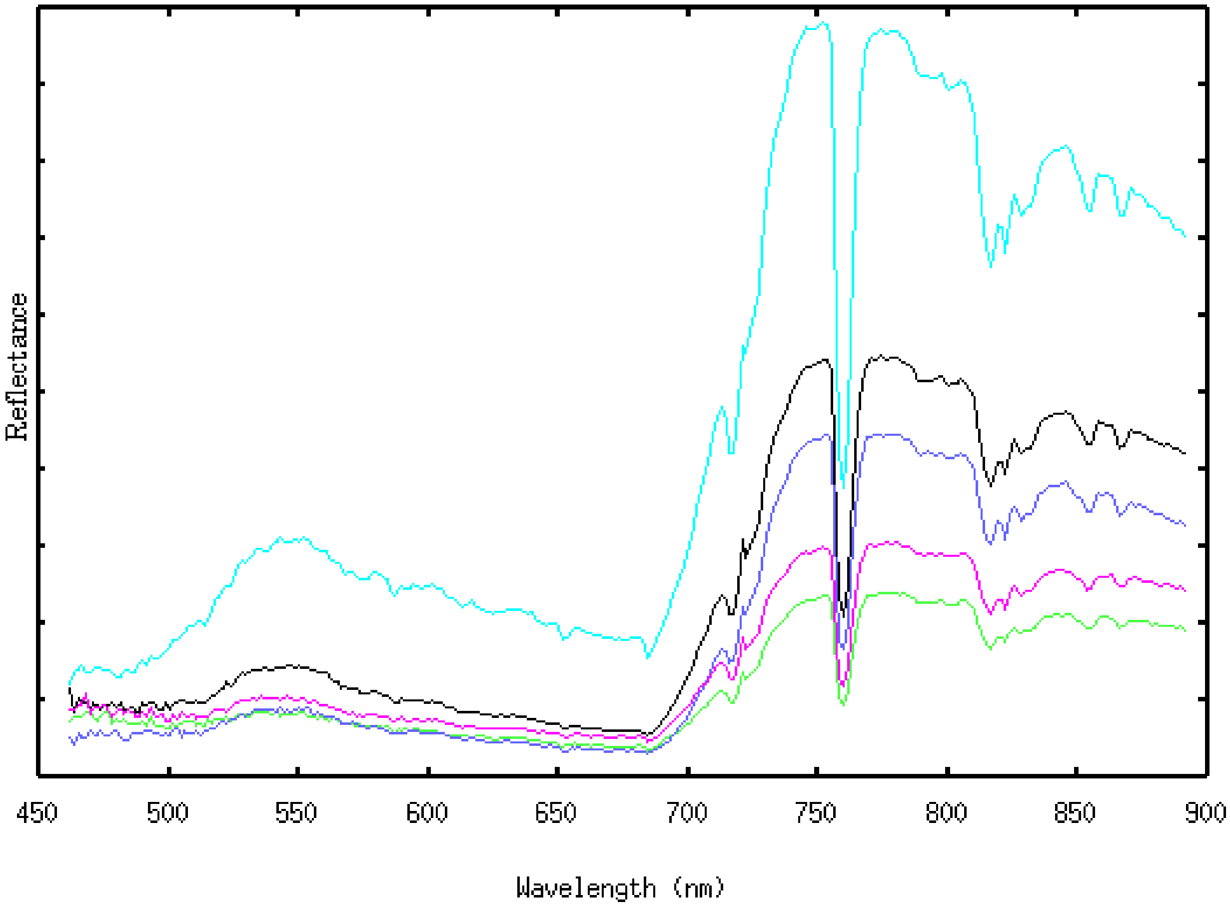

Figure 2.2-4. Various spectra of potato plants with increasing chlorophyll levels top to bottom (spectra courtesy of USGS).

It is clear that the reflectance spectrum derived from hyperspectral imaging can yield a great deal of information about surface content in an image scene. Since absorption feature signatures are indicators of chemical composition, many types of surface terrain may be classified by matching these features to specific mineral, plant, or man-made object library spectra. What has not been addressed is the impact of the atmosphere on the spectrum obtained from hyperspectral imagery. The earth atmosphere leaves the imprint of its chemical composition on the spectrum. The combination of atmospheric gases, water vapor, and suspended particulates (known as "aerosols") interact with light throughout the entire spectrum. An example of the influence of water vapor on atmospheric transmission is seen in Figure 2.2-5.

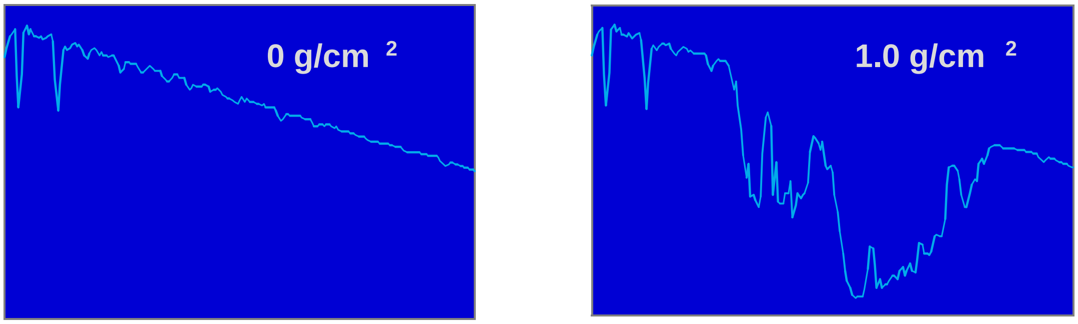

Figure 2.2-5. Column water vapor impact on atmospheric transmission spectrum from 0.86-1.017µm

Atmosphere constituents can have a significant effect on the spectrum of surface-leaving radiance of an object. This effect is, of course, propagated to the derived reflectance spectrum of the surface, making applications such as mineral mapping or plant-stress evaluation prone to error. Many spectral surface features that modern advanced algorithms seek to identify are altered by atmospheric interference.

Thus, it is imperative that the atmosphere be characterized and its effects removed from the hyperspectral radiance spectrum. The methods for characterizing and correcting the effects of the atmosphere on the sensor-acquired radiance spectrum are considered next in this discussion in the review of NLLSSF and APDA.

2.3 Techniques for In-Scene Extraction of Atmospheric Parameters

2.3.1 The Atmospheric Pre-Corrected Differential Absorption Technique (APDA)

The APDA method is a new technique that is a further refinement of the Continuum Interpolated Band Ratio method (CIBR) (Bruegge, 1990; Green, 1989) and the ATREM method (Gao et al., 1993). The governing radiometric equation for this algorithm is:

$$L(\lambda) = \rho(\lambda)\ \frac{1}{\pi}\ E_0(\lambda)\ \cos(\sigma)\ \tau_1(\lambda)\ \tau_2(\lambda) + L_{atm}(\lambda) \tag{2-1}$$

where $L(\lambda)$ is the radiance from one specific channel, $\rho(\lambda)$ is the reflectance of the ground (including adjacency effects), $E_0(\lambda)$ is the exoatmospheric irradiance, σ is the angle subtended from sun-to-earth normal, $\tau_1(\lambda)$ is the transmittance of the earth's atmosphere from the sun to the ground, $\tau_2(\lambda)$ is the transmittance of the earth's atmosphere from the ground to the sensor, and $L_{atm}(\lambda)$ is the total atmospheric upwelled radiance. The radiative transfer code MODTRAN 4.0 also takes into account curved earth effects. It is assumed that index of refraction changes in the atmospheric layers has a negligible effect at the sensor angular resolution.

The transmittance terms can be split further into parameters depending on water vapor and on aerosols and atmospheric gas absorption:

$$\tau_1(\lambda) = \tau_{1\_comp}\ \ \tau_{1wv} \tag{2-2}$$

$$\tau_{1\_comp} = \tau_{1\_aerosols}\ \ \tau_{1\_gases} \tag{2-3}$$

Substituting into Equation (2-1) yields:

$$\begin{aligned} L(\lambda) &= \left[\rho \, \frac{1}{\pi} \, E_o \cos\sigma \; \tau_{1\_comp} \; \tau_{2\_comp}\right] \tau_{1wv} \; \tau_{2wv} + L_{atm}(\lambda) \\ &= L_{grnd}(\lambda) \; \tau_{1wv} \; \tau_{2wv} + L_{atm}(\lambda) \end{aligned} \tag{2-4}$$

where $L_{grnd}(\lambda)$ and is the total ground reflected radiance at the sensor in the absence of atmospheric water vapor.

The radiances in the three channels can be written using this simplified equation where the parameter "m" is the index of the measurement channel in the peak water-vapor-absorption region centered on 0.94μm and r_1 and r_2 are the reference channels located in the atmospheric “windows” for water vapor on each side of the absorption peak (*i.e.*, $\tau_{i\mathrm{wv},r1} = 1.0$ & $\tau_{i\mathrm{wv},r2} = 1.0$). Assuming a small difference in the center wavelengths of the given channels, the radiance in the measurement channel can be approximated by a linear interpolation :

$$\begin{aligned} L_m &= [\omega_{r1} \; L_{grnd,r1} + \omega_{r2} \; L_{grnd,r2}] \; \tau_{1wv,m}(PW) \; \tau_{2wv,m}(PW) \\ &\quad + L_{atm,m}(PW) \end{aligned} \tag{2-5}$$

where:

$$\omega_{r_1} = \frac{\lambda_{r_2} - \lambda_m}{\lambda_{r_2} - \lambda_{r_1}} \tag{2-6}$$

$$\omega_{r_2} = \frac{\lambda_m - \lambda_{r_1}}{\lambda_{r_2} - \lambda_{r_1}} \tag{2-7}$$

By arranging Equation (2-5) to solve for the total transmission of water vapor and substituting L_{grnd} from Equation (2-4), the equation becomes very similar to the CIBR method but with the additional upwelled radiance correction terms.

$$\tau_{wv,m} = \frac{L_m - L_{atm,m}(PW)}{\omega_{r_1}(L_{r_1} - L_{atm,r_1}) + \omega_{r_2}(L_{r_2} - L_{atm,r_2})} \tag{2-8}$$

The path radiance corrections $L_{atm,i}$ contain functional parameters of terrain elevation, channel center wavelength, and quantity of water vapor. $L_{atm,i}$ can be estimated by calculating the total radiance at the sensor due to a zero albedo ground target with varying terrain height and water vapor content (assuming a fixed aerosol optical depth). The accuracy is increased by an iterative technique using water vapor contents retrieved from radiosonde profiles.

Equation (2-8) can be extended to multiple channels by calculating a regression line through an arbitrary number of channels and evaluating the derived regression curve at the mean center wavelength of the measurement channel(s). The numerator is the average of the differences of the sensor radiance and the path radiance in the measurement channels. This is the APDA equation for which the three-channel case is given in Equation (2-9):

$$R_{APDA} = \frac{\overline{[L_m - L_{atm,m}]_i}}{LIR([\lambda_r]_j, [L_r - L_{atm,r}]_j)|_{\overline{[\lambda_m]_i}}} \qquad (2\text{-}9)$$

where $LIR([x], [y])|_a$ refers to the regression line y=ax+b for the points

$y = Lr - L_{atm,r}$ evaluated at $x = \lambda_r$ in Equation (2-9). Essentially, this is a regression line across the atmospheric “windows” surrounding the water-vapor absorption feature (L_1 and L_2) in the spectrum (Figure 2.3-1). The denominator becomes the interpolated point L_4 with the estimated upwelling radiance subtracted. The numerator of Equation (2-9) is located at the wavelength of the trough of the absorption feature (L_3) in Figure 2.3-1. The subscripts *i* and *j* in Equation (2-9) refer to the measurement and reference channels respectively.

Again, it must be made clear that the atmospheric windows at positions L_1 and L_2 in Figure 2.3-1 can be affected by water vapor in the atmosphere. For the purpose of this model, this effect is considered to be negligent since the water vapor lines inherent in the band model are not close to being saturated.

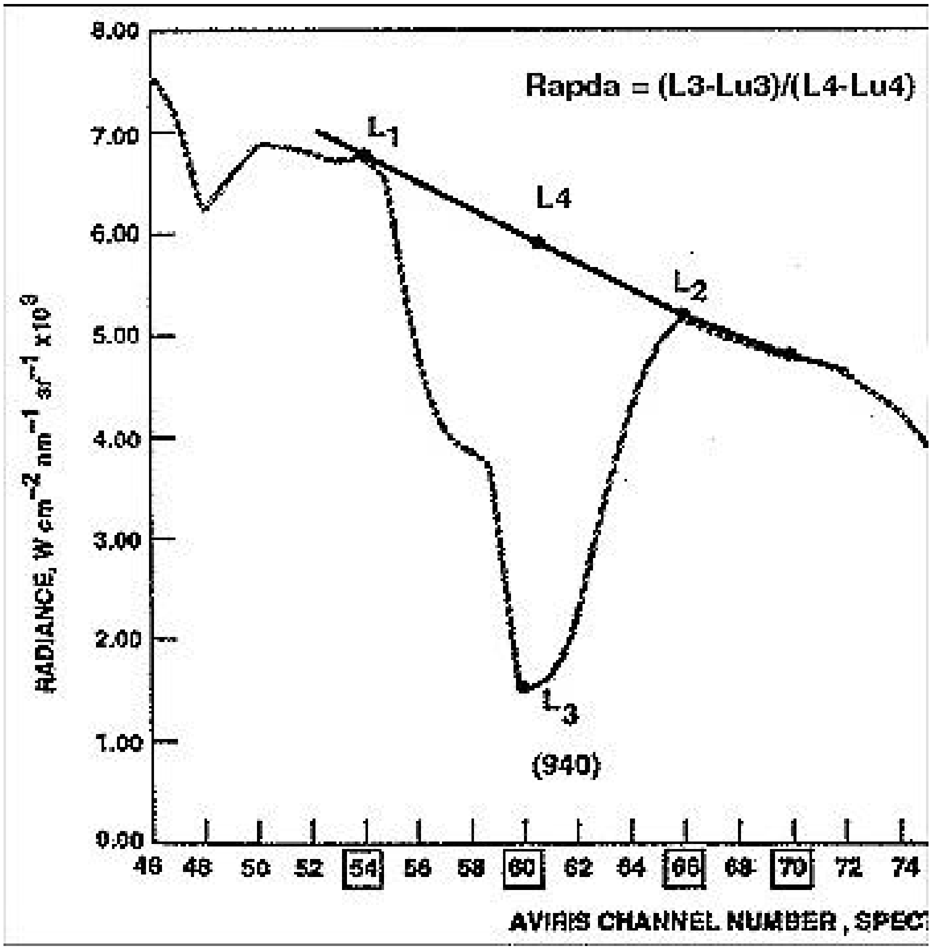

Figure 2.3-1. Linear regression across the 940nm water vapor band (courtesy of Daniel Schlaepfer and Chris Borel).

An exponential approach similar to Beer's Law is used to relate the R ratio to the corresponding precipitable water vapor amount (PW):

$$\tau_{wv}(PW) \approx R_{APDA} = e^{-(\gamma+\alpha(PW)^{\beta})} \tag{2-10}$$

where α, B, and γ are the parameters of columnar water vapor content. This equation is approximately true when the water vapor lines are not saturated. It is assumed that there is not fog or near fog conditions which is reasonable since a very low percentage of remotely sensed imagery is acquired or can be very useful under these circumstances. Solving Equation (2-10) for the water vapor content:

$$PW(R_{APDA}) = \left(\frac{-\ln(R_{APDA}) - \gamma}{\alpha}\right)^{\frac{1}{\beta}} \tag{2-11}$$

The following APDA algorithm is used to compute the columnar water vapor content of a given hyperspectral image (Schläepfer, 1996):

1. A radiative transfer program such as MODTRAN 4 is used to compute a LUT containing both the total radiance at the sensor for an average reflectance background (such as $\rho=0.4$) and the atmospheric upwelling radiance as a function of water content, terrain elevation, wavelength, and atmospheric conditions. (The atmospheric conditions are defined in the MODTRAN input file "tape5".) The MODTRAN-derived radiances are then convolved with the normalized sensor response function(s) to give sample radiance values. Water content can be varied by scaling water vapor density in a standard radiosonde file. Terrain height can be determined by using known topography information or by using an empirical method developed by Schläepfer and Borel.

2. Determine the R_{APDA} values for the water vapor amounts specific to each MODTRAN run by applying Equation (2-9).

3. Regress the random variables PW against R_{APDA} using the function in Equation (2-10) and store the regression parameters α, β, and γ.

4. Assume some starting PW1 for the hyperspectral image pixels based on the radiosonde profile and subtract the upwelling radiance term from the image.

5. Calculate the APDA ratio for the pixel and transform back into a PW2 via Equation (2-11) with the stored regression parameters.

6. With this improved estimate PW2, calculate the new L_{atm} for substitution in Equation (2-9)

7. Calculate the R ratio for the image (pixel) again and inverse transform the ratio values into a final PW3.

Previous experiments have shown that two iterations are sufficient to obtain good results. Increasing the number of iterations can actually result in divergence since the errors may be amplified.

Comparisons have been made between the ATREM-like CIBR method and the APDA technique for retrieving columnar water vapor over dark, bright, and spectrally variable backgrounds. The atmospheres for the comparisons were generated by MODTRAN. Many reflectance spectra of minerals, man-made objects, and simulated vegetation were used with a resulting water vapor error within ±5% for most of the spectra (Schläepfer, 1996) as can be seen in Figure 2.3-2. The authors consider this accuracy sufficient since current sensor calibration and modeling errors are of the same order. No error analysis has been performed on APDA's dependence on atmospheric conditions (aerosol loadings, stratification, etc.), calibration errors, and radiative transfer code uncertainties.

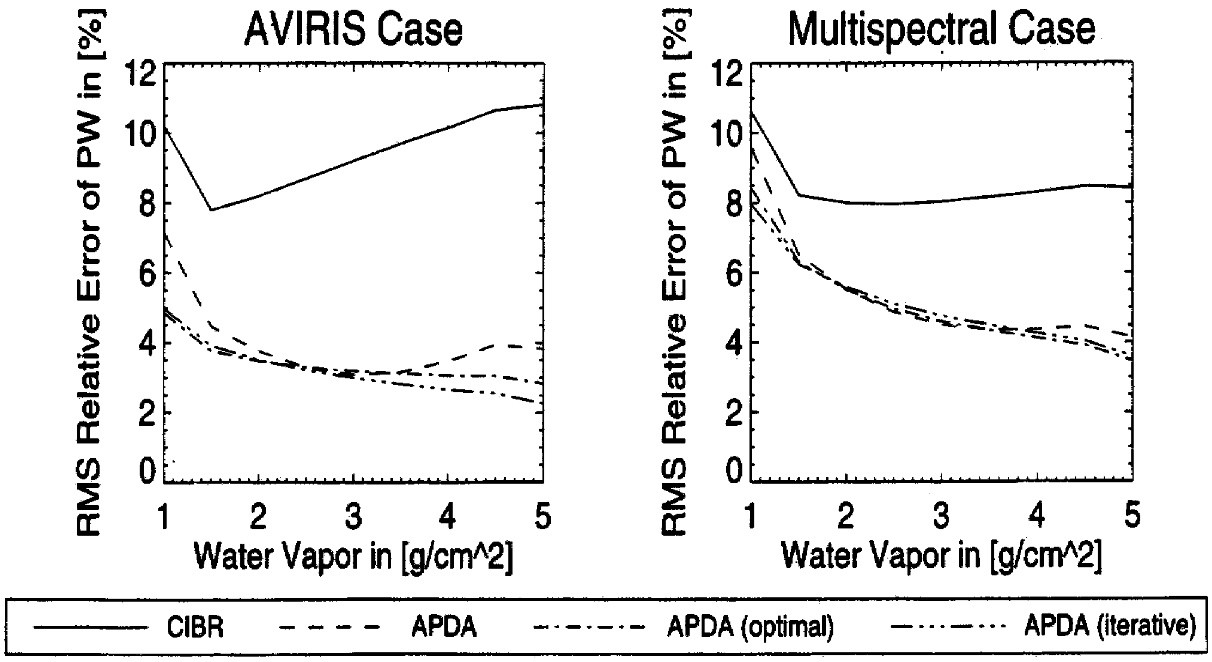

Figure 2.3-2. RMS relative error in % water vapor for 379 reflectance spectra using four different water vapor retrieval techniques.

The next water vapor extraction technique reviewed in this section departs from the band-ratio methodology and attempts to fit the spectrum in the water vapor absorption region to a curve with variable parameters. The NonLinear Least Squares Spectral Fit (NLLSSF) technique allows for more degrees of freedom to account for radiometric parameters and is consequently more computationally intensive than APDA.

2.3.2 The NonLinear Least-Squares Spectral Fit Model (NLLSSF)

The NLLSSF technique developed by Green (1989) resembles the ATREM method (Gao, et al., 1993) in that it is a complete atmospheric correction that inverts the governing radiative transfer equation to solve for surface reflectance. Since the water vapor in this method is calculated just before the inversion, all constituent modules of the algorithm up to and including the column water vapor determination are covered in this section.

Upon inspection of the governing radiative transfer equation for a remotely sensed scene, it is evident that a number of terms must be known to solve for apparent surface reflectance. Elements such as atmospheric molecular absorptions and elemental scattering properties of the surface, atmospheric aerosols, and the solar source must be characterized and included in the generation of a model of a calibrated radiance spectra for a given scene (Green, 1996). If many of the radiometric parameters can be known or closely estimated, a robust radiative transfer model can be run with fewer flexible parameters. One by one, the flex parameters can be determined to obtain a close estimation of what was detected at the sensor. The nonlinear least-squares spectral fit is one such process that obtains an estimate of apparent ground reflectance by using a governing radiative transfer equation and a radiative transfer model such as MODTRAN 4. Because of the complex interaction of variables in a remotely sensed scene, the algorithm begins with the user inserting parameters in the model that can be known and then estimates the terms that are more difficult to obtain.

The algorithm to generate the model should include all known parameters of the remotely sensed scene, such as the geometry of observation, time of day, latitude and longitude, radiosonde data (if available), terrain height (if available), sensor altitude, and exoatmospheric irradiance. The assignment of these parameters sets a constraint on the radiative transfer algorithm with the goal of minimizing the degrees of freedom. From here, intelligent assumptions must be made about the atmospheric composition, especially if radiosonde data are not available for a baseline. Assumed parameters can include aerosol type, visibility, air pressure, temperature, etc. Column water vapor is the flexible parameter in the atmospheric model.

With a baseline atmosphere, the only parameter(s) remaining in the radiative transfer program are the reflectance characteristics of the ground object(s). If the spectral region of interest is sufficiently narrow (as is true for the water vapor band), it may be possible to assume that the object reflectance ρ is linear with wavelength λ. Thus, a model of reflectance can be built:

$$\rho = \alpha + \beta\lambda \tag{2-12}$$

In some cases, there may be instances where nonlinear behavior occurs which is caused by some quantified physical phenomenon, such as the absorption of liquid water in vegetation in the 0.86-1.0177μm water vapor band (Figure 2.3-3) or the chlorophyll feature at 0.7μm. This nonlinear modeling can be easily added by introducing a scaled reflectance parameter to Equation (2-13) where γ is the flexible scalar and $\rho_{vegetation}(\lambda)$ is the reflectance curve of liquid water in vegetation (or the reflectance curve of the chlorophyll band):

$$\rho = \alpha + \beta\lambda + \gamma\rho_{vegetation}(\lambda) \tag{2-13}$$

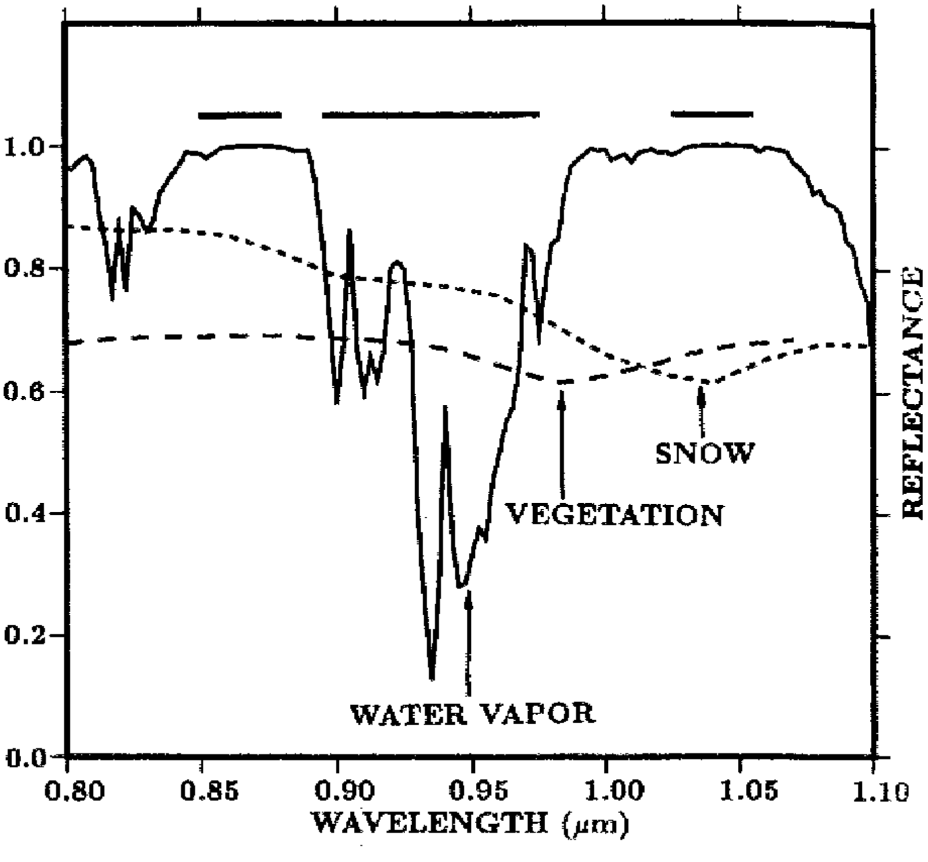

Figure 2.3-3. Examples of a calculated water vapor transmittance spectrum and measured reflectance spectra of vegetation and snow (Gao, 1993).

At this point, a model of the scene has been built with four flexible parameters: reflectance bias (α), reflectance gain (β), proportion of nonlinearity due to surface leaf water (γ), and atmospheric water vapor.

One method for solving for these parameters is a multivariate solution to a nonlinear least-squares spectral fit (NLLSSF) between the spectral radiance measured by the hyperspectral sensor and the spectral radiance calculated by a radiative transfer code, in this case MODTRAN 4. Most multivariate solutions require estimates of the functions or their slopes to solve for the parameters. Given the complexity of the radiative transfer models, use of these types of curve-fitting routines is out of the question. The “best” curve-fitting routine in terms of efficiency and speed for this model is a downhill simplex algorithm (Press, 1992), sometimes called the "amoeba" curve-fitting technique, that is designed to find global minima or maxima of a function. The routine name "amoeba" is descriptive of the way the simplex contorts in *n*-dimensional space as the minimum of the function (with *n* number of varying parameters) is being sought (Figure 2.3-4).

For this model, the minimum difference between the MODTRAN 4-derived radiance and the image radiance in their respective channels can be sought. A general flow of the amoeba curve-fitting technique is shown in Figure 2.3-5.

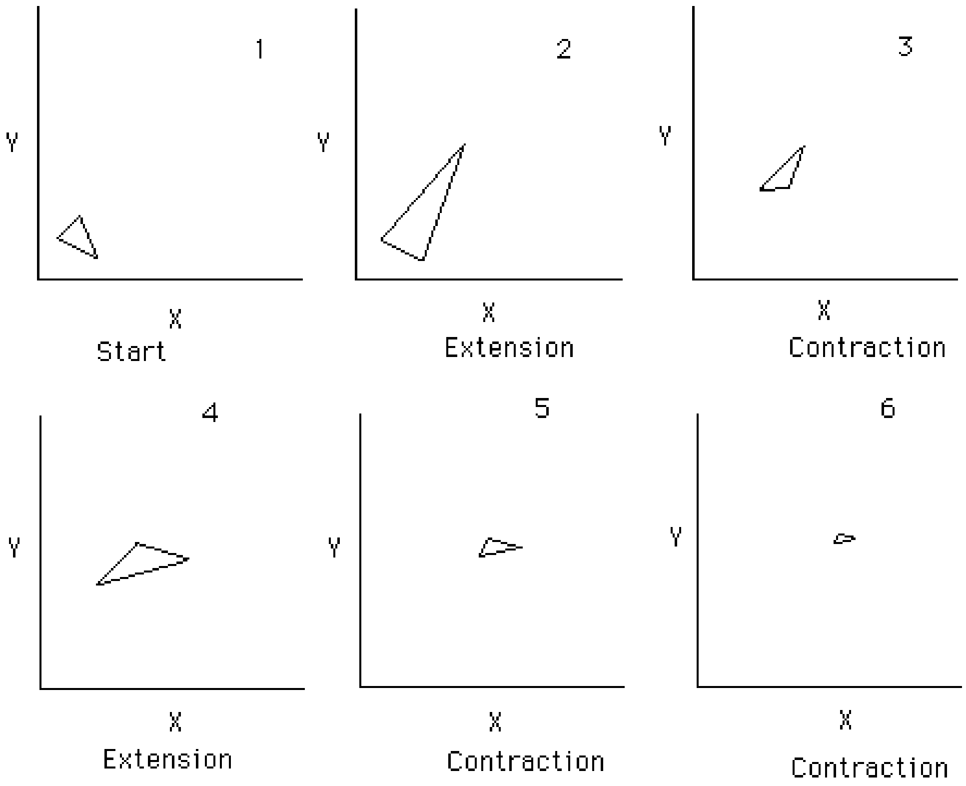

Figure 2.3-4. Simplex changing shape as minimum is sought in two-dimensional space (lower right frame has simplex contracting around calculated global minimum).

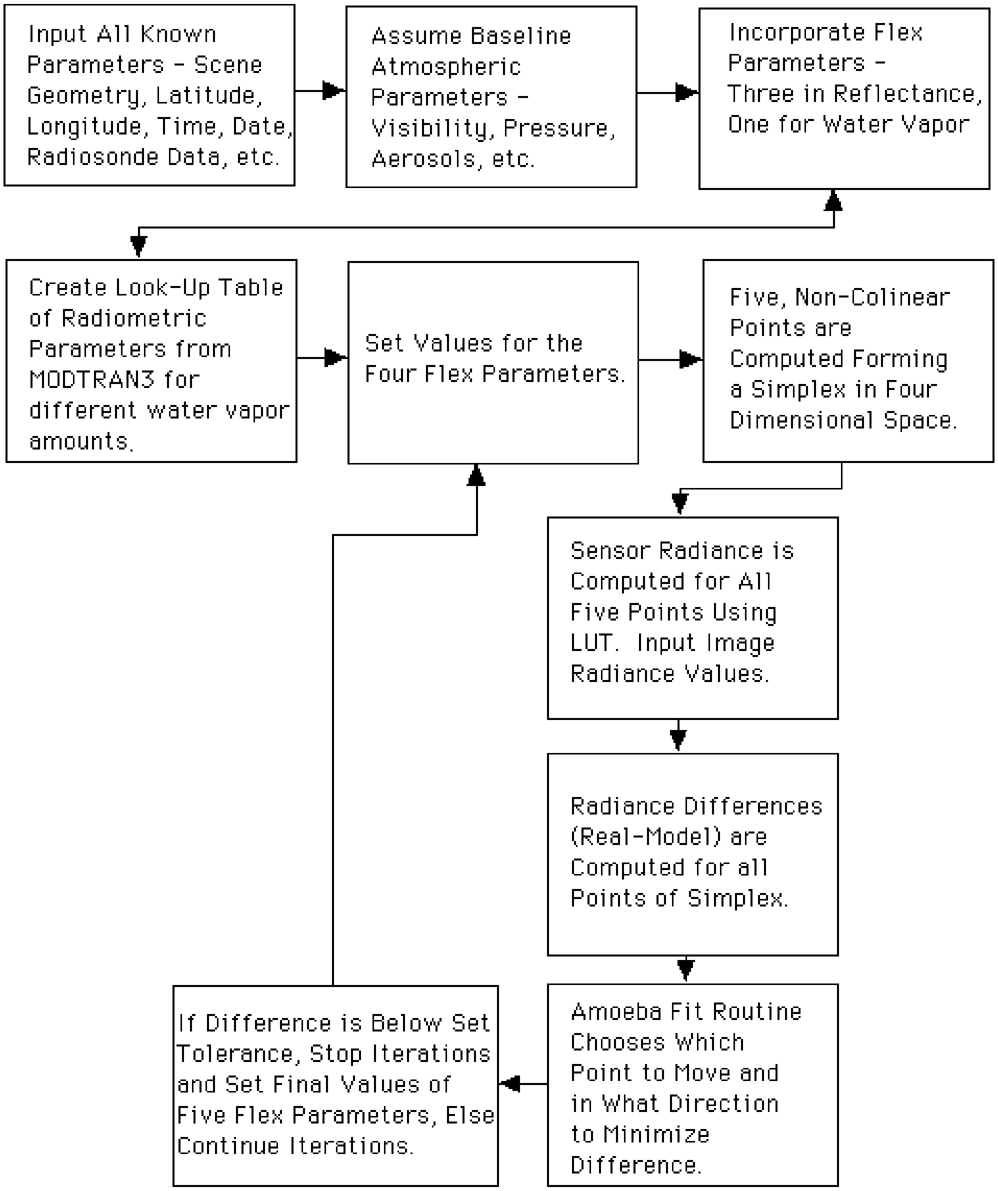

Figure 2.3-5. Flow chart of amoeba curve-fitting technique for columnar water vapor.

For assurance that an actual global minimum has been found by the amoeba rather than a local minimum, it has been suggested by the algorithm creators that the algorithm be run a second time. The initial parameters are the first pass final solutions. If the minimum is really global, the amoeba will converge back down to the first pass solutions after a few iterations. This test is addressed for the NLLSSF algorithm in the second pass through the atmospheric correction algorithm (refer to Section 3.1).

Noise due to the sensor system and random photon arrivals is inherent in any real image. The signal-to-noise ratio (SNR) can be increased by averaging sample values; the SNR increases with the square root of the number of samples averaged if the noise is uncorrelated. For example, the spectrum can be averaged over a 5x5-pixel area to reduce the noise in image radiance by a factor of five. This averaging improves the estimate of the derived column water vapor amount in the area of interest.

In the following modules, reference is made to a MODTRAN-generated LookUp Table (LUT). To aid in the understanding of how NLLSSF works, brief procedures are outlined. Because of the complexity of the LUT generation, a separate sub-section (Section 2.6) was created that expounds on this topic in much greater detail. Suffice for the reader at this point that the LUT is a multidimensional data structure that contains all the radiometric terms for the radiative transfer equation as functions of surface elevation, visibility, water vapor, and wavelength. A caution should also be given to the user of this technique. Since the dimensionality of this multivariate data is fairly high, the NLLSSF technique needs initial values for the surface elevation, visibility, and columnar water vapor that are close to the truth in order for the algorithm to converge to a realistic set of radiometric values.

Module 1: Surface Pressure Height

The total radiance reaching a hyperspectral sensor is a function of the absorption by well-mixed gases in the atmosphere in both source-to-target and target-to-sensor paths. One of the strongest atmospheric gas absorption features is due to oxygen and spans the spectral range from about 745nm to 785nm, with its peaks located at approximately 760nm (Figure 2.3-6). The oxygen band strength is calibrated to surface pressure elevation using the oxygen band model in the MODTRAN 4 radiative transfer code. In practice, an LUT generated from

MODTRAN 4 contains the sun-ground-sensor direct radiance (L_{grnd}), the upwelled path radiance (L_u), the scattered downwelled radiance (L_D), and the spherical albedo (S) of the atmosphere above the surface, all as functions of a fixed sensor elevation and terrain height *z*. The convolution of spectral radiance from MODTRAN 4 with the sensor response function for the final LUT values is calculated. It should be noted that all of these terms are functions of wavelength.

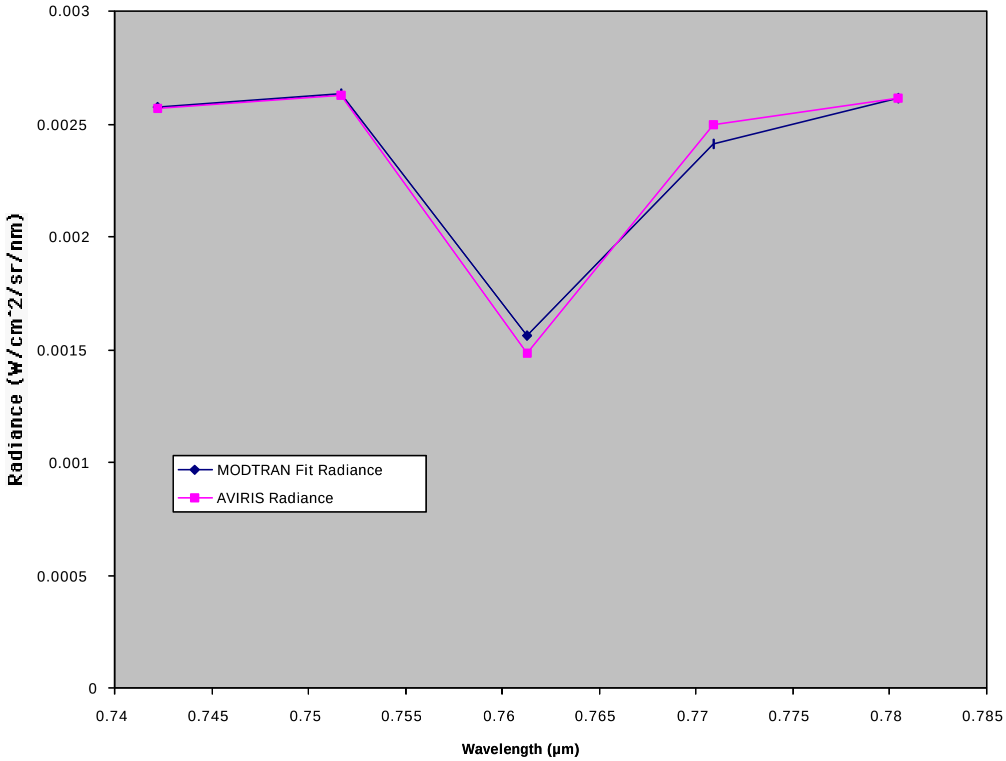

Figure 2.3-6. A MODTRAN 4 NLLSSF spectrum and AVIRIS Boreas measured spectrum for the oxygen band at 760nm .

The reflectance of the surface is modeled as a linear function of wavelength (Green, 1991b) as given in Equation (2-12) with a bias term (α) and a gain term. The aforementioned parameters and *z* are allowed to vary to iteratively fit the governing radiative transfer equation derived from Green, (1996) to the calibrated radiance at the sensor via NLLSSF:

$$L_{calc\_sensor}(\lambda) = L_u(\lambda) + \frac{\rho(\lambda)\left[L_{grnd}(\lambda) + L_D(\lambda)\right]}{1-\rho(\lambda)\;S(\lambda)} \qquad (2\text{-}14)$$

where (1-$\rho(\lambda)S(\lambda)$) is a gain term for the trapping effect and the radiance vector from sun-to-ground-to-sensor is:

$$L_{grnd}(\lambda) = \frac{E_0(\lambda)\ \tau_1(\lambda)\ \tau 2(\lambda)\ \cos\sigma}{\pi} \tag{2-15}$$

where $E_0(\lambda)$ is the solar irradiance, $\tau_1(\lambda)$ is the transmission from sun to the target, $\tau_2(\lambda)$ is the total transmission from the ground to the sensor, and σ is the solar zenith angle. (Equation 2-15 assumes that the ground target has Lambertian reflectance characteristics.)

The question may arise of the effect of the distance *z* from sensor to target on the surface pressure depth pz. The depth of the 760nm oxygen band is proportional to the amount of oxygen in the atmosphere between the sensor and target. Greater pressure means more column oxygen and indicates a longer range from sensor to target. This being said, it should be noted that the same baseline atmosphere is used at the beginning of this module, which is included in the MODTRAN 4 carddecks for all *z* values. Essentially, the surface pressure parameter in the carddeck is being scaled by *z* which produces a depth of the oxygen band absorption proportional to p**z*. For example, in Figure 2.3-7 the sensor is located at some fixed altitude with a true sensor-target range and surface pressure.

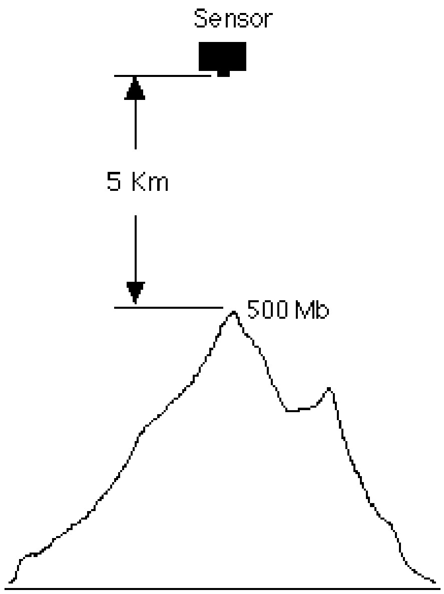

Figure 2.3-7. Surface pressure and elevation over target.

If the surface pressure given in the baseline carddeck is less than the actual atmospheric pressure, the parameter p*z* will ultimately produce an oxygen absorption band depth that is less than the oxygen absorption band depth from the image. Thus, increasing z will minimize the error between real and predicted oxygen absorption as well as minimize the error between real and predicted pz. It is not important that *z* be correct, but the parameter p*z* must be as close as possible to the real value. Using the data from Figure 2.3-7:

$$\text{SPE} = 5\ \text{Km} * 500\text{Mb} = 2500\ \text{Km Mb} \qquad (2\text{-}16)$$

where SPE is the surface pressure elevation. From the baseline atmosphere, surface pressure at this elevation was 400Mb, thus the best predicted fit for the oxygen absorption band would assume:

$$z = \frac{2500\ \text{KmMb}}{400\ \text{Mb}} = 6.26\ \text{Km} \qquad (2\text{-}17)$$

The surface-pressure elevation would then be fixed and used as an atmosphere parameter in the next module that estimates the aerosol-dependent visibility.

Module 2: Aerosol (Atmospheric Visibility)

The radiance scattered by atmospheric aerosols can be a significant contributor to the total radiance reaching the sensor. The Mie scattering coefficient resulting from atmospheric aerosols is proportional to $\frac{1}{\lambda}$. In this case, Mie scattering is significant in the range from 400 to 700nm owing to the extremely small size of the particles. This type of scattering is even more pronounced at shorter wavelengths of the spectrum.

The NLLSSF algorithm is employed to fit the sampled calibrated radiance spectrum in the range of strongest aerosol impact (see Figure 2.3-8). In this case, the flexible parameters in the amoeba-fitting routine are: atmospheric visibility (a scalar for the aerosol number density), reflectance bias, reflectance gain, and proportion of nonlinearity due the chlorophyll in vegetation. Recall that the surface elevation has already been fixed from the previous routine.

The aspects of aerosol type (e.g., urban, rural, maritime, etc.) and scattering (e.g., single or multi-scattering) are constrained by user-defined/estimated input to the MODTRAN 4 carddeck before running the NLLSSF algorithm. For many of the acquisitions of high-visibility data made by AVIRIS, the effect of aerosol scattering is strongest below $\lambda=1\mu m$. This allows the user to constrain the range of the spectral curve from $0.4\mu m$ to $0.7\mu m$ or approximately 30 channels of $0.01\mu m$ bandwidth.

To calculate aerosol optical depth, the amoeba algorithm is employed which uses a downhill simplex method to minimize a multidimensional function. In this case, the function to be minimized is the absolute difference of the sensor-measured radiance and the radiance at the sensor given by the governing radiative transfer equation (Equation 2-14) with parameter values taken from MODTRAN 4.0 runs. Although there are a number of accepted multidimensional minimization methods available for use in these calculations, the downhill simplex method is the most practical selection. It requires only evaluations of functions (not derivatives) and is accepted as the *best* method to use if the figure of merit is to “get something working quickly” for a problem whose computational burden is small (Press, 1992). Another attractive aspect of the method is that the fit parameters can easily be constrained without added computational burden. The routine also can avoid local minima by restarting the algorithm at the place where it last ended to have confidence about generating parameters from the global minimum.

To effectively incorporate this algorithm as the NLLSSF for the spectral curve, an LUT is constructed from multiple runs of MODTRAN 4 where only the visibility is varied in predetermined increments. Thus, when the amoeba routine calls the function evaluator subroutine (which uses Equation 2-14 and subtracts it from the image pixel radiance value), any visibility parameter between incremented values in the LUT can quickly be interpolated from the estimated visibility being tested by the amoeba fit.

As stated previously, the primary variable is the atmospheric visibility, with three other secondary parameters of α, β, and γ from the reflectance term (Equation 2-13). An example of the spectral curve generated from this routine is shown in Figure 2.3-8. To improve the SNR of the data and the subsequent curve-fit, the data were averaged over a region of size 11-by-11 pixels.

The resulting 47.73km visibility is consistent with the typical values for aerosols in the ARM site rural location.

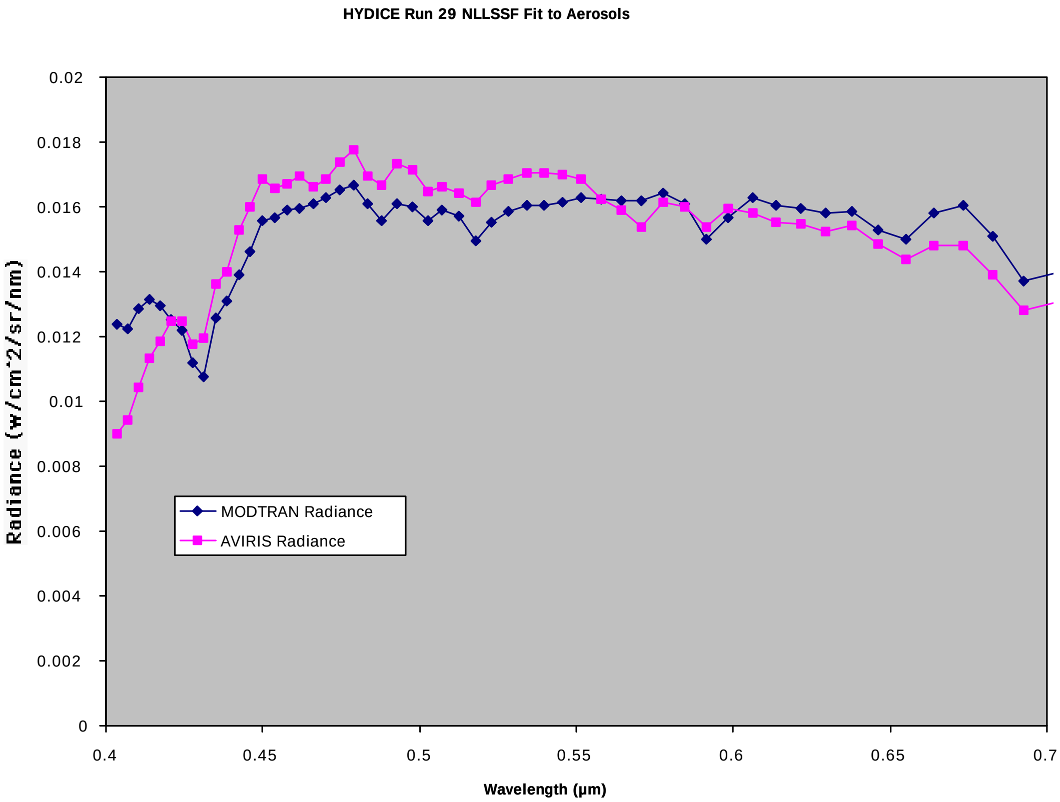

Figure 2.3-8. NLLSSF for aerosols over the 16% ARM site gray panel .

Module 3: Total Column Water Vapor

Water vapor is by far the most significant absorbing constituent in the atmosphere over the visible/NIR/SWIR spectral range. In addition, water vapor content in the atmosphere varies widely in amount and distribution over space and time, even across topographically featureless regions (Green, 1991b). Given the strength of this absorption feature, it is clear that total columnar water vapor must be determined to accurately retrieve reflectance data for ground targets.

The final step in this algorithm computes the total columnar water vapor for an image pixel by fitting the MODTRAN 4 derived spectral radiance at the sensor to the spectral radiance curve of the 940nm water vapor absorption band. The parameters to be varied include the water vapor amount and three terms in the reflectance equation (Equation 2-13). By this time, the surface elevation (pressure-depth) and the atmospheric visibility have both been fixed from modules one and two. Thus, the radiometry in the LUT is narrowed down so that the values can vary as a function of different columnar water vapor amounts. The water vapor temperature is assumed to be in equilibrium with the atmospheric layer(s).

To accelerate the computation, a LookUp Table (LUT) is generated from an estimated (or actual) radiosonde profile with water-vapor density (as a function of altitude) in place of relative humidity. Additional radiosonde files are created simply by scaling the water vapor densities to create profiles with varying total columnar water vapor (PW). Carddecks for the MODTRAN 4 radiative transfer algorithm are created with each of the new radiosonde profiles and MODTRAN 4 then generates L_{grnd}, L_u, L_D, τ_2, and S for each PW. The NLLSSF algorithm uses these data as a LUT to fit the spectral radiance modeled by the radiation transfer code and the sensor-measured spectral radiance between 850nm and 1050nm (Figure 2.3-9). Both visibility (aerosol loading) and surface pressure elevation are constrained by the previous steps in the algorithm.

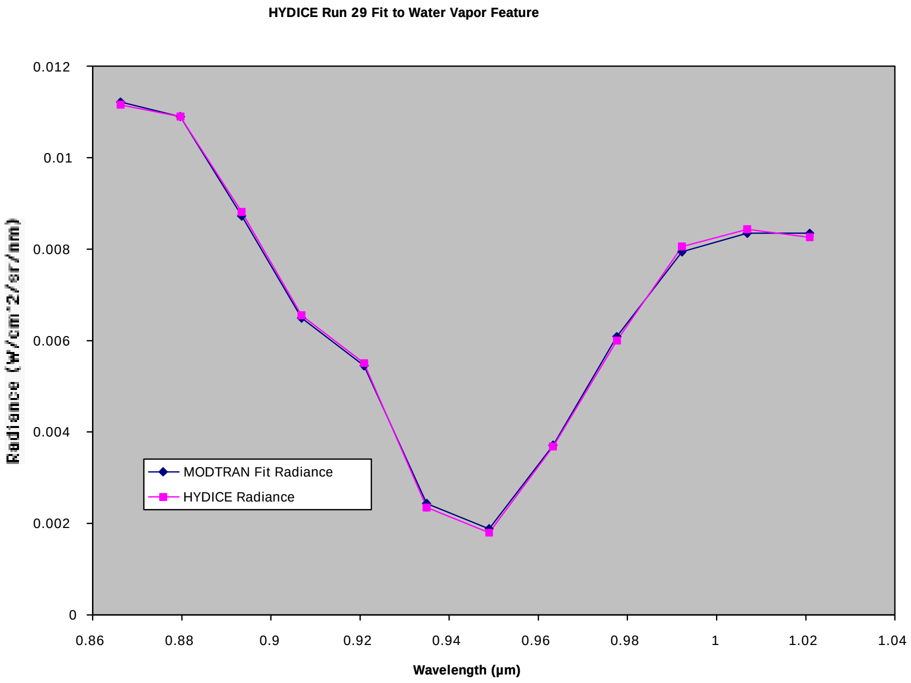

Figure 2.3-9. Water vapor spectral fit for the HYDICE Run29 16% gray panel (6.803 g/cm^2).

Using these parameters and the total column water vapor from this subroutine, the governing radiative transfer equation (2-14) can be inverted to solve for apparent surface reflectance. Figure 2.3-10 shows the derived reflectance (Tot_Inv) compared to surface ground truth (Truth) for the ARM site gray panels. As can be seen, both measured spectral reflectance curves agree well with NLLSSF-derived spectral reflectance.

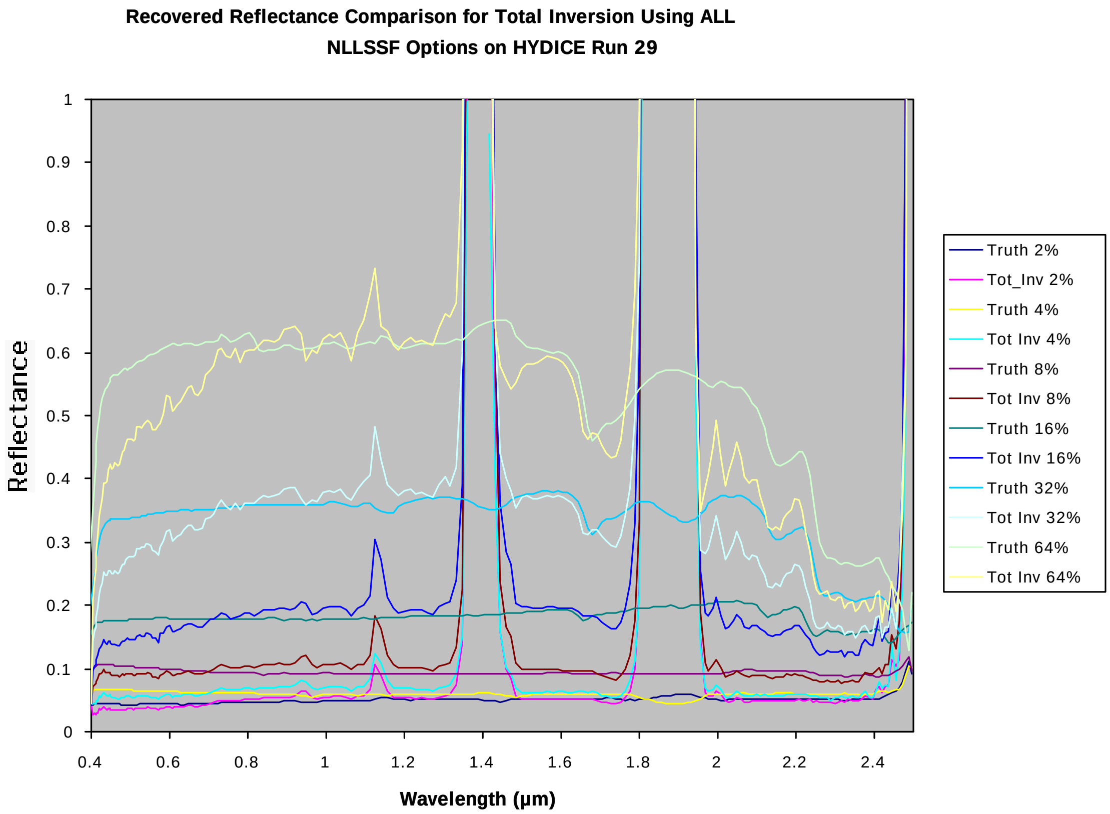

Figure 2.3-10. Calculated surface reflectance compared to measured field spectral reflectance for the ARM site gray panels (from nominal 2% reflectance – 64% reflectance).

This concludes the discussion of atmospheric parameter extraction techniques for hyperspectral imagery. APDA relies on a depth ratio of an absorption band to determine water vapor while NLLSSF uses a curve-fitting routine to estimate parameters in the radiative transfer equation.

2.4 Atmospheric Aerosols: Description and Existing Algorithms

2.4.1 Aerosol Properties

Aerosols are defined as solid or liquid airborne particles that are composed of various materials and found in stratified layers of the earth's atmosphere. Their sizes range from about 0.1µm to 10µm, though the sizes of condensation nuclei are typically about 0.01µm (Diner, 1994). Natural sources such as dust storms, desert and soil erosion, biogenic emissions, forest and grassland fires, and sea spray account for as much as 90% of the tropospheric aerosol loading, with man-made sources making up the balance.

The chemical composition of aerosols is varied; the main contributing substance is sulfur in the form of sulfates produced by the oxidation of gaseous sulfur dioxide generated as a by-product of industrial activity (Horvath, 1996). About 80% of the mass is contained in particles of size less than 1µm in diameter. The next most important substance is silicon, which has a bimodal size distribution peaking at 0.7 and 3µm, and is mostly derived from soil. However, it has been shown that submicrometer-sized silicon particle sources are typically due to coal-fired power plants and the combustion of household waste. Calcium is another soil-derived aerosol and typically has particle diameters greater than 3µm. Iron is commonly found in urban atmospheres and originates either in industrial or power plant emissions. Iron particles have a not-too-well defined distribution peak at d=0.7µm. Coarse particle sizes have been found ($d \cong$ 3µm) and are attributed to road dust in towns. Lead had been considered a tracer for automotive emissions in the past until the barring of lead additives in gasoline. Most of these aerosol particles with d < 1µm are emitted by incinerators and coal-fired power plants. Black carbon is the only light-absorbing aerosol in the atmosphere and is derived mainly from diesel emissions. The size distribution peaks at d=0.25µm and d=0.5µm; the former peak coincides with the size of diesel particles in exhaust gases. Due to traffic factors, no other aerosol element exhibits such a large difference in atmospheric density between inner city and suburban regions.

The effect of atmospheric aerosols on the earth biosphere is presently under intense study by the scientific community. One of the most ambitious studies is incorporated in the MISR (Multi-Angle Imaging Spectroradiometer) project at the Jet Propulsion Laboratory in Pasadena, California. The scientific objectives of the MISR aerosol retrievals are:

1) To study the spatial and temporal variability of aerosols in the earth's atmosphere and determine their effect on climate,

2) To improve the knowledge of the sources, sinks, and global budget of aerosols,

3) To characterize aerosols in the atmosphere and incorporate them in radiative transfer and scattering algorithms to make better quantitative estimates of absolute surface reflectances.

The third goal of the MISR project also is the goal of this research effort. For many years, the remote sensing community has strived to make quantitative assessments of surface-leaving radiance and reflectance from high altitude or spaceborne platforms. Attenuation of the sun by absorption and scattering due to atmospheric aerosols can alter the solar radiance by:

1) Reflection off the atmosphere,

2) Multiple reflections between the surface and atmosphere, and

3) Scattering into the target-sensor path from nearby surface.

The amount and the direction of light scatter in the atmosphere depend strongly on the ratio of the aerosol particle size to the wavelength of the incident light. When the particles are much larger than λ, the scattering is best explained by Mie theory. The atmospheric density of aerosol particles is usually characterized by one or two mean particle size components in a log-normal distribution (Shettle & Fenn, 1979). This distribution is given by:

$$\frac{dN(r)}{dr} = \sum_{i=1}^{2}\left(\frac{N_i}{\ln(10)\bullet r \bullet \sigma_i \sqrt{2\pi}}\right)\exp -\left[\frac{(\log(r)-\log(r_i))^2}{2\sigma_i^2}\right] \qquad (2\text{-}18)$$

where **N(r)** is the cumulative number density of particles of radius **r**, σ is the standard deviation of the distribution, and $\mathbf{r_i}$ and $\mathbf{N_i}$ are the mode radius and the number density of the i^{th} mode.

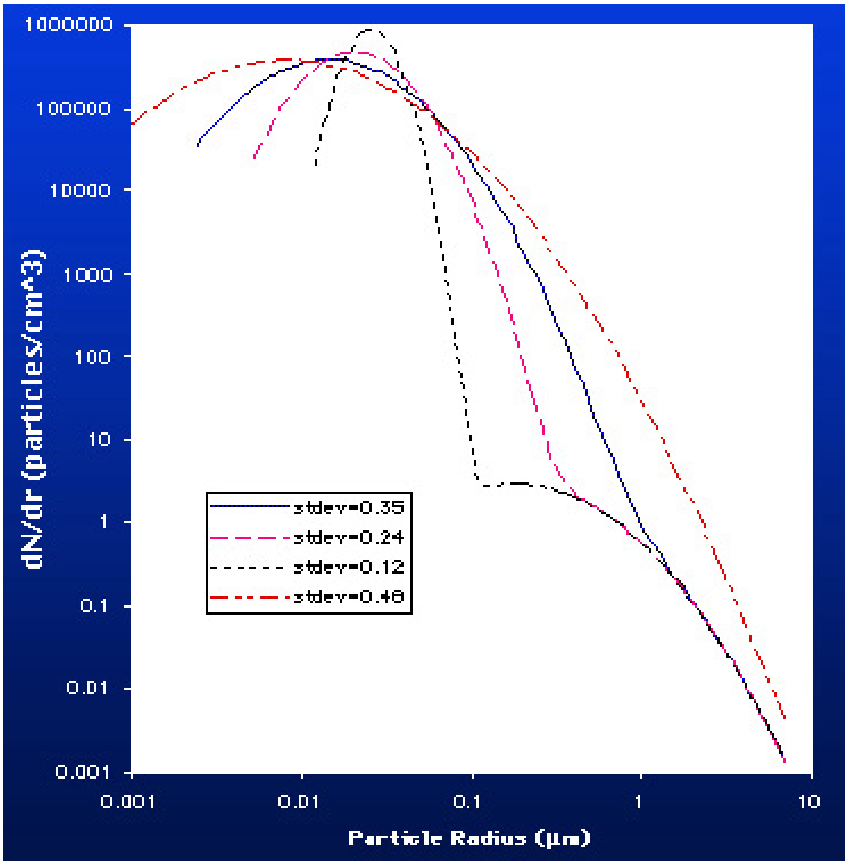

Figure 2.4-1. Typical particle size distribution curves for a rural aerosol type.

Since the presence of aerosols in the atmosphere can seriously degrade the accuracy of the surface radiative properties throughout the visible spectral bands, a robust and computationally feasible algorithm to extract aerosol properties from in-scene data would greatly enhance existing atmospheric correction techniques. The following sections briefly review existing algorithms for aerosol property determination from calibrated hyperspectral imagery.

2.4.2 The Fourier Transform Method

The construction of the Multi-angle Imaging Spectroradiometer (MISR) at JPL has motivated the development of algorithms that make use of the multidirectional viewing angles to better characterize the radiative properties of ground targets and the composition and contribution of the atmosphere in remote sensing. One of these techniques makes use of the spatial contrast in the acquired multiangle imagery and compares the amplitudes of the spatial Fourier transforms at all frequencies. An initial guess is made for the bulk optical aerosol properties, such as optical depth τ, single-scattering albedo *s*, and the size distribution. The Fourier components of the surface reflectance are compared to establish the quality of the first guess. Then the aerosol properties are subtly changed and the next guess is computed. The process is repeated until the RMS residuals indicate the best estimate of all aerosol properties. In all cases, the retrieval is constrained by the information provided by the multiangle imagery. The algorithm is unusable with nadir-only image acquisitions because of the need for multiple-angle data in the computations.

An assumption is made that the atmosphere is homogeneous over the image and that the surface albedo variations in that region can be utilized to estimate the aerosol properties. The governing radiative transfer equation for the directional surface reflectance inversion process is (Diner, 1985):

$$\begin{aligned} I(x,y) = R + e^{\frac{-\tau}{\mu}} \pi^{-1} \left[\int_0^1 \int_0^{2\pi} r(x,y)\; D\mu'\; d\mu'\; d\phi' \right] + \\ \pi^{-1} \int_0^1 \int_0^{2\pi} \int_0^1 \int_0^{2\pi} \left(T(x,y) * r(x,y)\; D\mu' \right) d\mu''\; d\phi''\; d\mu''\; d\phi'' \end{aligned} \tag{2-19}$$

where *x, y* are the spatial image coordinates, **R** is the path radiance, τ is the opacity of the atmosphere, **D** is the total radiance incident at the surface, **T** is the upward diffuse transmittance, **r** is the surface reflectance, μ is the cosine of the view angle, and * denotes convolution. All terms depend on view and sun angles and view azimuthal angle with respect to the sun position, where "view angle" is defined as the azimuthal angle between the sun and the along-track direction of the sensor. This equation can be restated in radiometric terms consistent with the notation of this paper:

$$L_{sensor} = L_u + \tau_2\; \rho\; \cos\sigma' \left[L_{grnd} + L_{downwelled} \right] + \left[T * \rho \left(L_{grnd} + L_{downwelled} \right) \cos\sigma' \right] \tag{2-20}$$

where σ' is the view angle of the surface to the incident radiance. The last term on the right describes the surface-leaving radiance being blurred by the diffuse-field point spread function (PSF) of the atmosphere. The filter theorem of the Fourier transform allows the convolution to be recast into a multiplication in the frequency domain. The spectrum of upward diffuse transmittance decreases in magnitude with increasing frequency and acts like a lowpass filter on the surface reflectance spatial structure.

The reflectance structure is modeled as:

$$\rho(\xi,\eta;\cos\sigma,\cos\sigma',\phi-\phi') = \rho^{0}(\xi,\eta;\cos\sigma) + \rho^{1}(\xi,\eta;\cos\sigma)\cos(\phi-\phi') \qquad (2\text{-}21)$$

$$\rho(0,0;\cos\sigma,\cos\sigma',\phi-\phi') = \mathrm{A}(\xi,\eta) * \rho_{n}(0,0;\xi,\cos\sigma',\phi-\phi') \qquad (2\text{-}22)$$

$$\rho_{n}(\xi,\eta) = \mathrm{A}(\xi,\eta) * \rho_{n}(\xi,\cos\sigma',\phi-\phi') \qquad (2\text{-}23)$$

where **A** is the transformed hemispherical albedo of the surface image and r is the 1-D normalized directional reflectance spectrum. It also can be shown that:

$$\left|\mathrm{A}(\xi,\eta)\right|\rho(\cos\sigma) =$$
$$\frac{\left|\mathrm{L}_{\text{sensor}}(\xi,\eta;\cos\sigma,\phi_1-\phi_0)\right|\mathrm{S}_1(\phi_2-\phi_0)}{e^{\frac{-\tau}{\cos\sigma}}\left[\mathrm{S}_1(\phi_2-\phi_0)-\mathrm{S}_1(\phi_1-\phi_0)\right]\mathrm{S}_0} - \frac{\left|\mathrm{L}_{\text{sensor}}(\xi,\eta;\cos\sigma,\phi_2-\phi_0)\right|\mathrm{S}_1(\phi_1-\phi_0)}{e^{\frac{-\tau}{\cos\sigma}}\left[\mathrm{S}_1(\phi_2-\phi_0)-\mathrm{S}_1(\phi_1-\phi_0)\right]\mathrm{S}_0}$$
$$(2\text{-}24)$$

where the S-functions are the components of the atmospheric optical transfer function (OTF) which suppress high-frequency information. Analysis of complex-valued parameters is avoided by taking absolute values. Equation (2-24) is the radiative transfer function that is iterated to retrieve **A** and uses two distinct azimuthal observation angles.

The Simplified Algorithm (Martonchik, 1992)

1) The algorithm first estimates the aerosol opacity, single-scattering albedo, and phase function. The corresponding upwelled radiance (L_u), upward diffuse transmittance (T), and total downward directed radiance (L_{grnd}+$L_{downwelled}$) are then computed.

2) The DC component of the Fourier transform of the multi-angle images is used to iterate on the Fourier transform of Equation (2-19) by substituting in Equation 2-21 for *r* to solve for $A(0, 0)\rho^0$ and $A(0, 0)\rho^1$. The surface reflectance structure $\rho(0, 0)$ is constructed via Equation (2-22) and used to update $L_{grnd}+L_{downwelled}$ and to recalculate the suppression functions S_0 and S_1. The iteration procedure continues until the value of $L_{grnd}+L_{downwelled}$ converges.

3) At nonzero spatial frequencies, solve for $|A(\xi, \eta)|\rho^0$ and $|A(\xi, \eta)|\rho^1$ by using Equation (2-24). The surface structure is incrementally constructed using Equation (2-23) in the multi-angle acquisition and tracking the RMS residuals between the curves at all spatial frequencies. The average of the aerosol parameter at the minimum residual for each curve gives the "best" estimate of the scene atmosphere. This is illustrated in Figures 2.4-2 and 2.4-3. The frequency representation of reflectance corresponding to the best estimate for all parameters is then transformed to the space domain to produce the best estimate of the reflectance value in each pixel of the image.

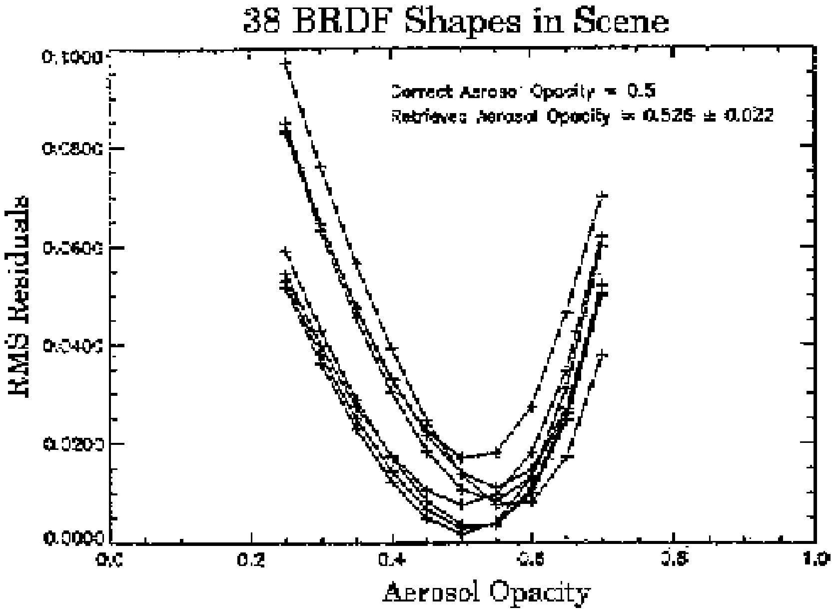

Figure 2.4-2. Retrieved directional reflectance shape residuals for various spatial wave numbers (Martonchik, 1992).

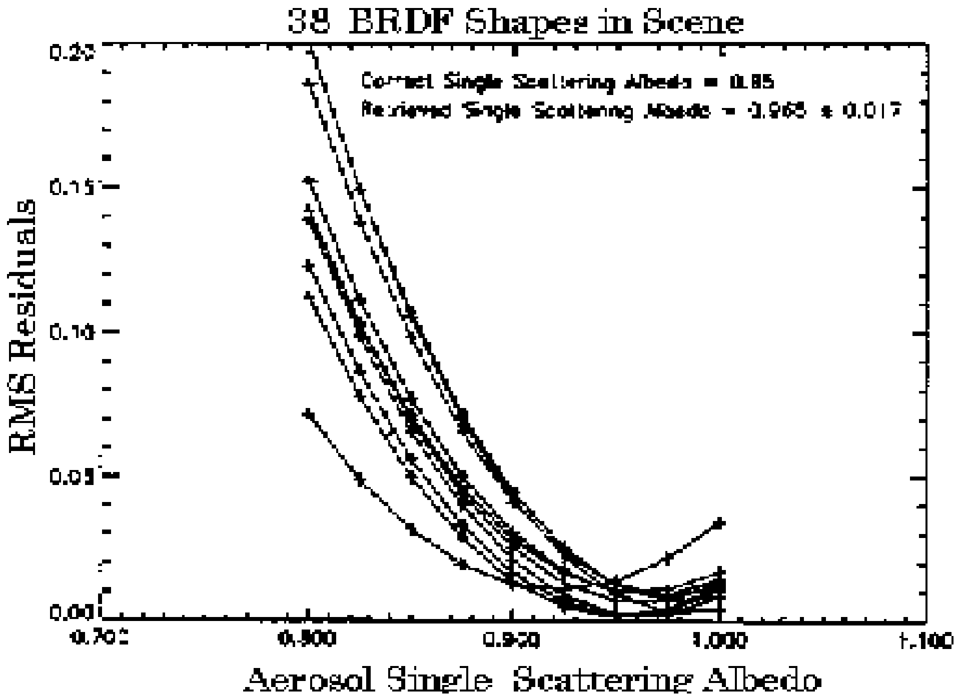

Figure 2.4-3. Retrieved directional reflectance shape residuals for various spatial wave numbers (Martonchik, 1992).

It should be noted that this procedure must be realized within individual wavelength bands and must be repeated for each band when a multiangle hyperspectral image is analyzed. This routine was tested for synthetic imagery having two fixed aerosol parameters with very good results (Figures 2.4-2 and 2.4-3). No results of a test where three aerosol parameters were varied are documented in the literature.

2.4.3 The Principal Components Method

This routine for retrieving aerosol properties from remotely sensed imagery was developed by the same authors who constructed the Fourier Transform method reviewed in section 2.4.2 (Martonchik, 1992). In the Fourier Transform method, angle-dependent power functions of the nonzero frequencies were used to construct empirical orthogonal functions (EOFs) which described the surface component of the observed radiance (Martonchik, 1996). The best estimate of the aerosol optical depth was that which minimized the residuals between the observed (sensor) radiances and the modeled radiances computed using the EOF expansion of the total at-the-surface radiance. In this technique, the FFT is unnecessary and the EOFs are constructed directly from the individual pixel radiances in the image.

In this algorithm, the governing radiative transfer equation is simply written as:

$$L_{sensor}(x,y) = L_{atm} + L_{direct}(x,y) + L_{diffuse} \tag{2-25}$$

where L_{atm} is the path radiance, L_{direct} is the direct solar radiance component from the surface to the sensor, and $L_{diffuse}$ is the diffuse radiance from the surface to the sensor. All three terms depend on the observer-view and sun angles and observer-azimuth angle with respect to sun position. Only the direct radiance component is considered to vary spatially in this radiative transfer function (RTF).

The image scene is divided into 4x4 pixel subscenes and the aerosol is estimated for each. Since aerosol loading is assumed to be constant over the entire image, the results for all subscenes are averaged at the end. The EOFs required to run the aerosol algorithm are the eigenvectors associated with the real-valued, scatter matrix. These eigenvectors are constructed from the reduced pixel radiances. Reduced pixel radiances are defined as the sensor radiance value of the pixel minus the average radiance of the pixel-averaged 4x4 subscene in which it is located. The assumption is that this process removes the path and the diffuse radiance which are assumed identical for each pixel in the subscene. Thus, the reduced pixel radiance is given by:

$$L_{reduced}(x,y) = L_{sensor}(x,y) - \frac{1}{16}\sum_{i=1}^{4}\sum_{j=1}^{4} L_{sensor}(i,j) \tag{2-26}$$

over the 4x4 image subsection where *i, j* are the pixel coordinates within the subsection. The scatter matrix can be constructed where each element can be represented as:

$$C_{pq} = \sum_{x}\sum_{y} L_{reduced}(x,y,p) L_{reduced}(x,y,q) \tag{2-27}$$

where p, q are used to indicate different viewing geometries. The eigenvectors of C are the solutions to the equation:

$$\sum_{q=1}^{10} C_{p,q} f_{n,q} = \lambda_n f_{n,p} \qquad (2\text{-}28)$$

The λ_n's are the real, positive eigenvalues of f_n. Since MISR has five forward and five rearward camera look angles, there is a total of ten eigenvectors and associated eigenvalues. Every image pixel would have a ten-element vector of reduced radiances and could be expanded in terms of an orthonormal set:

$$L_{reduced}(x, y, p) = \sum_{n=1}^{10} A_n^{x,y} f_{n,p} \qquad (2\text{-}29)$$

where the **A** matrix contains the principal components of the reduced radiance multiangle vector.

If a single spatially variable surface bidirectional reflectance factor (BRF) is said to be a descriptor of the view angle variability of a surface within an image subsection (individual pixel reflectances can still differ), the reduced pixel radiances obey the linear relation:

$$L_{reduced}(x, y, p) = c' \; L_{reduced}(x', y', p) = c \;\; f_{1,p} \qquad (2\text{-}30)$$

Thus, it follows that if the correct path radiance and diffusely transmitted radiances are subtracted from the average radiance at the sensor (in the 4x4 subsection), then the resulting pixel-averaged surface function must also be proportional to f_1:

$$\overline{L}_{sensor,i} - L_{atm,i} - L_{diffuse,i} = a_1 f_{1,i} \qquad (2\text{-}31)$$

When the correct aerosol parameters are unknown, the best estimate of the parameters is the minimum least-squares difference between the left and right side of Equation (2-31). This can be expressed as:

$$D(\text{mod el},\tau_{aer}) = \sum_{i=1}^{10}\left(\overline{L}_{sensor,i} - L_{atm,i}(\text{mod el},\tau_{aer}) - L_{diffuse,i}(\text{mod el},\tau_{aer}) - \sum_{n=1}^{N} a_n f_{n,i}\right)^2$$

(2-32)

with the expansion coefficients obtained from:

$$a_n = \sum_{i=1}^{10}\left(\overline{L}_{sensor,i} - L_{atm,i}(\text{mod el},\tau_{aer}) - L_{diffuse,i}(\text{mod el},\tau_{aer})\right) f_{n,i} \qquad \text{(2-33)}$$

Only eigenvalues greater than $0.05l_1$ are used in the summation, (*i.e.*, $N_{max}<10$). The minimum **D** corresponds to the best estimate of optical depth for that N. The best overall aerosol optical depth for the image subsection is obtained by a weighted average over all N optical depths:

$$\tau_{best} = \frac{\left(\sum_{N=1}^{N_{Max}} \frac{1}{D^{N}} \tau_N\right)}{\left(\sum_{N=1}^{N_{Max}} \frac{1}{D^{N}}\right)} \qquad \text{(2-34)}$$

and:

$$D_{eff} = \frac{N}{\sum_{N=1}^{N_{Max}} D^{-N}} \qquad \text{(2-35)}$$

A weighted average using the aerosol optical depth and corresponding $\mathbf{D_{eff}}$ is then computed for all 16-pixel subsections in the image.

In preliminary tests, the algorithm appeared to extract realistic aerosol optical depths for the multiangle scene tested. Since no atmospheric truth data were obtained for the image acquisition, the algorithmic procedure cannot be considered as validated.

This concludes the listing of aerosol extraction algorithms available for hyperspectral imagery. Of these, only the NLLSSF technique has been used with actual image data with some success. The aerosol NLLSSF algorithm by Green, (1989) has the advantage in that it extracts the visibility parameter of aerosols and assumes a fixed standard deviation of the particle distribution. However, the user must assume some particular set of atmospheric aerosols such as an urban, rural, maritime, or other MODTRAN aerosol mixture.

The Fourier transform technique, while novel in its approach, is too computationally intensive to incorporate into a total atmospheric algorithm. The Principal Component approach may prove to be robust enough and computationally realistic for total atmospheric correction, but it depends on the multiple-view angle imagery that only the MISR sensor can provide. The intriguing aspect of this approach is its use of a spatially blurred image as part of the determination of atmospheric aerosols. Since aerosols cause the most scattering of light in the visible region, the incorporation of this phenomenon in the fit of aerosol bulk properties may be important.

While the Principal Component method may be useful, it is as yet untested and is applicable only to MISR imagery (multiangle and multispectral). What is sorely needed is an algorithm that can be utilized with more common types of sensors, such as line scanners.

For reasons previously stated, none of the aerosol algorithms are planned to be used with the exception of the NLLSSF technique which may be part of larger, more comprehensive aerosol extraction routine.

2.5 Review of the Radiative Transfer Process

Before reviewing the comprehensive atmospheric correction algorithm in detail, it is useful to describe the paths of photons that transfer solar energy since both APDA and NLLSSF use this radiometry to estimate the atmospheric component(s). This is key because well-modeled radiometry can be applied to the sensor radiance so that the atmospheric correction algorithm can derive an estimated ground reflectance.

Given the surface elevation, columnar water vapor, and visibility for a hyperspectral image, the radiometric parameters can then be retrieved from an LUT generated previously by multiple MODTRAN 4 runs. The radiometric parameters used in the LUT will be defined in this section along with the radiative transfer process. Then the construction of the actual LUT will be described in Section 2.6.

Since all work in this research is done in the visible and near-infrared regions, the thermal emissive contributions to the total sensor radiance are assumed to be zero. There is also the assumption that no shape factor is present due to objects or terrain and that the spectral reflectance properties of the surface or target are Lambertian. In the simple single scattering case, the total radiative transfer equation reduces to:

$$L_{sensor} = L_{grnd} \rho + L_{upwelled} \tag{2-36}$$

where L_{sensor} is the total radiance measured at the sensor by a detector element, L_{grnd} is the direct solar radiance from the sun to the target to the sensor (including transmissive effects of the atmosphere as shown in Figure 2.5-1),

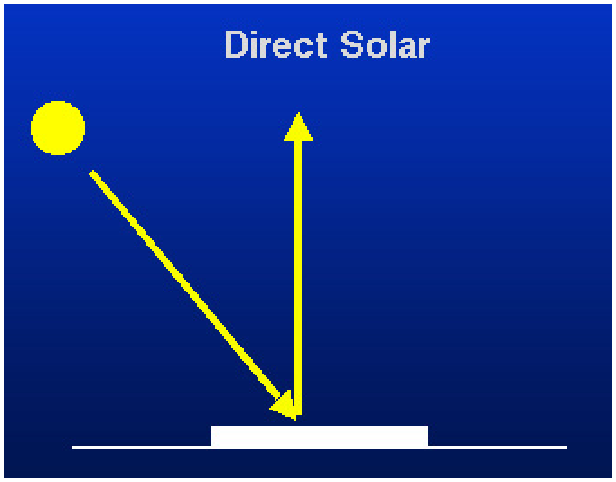

Figure 2.5-1. Direct solar radiance path.

ρ is the surface reflectance of the target, and L_u is the upwelled atmospheric radiance which has no interaction with the target or surround (Figure 2.5-2). All of these terms are functions of wavelength.

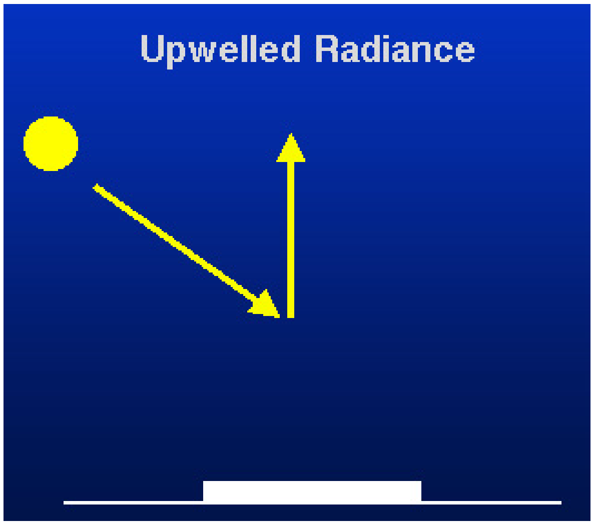

Figure 2.5-2. Atmospheric scattered upwelling radiance

If the earth's atmosphere caused only a single scattering event per photon, the work of a remote sensing scientist would be a lot less challenging. However, earthbound photons in the ultraviolet and visible portions of the spectrum frequently are scattered two or more times before they reach the sensor because of molecular interaction (Rayleigh scattering), aerosols (Mie scattering), and a Rayleigh-aerosol coupled interaction. Modeling this multiple scattering in the radiative transfer equation warrants the inclusion of additional terms to account for non-target direct solar photons that scatter into the sensor path:

$$L_{sensor} = \frac{\left(L_{grnd} + L_{downwelled}\right)\rho}{(1.0 - \rho S)} + L_{upwelled} + \sum_{h=0}^{sensor\_height} \sum_{\theta=0}^{\frac{\pi}{2}} \sum_{\phi=0}^{2\pi} \rho(\theta, \phi) L_{env}(\theta, \phi, h) \qquad (2\text{-}37)$$

where $L_{downwelled}$ is the scattered atmospheric radiance onto the target including transmissive effects of the atmosphere,

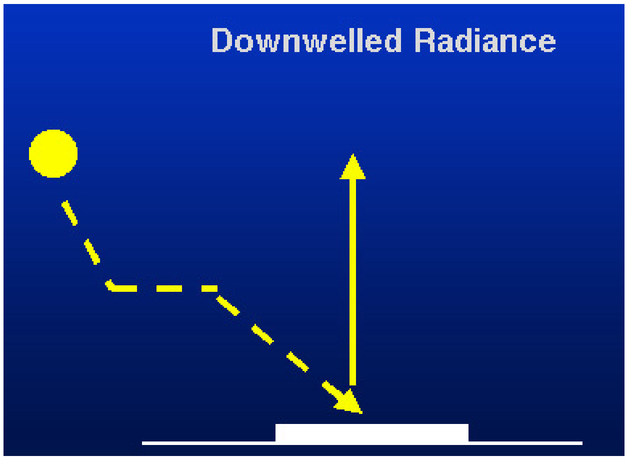

Figure 2.5-3. Scattered solar downwelling radiance.

S is the spherical albedo of the atmosphere, (1.0-ρS) in the denominator is derived from a series that accounts for successive reflections and scattering between the surface and the atmosphere (Vermote, E. et al., 1997) also called the trapping effect (Figure 2.5-4).

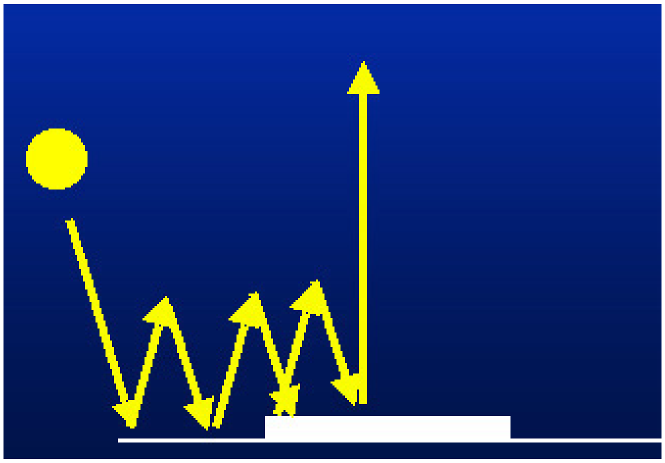

Figure 2.5-4. Trapping effect radiance.

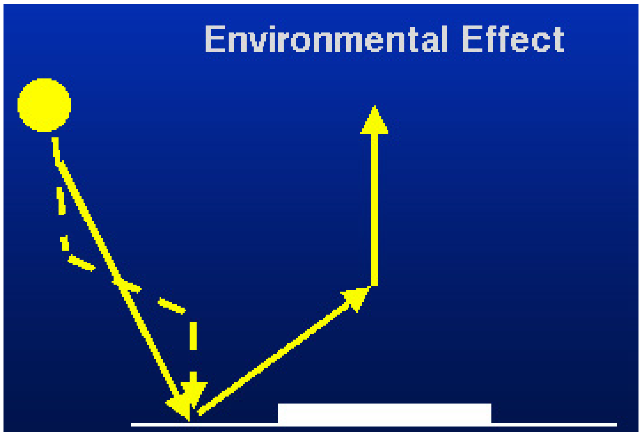

Figure 2.5-5. Environmental or adjacency radiance.

L_{env} is the direct and scattered solar radiance that interacts with a surround area with reflectance $\rho(\theta,\phi)$ and is scattered into the target-sensor path (Figure 2.5-5), θ is the angle from nadir (looking downward from the sensor) to where the surround area is located, and ϕ is the azimuthal angle where the surround area is located.

The last term in the summation Equation 2-37 is often referred to as the "environmental or adjacency effect radiance" because it includes photon interactions with ground areas outside of the target. Presently in MODTRAN 4.0 radiative transfer calculations, the reflectance of the surround areas are assumed to be equal to that of the target area. For homogeneous land cover areas this assumption holds true, but usually not with most scene content. This problem leads to one of the efforts in this research, since there appears to be a lack of algorithms that account for a spatially nonhomogeneous reflective surround . In terms of the atmospheric optical effect, the question becomes: What is the atmospheric point spread function (PSF)?

To account for nonhomogeneity in the surround of the scene, it is useful to visualize a ground-projected block or grid of sensor pixels with each having reflectance $\rho(\theta,\phi)$). This block is spatially weighted to account for the scattered fraction of radiance received at the sensor in its instantaneous field of view (IFOV); see Figure 2.5-6. The resulting sum of the spatially weighted $\rho(\theta,\phi)$) values is the average reflectance (ρ_{avg}). The grid of spatial weights can be thought of as the estimate of the atmospheric PSF since the "point" or projected area of the detector element receives energy from outside of the confines of the sensor IFOV.

$$\rho_{avg} = \sum_{i}\sum_{j} W(i,j)\rho(i,j) \tag{2-38}$$

Note: In Equation 2-38 the Cartesian coordinates (i,j) have been substituted for polar coordinates of the ground pixels (θ,ϕ).

The value of the environmental/adjacency radiance at the sensor reflected from a 100% reflector (L_{env}) can then be extracted from MODTRAN (given fixed atmospheric parameters) and multiplied by this average reflectance of the surround to yield the estimated adjacency-effect radiance. Since the trapping-effect radiance also includes interaction with the surround, the average reflectance can also be substituted for ρ in the series. After a numerical estimate is substituted for the series, the radiative transfer equation becomes:

$$L_{sensor} = \frac{\left(L_{grnd} + L_{downwelled}\right)\rho}{(1.0 - \rho_{avg} S)} + L_{upwelled} + \rho_{avg} L_{env} \tag{2-39}$$

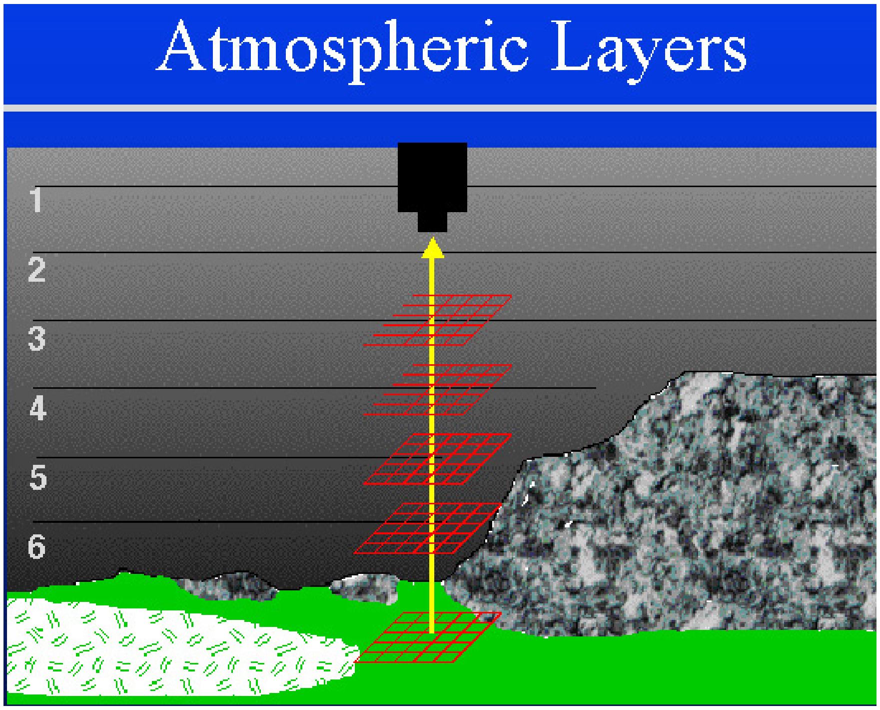

Figure 2.5-6. The sensor ground-projected pixel grids containing the fractional contributions of the ground reflectance at each atmospheric layer height. These grids are summed over the layers to eventually generate the spatial weighting for the ground reflectance.

The assumption of use of the average reflectance is valid only if the target is not much darker than the surround. If a dark target lies on a bright surround, the actual trapping effect radiance will be very small since the last photon interactions result in reflection of a very small percentage of the trapped radiance. As a side note, even though the same PSF was used for the trapping effect in Equation 2-39 (i.e the $\rho=\rho_{avg}$ substitution), it is known that the trapping effect PSF is much larger and broader. Further research in this area could be performed to develop the weighting (and kernel size) for better estimation of the gain effect in trapping effect radiance.

Solving Equation 2-39 for the ground reflectance of the target yields the equation:

$$\rho = \frac{\left(L_{sensor} - L_{upwelled} - \rho_{avg} L_{env}\right)\left(1.0 - \rho_{avg} S\right)}{\left(L_{grnd} + L_{downwelled}\right)} \tag{2-40}$$

Equation 2-39 and its complement 2-40 is included as a choice for the radiative transfer equation in the comprehensive atmospheric correction algorithm. In the event that the user does not wish to include the L_{env} radiometric parameter, an alternative governing equation for a single pass through the algorithm may be selected:

$$L_{sensor} = \frac{\left(L_{grnd} + L_{downwelled} \quad \tau_2\right)\rho}{(1.0 - \rho\ S)} + L_{upwelled} \qquad (2\text{-}41)$$

As inferred in Equation 2-38, to estimate ρ_{avg}, it is necessary to already have a spectral reflectance map. This requires t a first pass through the atmospheric correction code where ρ_{avg} is assumed to be equal to the target reflectance within the sensor IFOV. Once the radiometric parameters are determined by locking in the surface elevation, aerosol dependent visibility, and columnar water vapor amount (via iterations with NLLSSF, APDA, or another technique), Equation (2-39) may be inverted to solve for the target reflectance for the first run by substituting $\rho=\rho_{avg}$:

$$\rho = \frac{\left(L_{sensor} - L_{upwelled}\right)}{\left(L_{grnd} + L_{downwelled} + L_{env}\right) + \left(L_{sensor} - L_{upwelled}\right)S} \qquad (2\text{-}42)$$

This first-pass reflectance map becomes either the end product or the map that contains $\rho(i,j)$ values for use in Equation 2-38. The last step in the first run is the determination of the spectral atmospheric PSF (or W(i,j)) that dictates the amount of blur that is applied image-wide (and band-by-band) to the first-pass reflectance map (see Section 3.5) via convolution. The first pass reflectance map convolved with the PSF is then used for ρ_{avg} in the second run. Once the average reflectance map ρ_{avg} is derived, the second pass through the correction algorithm uses Equation 2-40 for the inversion-to-ground-reflectance formula.

The next section addresses the generation of the Look-Up Table (LUT) with MODTRAN 4.0 that contains the radiometric parameters for different atmospheres as well as a general overview of the atmospheric correction algorithm.

2.6 The Radiometry LUT and the Atmospheric Correction Algorithm

In order to finally solve Equation 2-40 or 2-42 for estimated ground reflectance, a quick overview is needed of the steps in the comprehensive atmospheric correction algorithm. First, a radiometrically calibrated hyperspectral image is chosen to invert to obtain the ground reflectance. Secondly, an estimated atmospheric profile is chosen and the necessary parameters needed to construct a MODTRAN carddeck are substituted, either from measurement or estimates by the user. This becomes the base carddeck to use for making a full LUT.

Since NLLSSF, APDA, and the techniques developed in this research attempt to fit the estimated radiance profile at the sensor (see Section 2.3.1 and 2.3.2), a number of atmospheric conditions with their associated radiometric parameters must be determined. It must be remembered that if the surface elevation (or surface-pressure-depth), visibility, or water-vapor amount is changed, then the radiative transfer terms in the atmosphere also change. Thus, for the purposes of this correction algorithm, the LUT must contain all radiometric parameters in Equation 2-40 for each combination of surface elevations, visibilities, and water vapor amounts as functions of wavelength.

To begin, a range and increment step is chosen for each atmospheric parameter to be solved. For example, the range ofsurface elevations can be from 0.0 km to 0.8 km in 0.1 km increments, the visibility from 10.0 to 70.0km in 10 km increments, and the water vapor from 0.0 to 5.5g/cm^2 in 0.75 g/cm^2 increments. For every combination, the base MODTRAN carddeck is altered , a run of MODTRAN is performed, the radiometric parameters are convolved with the sensor response, the radiometric parameters needed for Equation 2-39 are linked with the atmospheric parameter combination and then are placed in an organized data structure as the LUT. The LUT becomes a complete database of radiometry that can easily be accessed for any specific combination of surface elevation, visibility, and water vapor. Combinations that fall in between the discrete intervals can be interpolated to obtain the necessary radiometry.

Once the LUT has been completed, the first pass of the comprehensive algorithm can begin. The user can select which techniques to use to solve for surface elevation, visibility, and water vapor. For this example, a user may select NLLSSF to solve all three atmospheric parameters. The algorithm proceeds to Box A in Figure 2.6-1 and NLLSSF is used to solve for the surface elevation of each pixel. The procedure repeats until all the pixels in the image have been assigned a surface elevation.

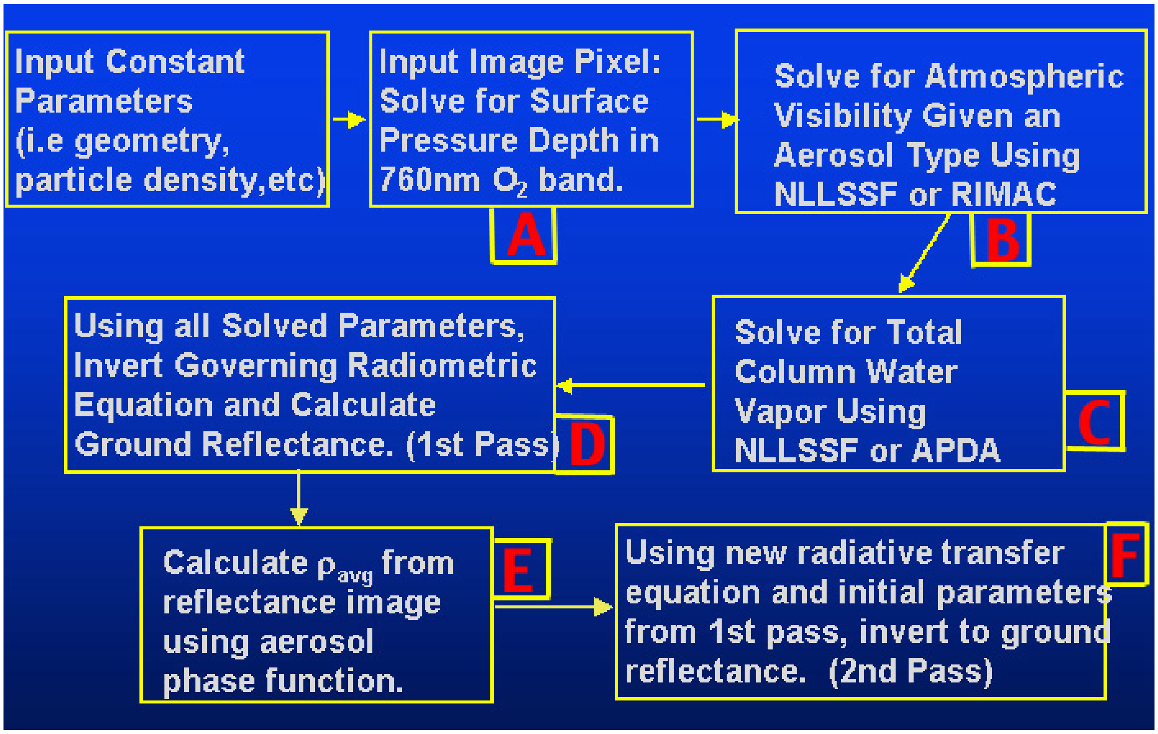

Figure 2.6-1. Overview of the atmospheric correction algorithm.

NLLSSF iterates through the LUT the surface elevation dimension to find the combination of radiometric parameters that will minimize the error between the image pixel radiance and Equation 2-39, where $\rho_{avg}=\rho$ is assumed. The aerosol-dependent visibility and columnar water vapor must be estimated by the user for this step, usually by using one value fo rthe entire image (for each parameter). As stated in Section 2.3.2, the NLLSSF routine must begin close to the truth for convergence to a realistic solution.

With the surface elevation fixed, the algorithm moves to Box B in Figure 2.6-1 where the NLLSSF solves for the aerosol-dependent visibility. The visibility that results in the least radiance error for an image radiance value is used. The algorithm assigns a visibility to each pixel. At this point, it is easy to see that essentially the algorithm moves through the 3-D LUT by constraining one dimension after another to converge on the best "atmosphere" for the image pixel.

With the surface elevation and visibility fixed, the NLLSSF goes to Box C in Figure 2.6-1 where it iterates on the atmospheres until the best fit is found for the water vapor feature at 940nm. Again, the algorithm proceeds through the image pixel-by-pixel to assign a water vapor to each pixel. The algorithm then proceeds to Box D in Figure 2.6-1 where it extracts the radiometric parameters from the LUT that correspond to the solved surface elevation, visibility, and water vapor from the previous three steps. Equation 2-42 is used to solve for the ground reflectance. Once the recovered spectral reflectance is written to an image file for each pixel, the first pass is complete.

The next step is to calculate the atmospheric PSF (see Section 3.5) and convolve this with the first-pass reflectance image to yield a ρ_{avg} image (Box E). Once complete, the algorithm repeats starting from Box A in Figure 2.6-1 using Equation 2-39 to fit the image pixel (sensor) radiance. At Box D, the algorithm then uses Equation 2-40 to solve for reflectance (for each pixel) using the radiometric terms that correspond to the fixed atmospheric parameters obtained in the second pass.

3. Components of the Atmospheric Correction Algorithm

3.1 Overview of the Complete Algorithm

The APDA and NLLSSF technique were reviewed in Section 2.3 and the comprehensive atmospheric correction algorithm was presented in Sections 2.5 and 2.6. Since the existing components have been described previously, it is necessary to establish some order in the computations of parameters. The sequence of the atmospheric characterization thus consists of the following steps:

1) estimation of terrain height
2) determination of aerosol properties (by estimating the atmospheric visibility and defining an aerosol type),
3) extraction of total column water vapor, and
4) estimation of the atmospheric PSF to account for surround effects.

(Note: From numerous trials, it has been determined that the aerosol properties must be computed before estimating the water vapor estimation so that the atmospheric "windows" (i.e. the wings) around the .94μm water vapor feature at .86μm and 1.0μm have a better fit to the sensor radiance.)

Before exploring the composition of this atmospheric correction algorithm further reasons for its development must be stated. First and foremost, the remote sensing community needs a comprehensive atmospheric correction algorithm to obtain estimated ground reflectance from calibrated multispectral and hyperspectral images. A second reason is that there is no comprehensive correction algorithm that contains a large assortment of options for inverting sensor radiance measurements to ground reflectance. The options such as APDA and NLLSSF are not presently available in modular and useable forms. The third reason for this algorithm is that in addition to including a large assortment of correction approaches, a new technique for determining atmospheric visibility (and subsequently the aerosol properties) called the Regression Intersection Method for Aerosol Correction (RIMAC) has been developed to work in this modular environment. The last reason is that a new method for determining the contribution of the target surround is presented which uses the built-in functionality of MODTRAN 4. This new method has the potential for being able to use a generic set of PSFs given that the atmospheric layer profile has relative humidities less than 95%.

With these reasons being established for a foundation, the components and atmospheric characterization sequence in this atmospheric correction algorithm can be reviewed.

Figure 3.1-1 presents the atmospheric correction or inversion algorithm modules. The atmosphere PSF routine is considered an intermediate step and is included in Figure 2.6-1. The following list is a breakdown of the options available in the algorithm for solving for three atmospheric parameters:

Parameter	Options
Surface elevation	Default or truth data
	NLLSSF (fits O_2 band)
Aerosol-Dependent Visibility	Default or truth data
	NLLSSF (fits .4-.7µm bands)
	RIMAC (fits .55-.7µm bands)
Columnar Water Vapor	Default or truth data
	NLLSSF (fits H_2O band)
	APDA (fits H_2O band)

Other options include the user's choice of one of two passes through the algorithm and choices of radiative transfer equations (see Section 2.5). From Figure 3.1-1, it can be seen how the options are combined to obtain the best model of the atmosphere given the image pixel radiance. The algorithm then proceeds to invert the sensor radiance to ground reflectance.

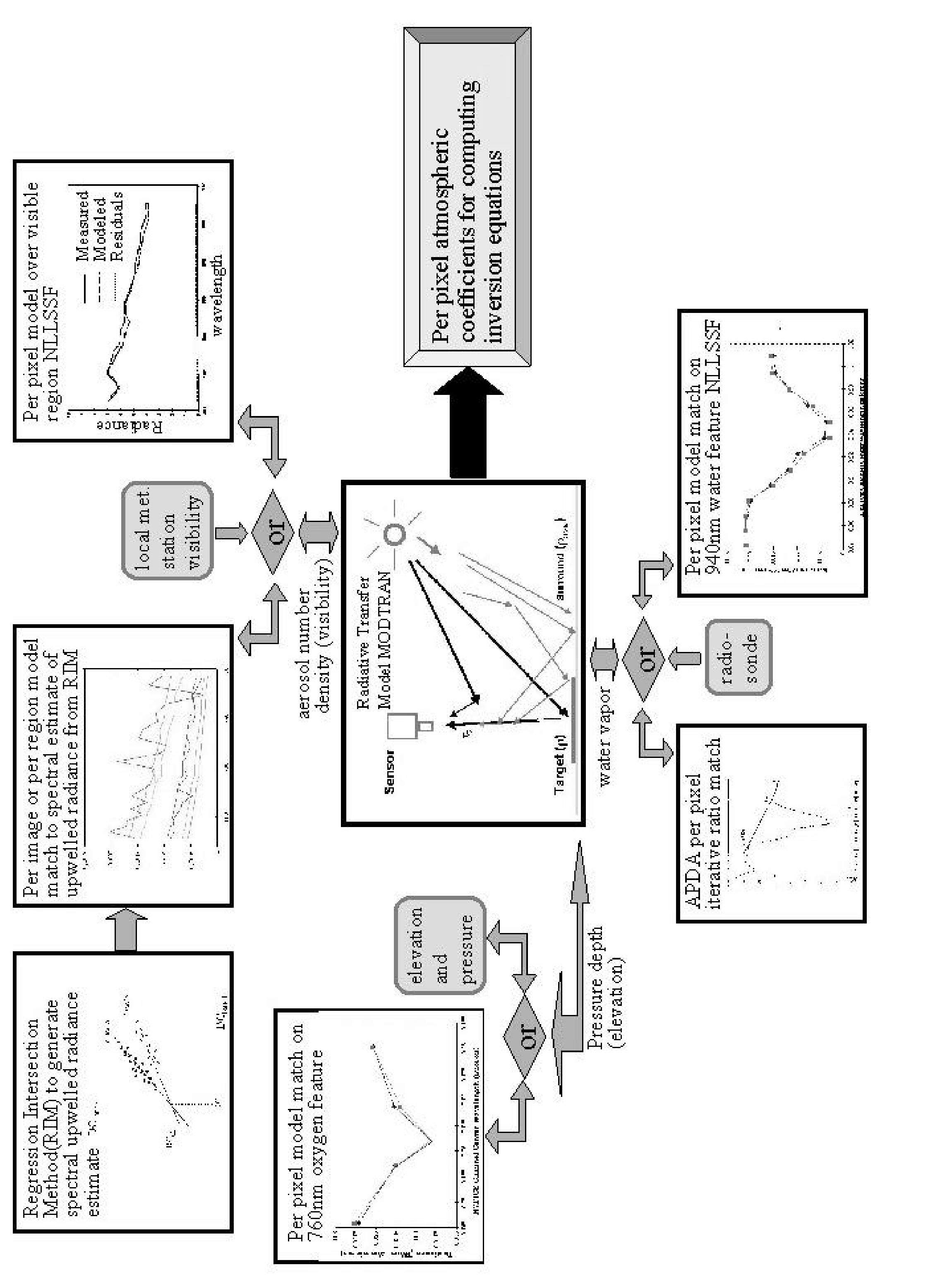

Figure 3.1-1. The components of atmospheric correction and their flow to derive the estimated ground reflectance (illustration courtesy of Nina Raqueño)

In all references to reflectance units in this research, the range is assumed to be 0.0 to 1.0 reflectance units. Zero reflectance is a completely black non-reflecting target, while a reflectance of 1.0 means that the target reflects 100% of the incident light.

3.2 Terrain Height

Only Green's method of NLLSSF is used to calculate the surface pressure elevation (Section 3.3.2). Using the 760nm oxygen absorption band, an iterative routine is employed to fit the model sensor radiance from MODTRAN to the acquired spectral radiance data for each pixel (left middle module in Figure 3.1-1). The reflectance is modeled with a gain and bias as a function of wavelength. A preconditioning step prior to running the amoeba routine performs a fast linear fit between the first and last channel of the oxygen bands to initialize the reflectance gain and bias using the atmospheric defaults.

This routine is incorporated into the new atmospheric correction routine as the first step. If the surface elevation is known, this NLLSSF module can be switched off and a default elevation used instead.

3.3 Aerosols

One option to determine the atmospheric visibility given an aerosol type is Green's NLLSSF (in top right Figure 3.1-1). Once again, a pre-conditioning step is run to initialize the amoeba routine. The default atmospheric condition radiometric parameters are used, except the surface elevation is set to the solution of the previous step. The reflectance is linearly modeled with the 400nm and 700nm bands and the vegetation scalar is found by multiplying the NDVI by 2.5. This multiplier for the NDVI is an empirically-derived value that appears to give a fairly accurate vegetation fraction on a per-pixel basis. The multiplier is meant to help estimate in a pre-conditioning step and is not used to compute the final vegetation scalar in the actual fit routine. The reflectance is modeled with a gain, bias, and a spectral scaled vegetation reflectance curve to compensate for the non-linear chlorophyll reflectance as a function of wavelength. The NLLSSF is then used on all the bands in the range from 400nm - 700nm. As in the previous subsection, a default value for visibility can be used instead.

3.3.1 Non-Unique Radiometric Solutions for Aerosols

The original proposed goal in this area of research was to develop an inscene algorithm to extract the bulk atmospheric aerosol properties from the image. Before this effort was undertaken, it was deemed prudent to investigate how the microproperties of the aerosols affect the macroscopic property of radiance at the sensor and the subsequent recovery of true surface reflectance. The ideal case was chosen where the atmosphere was generated by MODTRAN and the parameters were used to invert to ground reflectance.

To set up this test, a standard rural aerosol model was chosen with a number density that matched a 15km meteorological visibility for 70% relative humidity. The MODTRAN radiometry using the default mode radius and standard deviation for the small and large particle aerosol component was used as "truth":

	Small Aerosol	Large Aerosol
Mode Radius	0.02846µm	0.4571µm
St. Deviation	0.35µm	0.4µm
Number density	27037 p/cm^3	3.38 p/cm^3

Cases where other combinations of aerosol number density and standard deviation were sought that could invert from sensor radiance to reflectance with no greater error than 0.01 reflectance units. A rural aerosol was chosen that corresponded to 12.5 km visibility at 70% relative humidity with particle density of 30945 particles/cm^3 for the small particle and 3.87/cm^3 for the large particle. The standard deviation of the small particle density was changed until the reflectance inversion error from "truth" matched the given tolerance. This same procedure was followed for aerosol number density for a visibility of 17 km: 23911 small particle, 2.99 large particle. The mode radii remained at the MODTRAN default for 70% humidity conditions. After many MODTRAN runs with different user-defined aerosols specified in Card 2D2, the recovered reflectance error tolerances for an average 0.18 albedo ground target were found. The limits were an “equivalent” aerosol atmosphere in the 12.5 km visibility case with σ=0.34µm standard deviation and in the 17 km visibility case σ=0.36µm standard deviation.

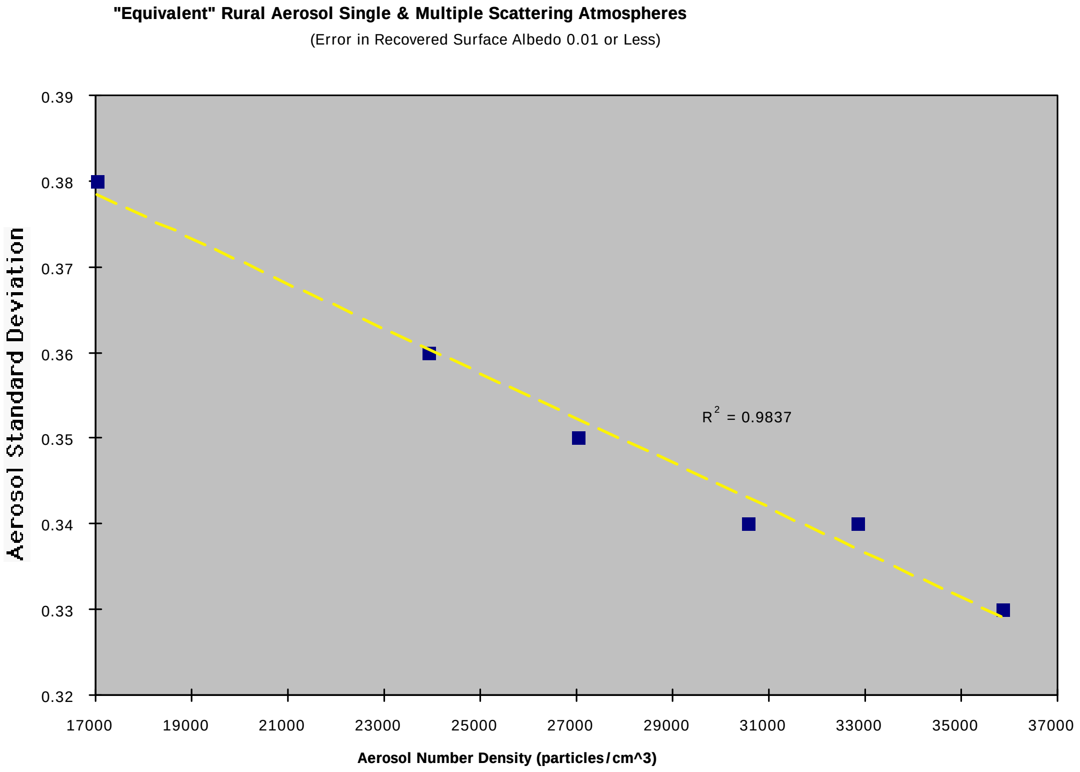

Figure 3.3.1-1. The regression line shows the non-unique combinations of aerosol standard deviation and number density that yield equivalent atmospheres at 410nm.

Figure 3.3.1-1 shows a plot of the equivalent aerosol parameters that could be used as a LUT in the spectral region of 410nm where the majority of scattering due to aerosols takes place. Thus, by choosing a number density (*e.g.,* visibility parameter) between the two extremes, you could find a suitable standard deviation that would compute the ground reflectance from the sensor radiance within 0.01 reflectance units. Assuming the MODTRAN model of the atmosphere is true, the data show that there are non-unique aerosol properties that can yield the "same" radiance at the sensor. For a range of atmospheres, it is not necessary to devise a complex and run-time intensive algorithm to solve for non-unique bulk aerosol properties. A quantitative solution to the radiative transfer equation can be found using an "equivalent" aerosol property(s) essentially by employing the already fixed aerosol distribution standard deviation in MODTRAN and then simply changing the relative humidity and visibility parameters. It should be noted that the visibility parameter is closely related to the aerosol particle number density and humidity

(Shettle & Fenn, 1979). For the scope of this research, it was determined that solving for aerosol visibility is sufficient for non-unique determination of the bulk properties.

3.3.2 The Regression Intersection Method for Aerosol Correction (RIMAC)

A new in-scene option for estimating the atmospheric aerosols via the visibility (see at the top left in Figure 3.1-1) is the Regression Intersection Method for Aerosol Correction (RIMAC). Derived from the Regression Intersection Method to estimate atmospheric upwelled radiance (Crippen, 1987) (Gaddis et al., 1996), this technique assumes that the majority of the upwelled radiance is a function of aerosol scattering in the 550nm - 700nm wavelength range. A substantial advantage of utilizing RIM is that it provides statistically derived results from the actual image data with no atmospheric or other scene information needed. By comparison, the NLLSSF technique relies on a starting estimate that is close to truth in order to obtain realistic atmospheric parameters and subsequently yield a good inversion to reflectance. NLLSSF also is constrained by the reflectance modeled as a linear function of wavelength for a given band range (with some nonlinearity accounted for in specific bands).

The RIM depends on classification that can identify homogeneous areas of varying spectral contrasts in the terrain. Lack of spectral contrast can lead to gross errors in the estimated upwelled radiance. The method also assumes that the spectral bands are inherently registered. As implemented, an unsupervised ISODATA classification is done by a noninteractive ENVI calculation or a previously constructed supervised classification map is used to define class regions of homogeneity. Ineligible class distributions are identified for lack of compactness by using a standard deviation cutoff for each band (Barnes, 1997). Once ineligible distributions are discarded, the spectral digital counts (DC) of the image are loaded for each of the classes. Starting from the first band and using band pairs, a regression is performed on the DCs for each class to extrapolate toward the origin and the intersections of all the class regressions are calculated from the combinations of the first band with the others (Figure 3.3-1).

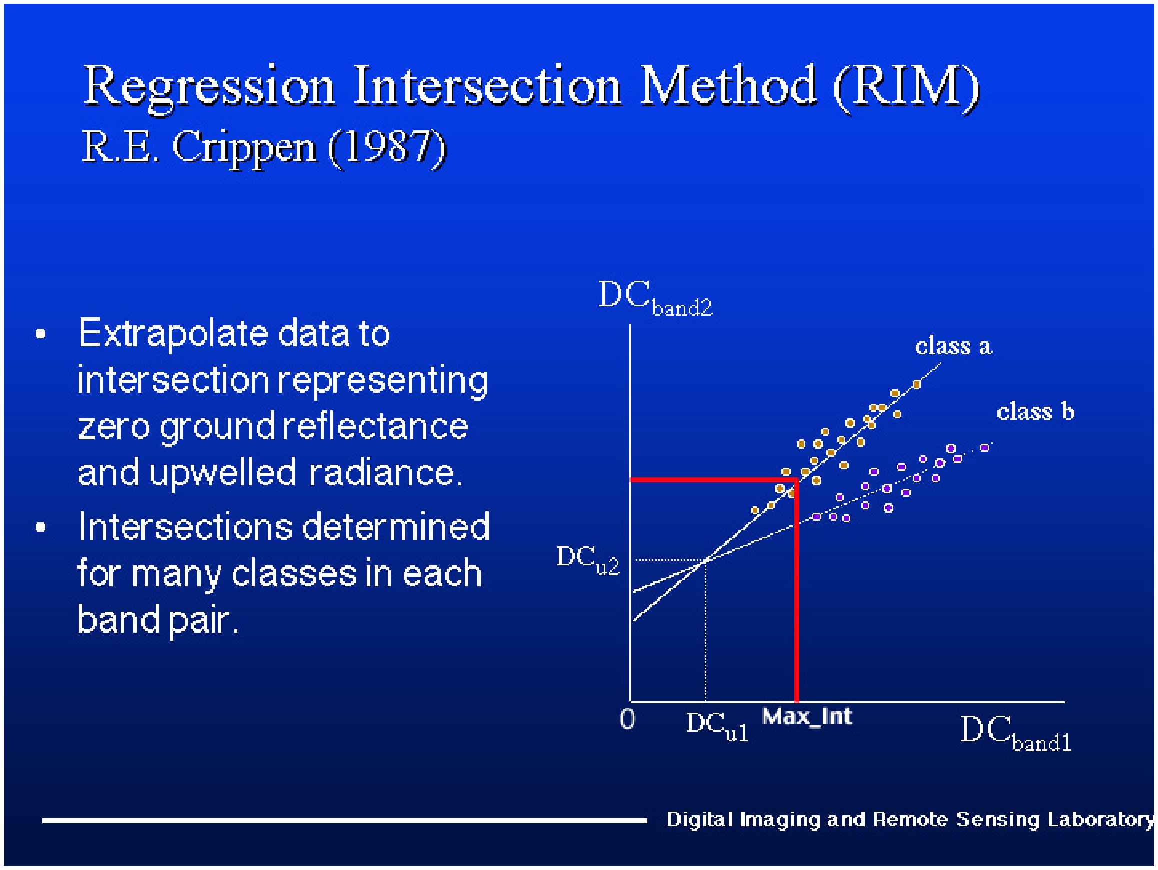

Regression Intersection Method (RIM)

R.E. Crippen (1987)

- Extrapolate data to intersection representing zero ground reflectance and upwelled radiance.
- Intersections determined for many classes in each band pair.

Digital Imaging and Remote Sensing Laboratory

Figure 3.3-1 Example of In-Class Distributions in Two Bands (Barnes, 1997)

The maximum hard limit for acceptable class regression line intersections is set by the "toe" of the image histogram in the dark pixel region (for example, see Max_Int in Figure 3.3-1). This requirement was put in place so that the resulting RIM-derived total upwelling radiance could not be a value greater than the dark pixel radiances in the image. The absolute histogram minimum could very well be either a dead or noise contaminated pixel. In the case of this algorithm, the minimum number of pixels in the dark bin was set to ten. The minimum intersection cutoff value is set to a DC of zero so that the RIM-derived upwelling radiance cannot be negative. Intersections above and below the hard limits are discarded from consideration. An example of the acceptable range limits for the intersection coordinates is given by the red lines in Figure 3.3-1.

Once a cluster of acceptable intersections are found for the band pair, the mean (or median) value is determined and the transformed DC becomes the total upwelling radiance value for the first band of the comparison. This process is then repeated for the second and subsequent bands. See Figure 3.3-2 for a general flow chart of the algorithm.

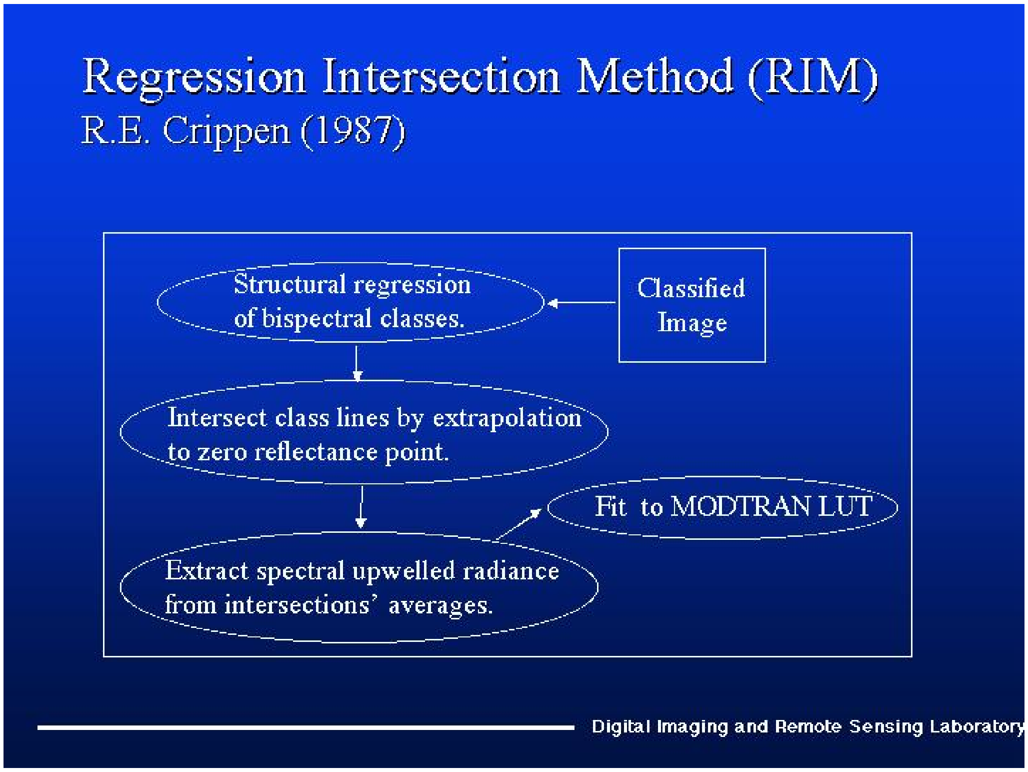

Regression Intersection Method (RIM)

R.E. Crippen (1987)

Structural regression of bispectral classes.

Classified Image

Intersect class lines by extrapolation to zero reflectance point.

Fit to MODTRAN LUT

Extract spectral upwelled radiance from intersections' averages.

Digital Imaging and Remote Sensing Laboratory

Figure 3.3-2 RIMAC Flow Chart

The total upwelling radiance in this case is defined as:

$$L_{Total\_Upwelled} = L_{env} \rho_{avg} + L_{atmos\_upwelled} \tag{3-1}$$

where L_{env} is the radiance contribution of the target surround, ρ_{avg} is the average reflectance of the surround, and $L_{atmos\_upwelled}$ is the atmospheric radiance component. Light is highly scattered by the atmosphere in the blue region of the spectrum from ~390nm to 500nm. Unfortunately, this increased scatter also reduces the apparent contrast within a defined class in the scene. As stated previously, the integrity of the RIM is highly dependent on class contrast. This is easily understood by referring to Figure 3.3-1. As the contrast within a class in the two bands of interest decreases, the distribution becomes increasingly circular. The correlation of the class distribution decreases and the validity of performing a regression analysis becomes questionable. Furthermore, even if a regression analysis can somehow be justified, the regression lines for the classes have a high probability of either diverging, being parallel, or converging outside of the hard limits. To avoid the low contrast spectral region, but still include bands where the aerosol signature is apparent, the spectral range used for RIMAC has been set at 550nm-700nm. It should be noted that these spectral limits have been derived from analyses on a very small image set. Below about 500nm, the total upwelled radiance from the RIM method appears to be underestimated with the error increasing into the blue region of the spectrum. Further work is needed in this area to determine if the 550-700nm spectral range is the "best" for the total upwelled radiance estimation.

The total upwelling radiance as defined by Equation 3-1 has no target interaction at all; it is a function only of the scattering of the atmosphere defined by the aerosol phase function and some interaction from the target surround. Using the radiometry from a MODTRAN 4.0 generated LUT, a nonlinear fit can be performed to find the least-squared spectral error between the RIM-derived total upwelled radiance and a MODTRAN calculated atmosphere for a specified visibility. However, the average reflectance of the target surround has must somehow be estimated.

Before the NLLSSF can be performed to solve for the aerosol-specific visibility parameter, one of two methods can be used to estimate ρ_{avg}. If the hyperspectral image spectral range includes a 2200nm band, then a ratio method developed by Kaufman (1997) can be used to estimate ρ_{avg} for the image. The average image spectra is calculated and since the multiple scattering terms in the 2200nm band in the radiative transfer equation are negligible, a simplified lower-dimensionality inversion to reflectance is performed:

$$\rho = \frac{\left(L_{sensor} - L_{atmos\_upwelled}\right)}{\frac{E_s \cos(\sigma)\tau_1\tau_2}{\pi}} \tag{3-2}$$

where $L_{atmos\_upwelled}$ is the non-target/surround interactive upwelling radiance component scattered from the atmosphere, E_S is the exo-atmospheric irradiance from the sun, σ is the solar zenith angle, τ_1 is the sun-target transmission term, and τ_2 is the target-sensor transmission term.

Kaufman's correlation predicts that the reflectance in the 660nm band is approximately half that of the 2200nm band (Kaufman, 1997). Once the reflectance for the 2200nm band is estimated, the 660nm reflectance can be estimated by multiplying the 2200nm band reflectance by

0.5. Since this estimate is for image-wide spectra, it is assumed that the reflectance from 550nm-700nm is constant and equal to the 660nm Kaufman estimate.

A least-squares spectral fit is performed by varying only the aerosol visibility to match the RIM-derived total radiance value via Equation 3-1. If the spectral response of the sensor does not include a 2200nm band, a simple NLLSSF on the RIM-derived total upwelled radiance is performed on the 550-700nm bands where the average target surround is assumed to be a linear function of wavelength in this region. There are three parameters to vary with this latter option, as opposed to one in Kaufman's, method: the aerosol-specific visibility, the reflectance bias, and the reflectance gain terms.

The aerosol-specific visibility that corresponds to the MODTRAN-derived total upwelled radiance with the least-squares spectral fit to the RIM-derived total upwelled radiance is then assigned to the image. Since there is only one visibility value that is derived from the RIMAC, it is assumed that the user is aware that this amount is an average visibility over the entire image area. Another words, the visibility is assumed to fairly homogeneous over the image area. For real imagery this is certainly not true, but if the aerosol loading varies only slightly over the scene, then the errors generated by using the scene average visibility will be small. This is not a visibility on a per-pixel basis as in the NLLSSF technique; when this module is complete, it assigns the same visibility to all pixels in the image.

3.4 Column Water Vapor

The user would select either NLLSSF, APDA, or a default columnar water vapor value for the image, as seen at the bottom of Figure 3.1-1. If Green’s NLLSSF method is chosen, Equation (3-1) would be used with $\rho avg=\rho$ for the first pass of the algorithm and then Equation (3-1) for the second pass. The pre-conditioning step for the amoeba routine is the same as the previous steps for the reflectance gain and bias, but the liquid water vapor scalar is determined by using CIBR in the 975nm absorption band.

It should be noted that adding the downwelled terms to the APDA ratio equation was deemed unnecessary and would add substantially to computer runtimes. This is because of multiple recursion with MODTRAN runs at three or more wavelengths.

3.5 The Atmospheric Point Spread Function (PSF)

As previously mentioned, the earth's atmosphere is a far from perfect transmitter of electromagnetic energy. This is true not only because of absorption that varies by wavelength, but also because of Rayleigh scatter due to well-mixed gases and Mie scatter from much larger suspended dust and organic debris. As reviewed in Section 2.5, some fraction of the total number of photons that arrive at the sensor have had no interaction with the target in the sensor IFOV (instantaneous field of view). The atmospheric upwelling radiance (Figure 2.5-2) has no interaction with the ground so its contribution can be estimated with Rayleigh and Mie scattering models. However, the other atmospheric pathway referred to as the "environmental" or "adjacency" radiance, does interact with the ground. In this case, the direct and diffuse components of solar radiation reflect from the surround of a target that in turn are scattered by the atmosphere into the IFOV of the sensor (Figure 2.5-5).

To characterize the adjacency radiance contribution, it is first necessary to estimate the aerosol visibility so that the aerosol-induced scattering can be calculated for the numerous atmospheric layers between the target and sensor. The aerosol phase function $P(\theta,\lambda)$ can then be calculated for each layer 'h' of the atmosphere. $P(\theta,\lambda)$ defines the angular distribution of light that scatters into the direction θ per steradian in a homogeneous scattering medium. The phase function also is the energy distribution that governs the fractional scattering contribution of the reflected radiance from a given surround pixel that scatters into the nadir-viewing sensor path (Figure 3.5-1).

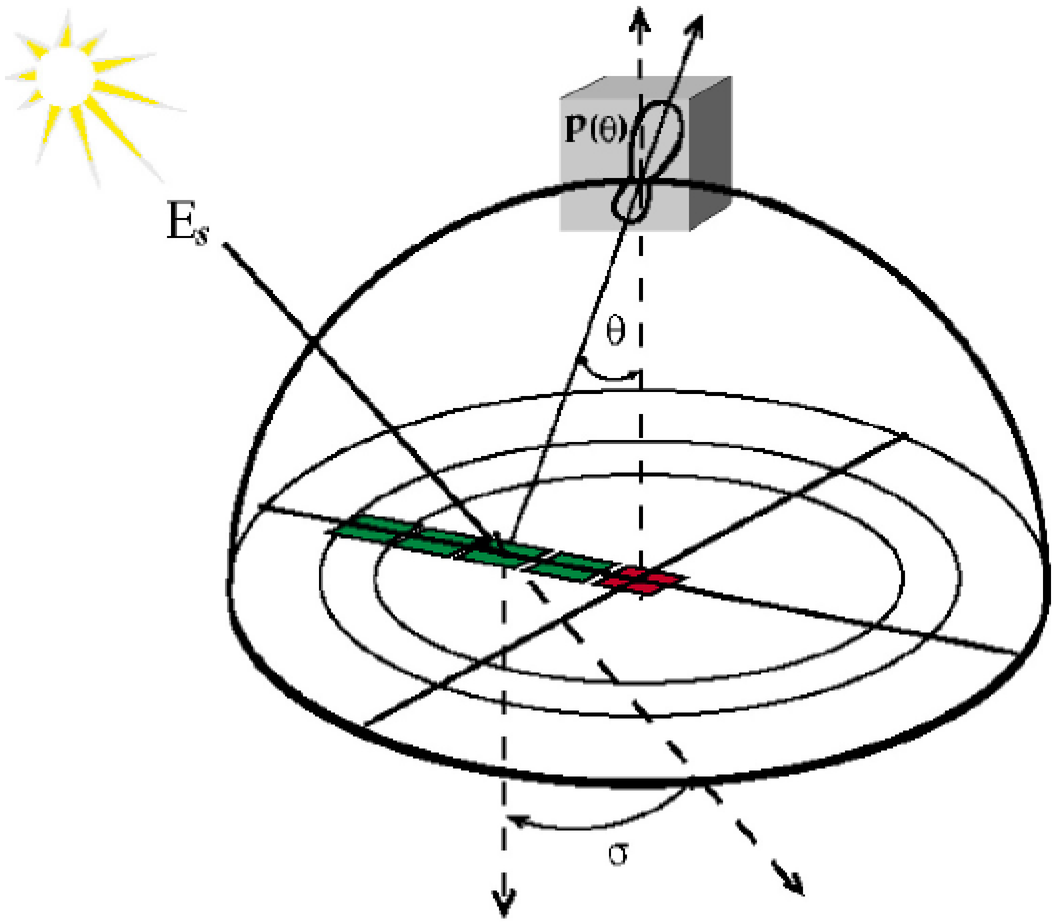

Figure 3.5-1. Atmospheric path for light scattered into the sensor path from a surround ground-projected pixel (green) and contributes to the irradiance leaving the target ground-projected pixel (red).

In theory, the atmospheric PSF has infinite support. However, the contribution of surround radiance from a given ground-projected pixel is known to drop off substantially with increasing angle to nadir because of increasing atmospheric transmission and the forward-scattering nature of the aerosol phase function. To describe this entire radiative transfer process mathematically, the total environmental contribution can be written:

$$L_{env\_total}(\lambda) = \int_{\tau_{layer}(1)}^{\tau_{layer}(h)} \int_{\phi=0}^{2\pi} \int_{\theta=0}^{\frac{\pi}{2}} L(\theta,\phi,\lambda)\, P(\theta,\lambda,\ H)\, T_2(\theta,\lambda)\, \rho(\theta,\phi,\lambda\ )\, d\tau \sin(\ \theta\ )\, d\theta\, d\phi \qquad (3\text{-}3)$$

where θ is the angle of the surround location from nadir, φ is the azimuthal angle of the surround location , $L(\theta,\varphi,\lambda)$ is the solar ground radiance which is incident on a surround pixel of reflectance $\rho(\theta,\varphi,\lambda)$, $P(\theta,\lambda,H)$ is the aerosol layer phase function (dependent on both aerosol composition and relative humidity H), $T_2(\theta,\lambda)$ is the transmission of surround pixel radiance to the sensor, $d\tau$ is the atmospheric layer optical depth, and $\sin(\theta)d\theta d\varphi$ is the solid angle that the unit cross-section of the sensor IFOV presents to the surround pixel (Otterman and Fraser, 1979).

The geometry can be observed by referring to Figure 3.5-2. Further computations on the solid angle determination can be seen in Appendix A. However, MODTRAN 4.0 already calculates the resolved environmental radiance (in this case using a 1.0 albedo ground target) which is included in the LUT. The interest for this algorithm section is to calculate the PSF or the ground reflectance weighting function for this MODTRAN-derived radiance value.

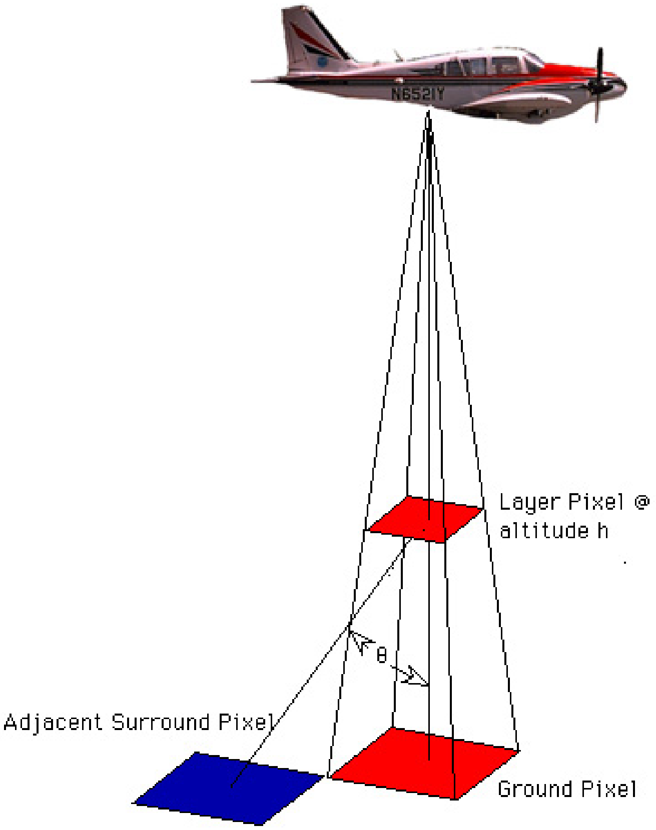

Figure 3.5-2. The geometry for the solid angle of what the source (the surround pixel) sees of the unit cross-section of the IFOV.

With the finite supports of the PSF defined as a grid of $i \times j$ ground-projected pixels, it can easily be shown that the unnormalized grid values are defined as:

$$\mathrm{PSF}_{\mathrm{unnorm}}(i,j) = \sum_{\mathrm{layers}} P(\theta,\lambda)\ \Omega(i,j)\ e^{-(\tau_{2a}\sec\theta+\tau_{2b})}\Delta\tau_{\mathrm{layer}} \tag{3-4}$$

where θ is the angle made by the center of the pixel [i,j] of the surround with the nadir-view of the center (target) pixel as seen from the layer height, $P(\theta,\lambda)$ is the aerosol phase function for the layer, Ω is the solid angle subtended by the unit cross-section as seen by the i, jth surround pixel, τ_{2a} is the surround pixel-to-unit layer cross-section optical depth, τ_{2b} is the unit layer cross-section-to sensor optical depth, and $\Delta\tau_{\mathrm{layer}}$ is the aerosol layer optical depth. To calculate the fractional contribution of each surround pixel to the scattered radiance, it is necessary to normalize the PSF (*i.e* the PSF must integrate to unity). However, when this normalization is performed, the approximately equal aerosol layer optical depths cancel, leaving:

$$\mathrm{PSF}(i,\ j) = \frac{\sum\limits_{\mathrm{layers}} P(\theta,\lambda)\ \ \Omega(i,\ j)\ e^{-(\tau_{2a}\sec\theta+\tau_{2b})}}{\sum\limits_{i}\sum\limits_{j}\ \sum\limits_{\mathrm{layers}} P(\theta,\lambda)\ \ \Omega(i,\ j)\ e^{-(\tau_{2a}\sec\theta+\tau_{2b})}} \tag{3-5}$$

Since the goal is a convolution kernel used to weight the first-pass recovered ground reflectance values, the logic for this computation is easily followed. The magnitude of the resolved environmental radiance vector generated by MODTRAN 4 in the LUT inherently contains the optical depths that were cancelled out of Equation (3-5). Thus, in the context of the image, this normalized PSF weighting function can be thought of as a band-dependent convolution kernel. To computationally derive θ inside MODTRAN, the additional parameter of IFOV in milliradians must be added to a special tape5 in order to calculate the solid angle, the layer heights and the pixel center distances from nadir. Again, the index of refraction differences in the atmospheric layers is assumed to have a negligible effect on the ground spot variation or shape of the atmospheric PSF.

At this point it should be mentioned that no skew correction is performed on the PSF to account for the surround effects of target pixels that are not directly beneath the sensor. Reinersman and Carder (1995) did Monte Carlo simulations with AVIRIS imagery that show the skewness of the PSF is very small at least up to 15 degree off-nadir (which is the half-extent of the AVIRIS field of view). Also, the PSF only accounts for Mie scattering and does not include Rayleigh scattering or Rayleigh-aerosol scattering interaction. Again, Reinersman and Carder (1995) work estimated that scattering effects other than Mie accounted for only a maximum of 5% of the of the PSF in the blue region where scattering due to aerosols is greatest. Thus, a more complex PSF generating process would buy only a small amount of scattering contribution that most likely is at or below the noise level of the entire radiative transfer system.

The surface plots of the spectral kernels give a conceptual view of the scattering contribution from each pixel. Figure 3.5-3 shows 11×11 kernels with AVIRIS-sized ground pixels and the fractional scattering contributions at the sensor in the 405nm band and the 2100nm band.

As would be expected, there is much less scattering in the short-wave infrared than there is in the blue region of the spectrum where scattering from atmospheric aerosols dominates.

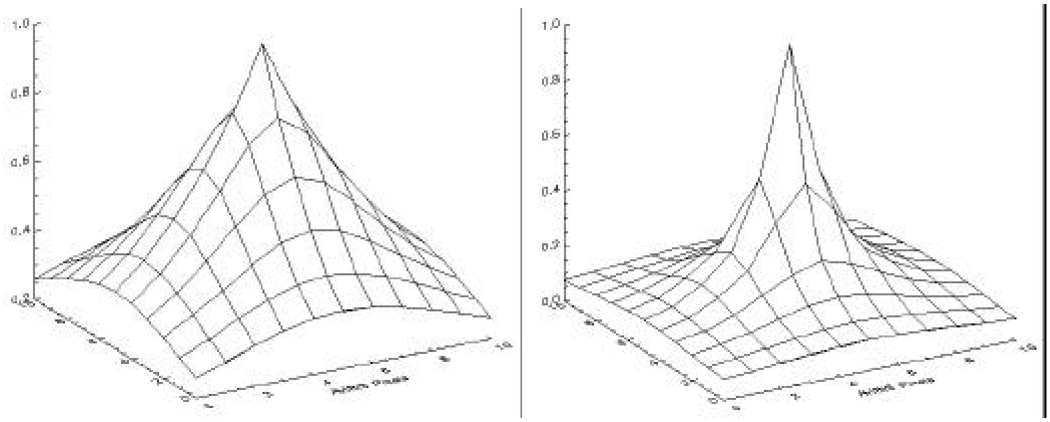

Figure 3.5-3. Fractional scattering contribution kernel in the 402nm AVIRIS band (left) and the 2100nm band (right) for a rural aerosol.

The surface plots in Figure 3.5-3 also match the predicted shapes of spectral atmospheric PSFs from the work of Reinersman and Carder (1995).

This is also the case in Figure 3.5-4 that shows the atmospheric PSF for the HYDICE Run 29 scene at 400nm (Band 2) and 2100nm (Band 166). Notice that because HYDICE was flown at a much lower altitude than AVIRIS, the fractional contributions from the surround pixels when the respective spectral bands are compared are less than what is seen in Figure 3.5-3. This would be expected since there would be less atmosphere between the ground and sensor and consequently less scattering as well. The PSF also is different because the IFOV for HYDICE is 0.5 milliradians, while the AVIRIS IFOV is 1.0 milliradians.

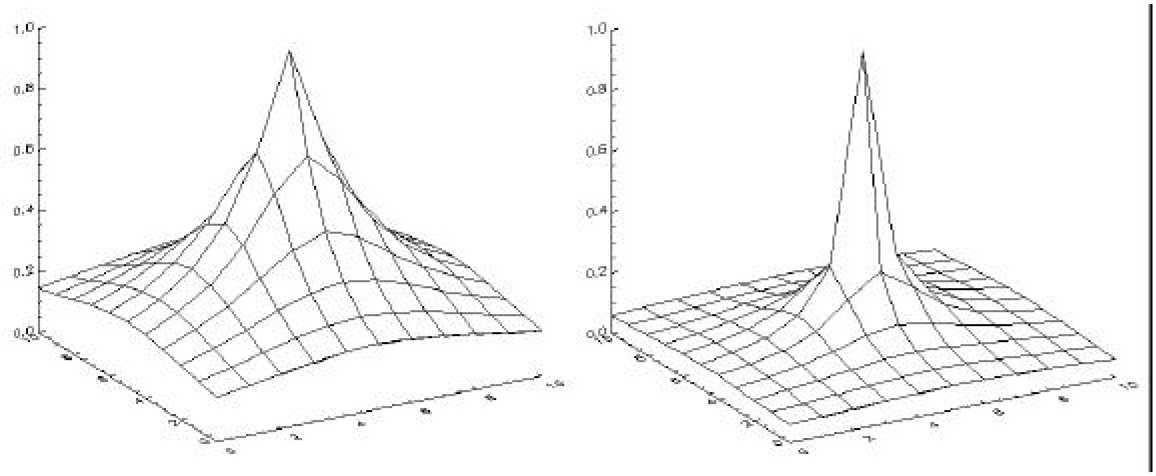

Figure 3.5-4. Fractional scattering contribution kernel (PSF) in the 400nm HYDICE band (left) and the 2100nm band (right) for a rural aerosol.

For comparison, the PSF from the desert aerosol in the cr08m33 Western Rainbow scene is also presented in Figure 3.5-5. The shape of the PSF is quite different due to the fact that the scattering phase function must be very isotropic. This parabolic shape is also very similar to Henyey-Greenstein phase function used for multiple scattering.

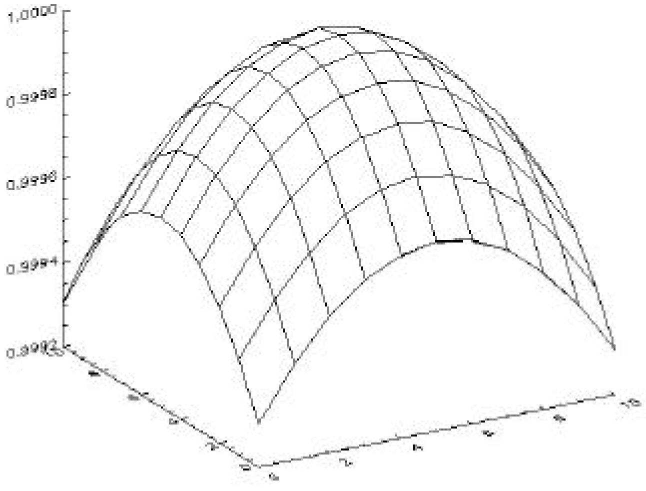

Figure 3.5-5. Fractional scattering contribution kernel (PSF) for a desert aerosol in all bands.

In the final calculation of the total environmental/adjacency effect radiance at the sensor, the magnitude of the resolved radiance also is very important. The resolved environmental/adjacency radiance vector is the environmental radiance at the sensor if the ground reflectance were 100%. In Figure 3.5-6, this is much less at 2100nm than at 402nm. This is intuitive because the Mie scattering due to aerosols declines steadily from the blue into the infrared and near-infrared region. Figures 3.5-4 and 3.5-5 also illustrate how the environmental radiance can act like a gain factor for the for the PSF since it is driven by the scattering optical depth. Even though the scattering optical depths were canceled out in Equation 3-5, they are still accounted for in the MODTRAN-derived resolved environmental radiance vector. Generally the longer the wavelength, the lower the scattering optical depth and thus the lower the total scattered radiance. This is statement is considered to be true only in the bands of the solar continuum and is invalid when volcanic dust, clouds, or other large particles are present in the optical path.

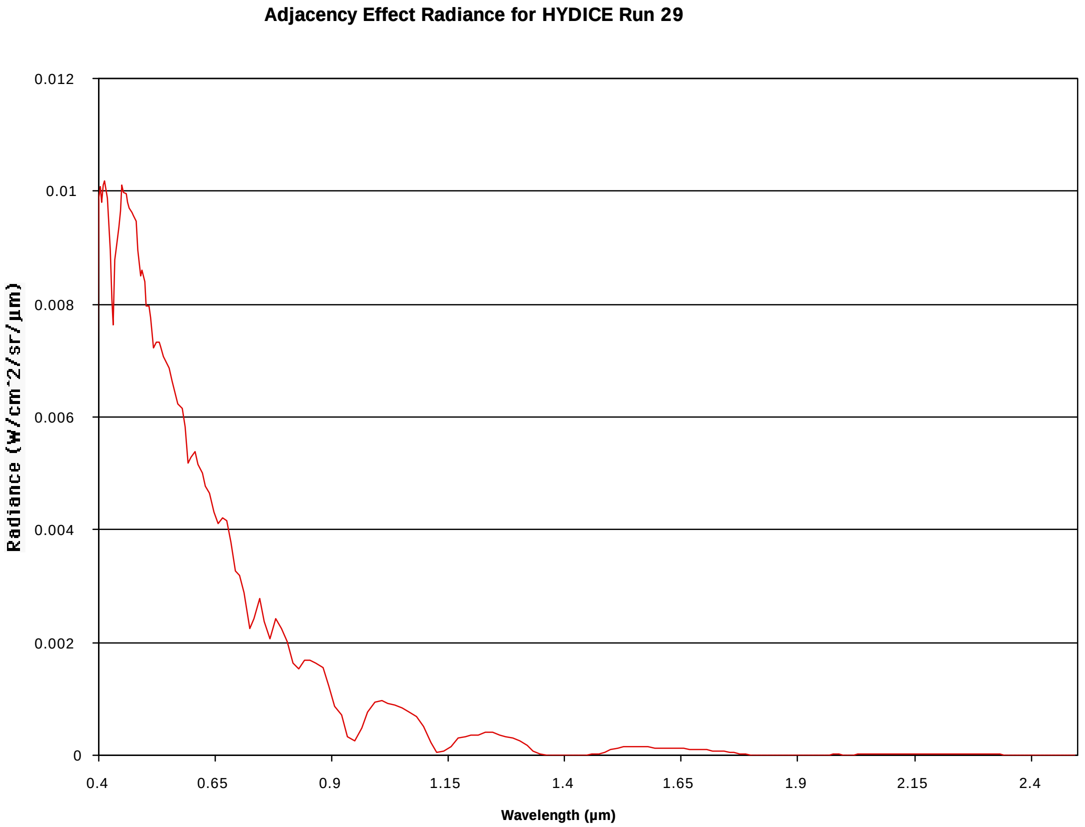

Figure 3.5-6. The resolved environmental/adjacency radiance vector from HYDICE Run 29.

A large part of this work was then extraction of the shape of the atmospheric PSF from MODTRAN, but just as important is the magnitude of the resolved environmental radiance vector.

In fact, the magnitude of the radiance gives the relative importance of the PSF; if the magnitude if is very small, the shape of the PSF doesn't really have a large effect in the overall radiative transfer equation. On the other hand, if the magnitude is large (see Figure 3.5-6 in the blue region), the shape of the atmospheric PSF will greatly affect the recovered ground reflectance. Figure 3.5-7 shows a plot of the different radiance components from the HYDICE run 29 scene and by just visually comparing the environmental radiance (L_{env}) to the other components, it can be ascertained how influential in the overall radiative transfer that it will be.

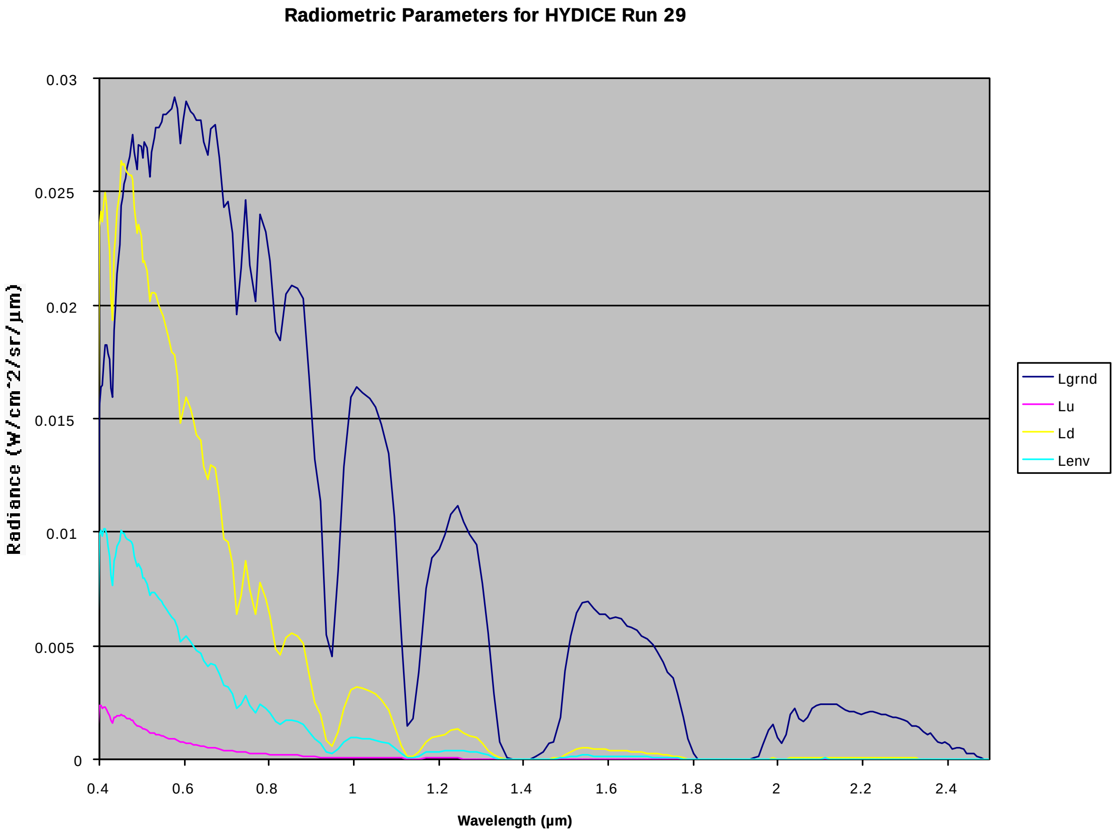

Figure 3.5-7. The different radiance components from the HYDICE Run 29 scene (the radiance components shown do not include interaction with the ground target).

Once the spectral "kernels" have been calculated, the kernels or PSFs are convolved with the first-pass reflectance image to yield the estimate for the average reflectance of the surround for each pixel in each band. A second pass can then be done through the inversion algorithm using Equation 2-39.

4. Results and Discussion of Inversion from Sensor Radiance to Ground Reflectance Units

The total inversion of sensor radiance to estimated ground reflectance was performed on eight hyperspectral images from four different geographical locations and environmental conditions. For each image, a number of different atmospheric parameter estimation options were used and the results were compared to the ground truth target spectral reflectance. All spectral reflectance errors were plotted from 400nm-1800nm with the exception of the AVIRIS Boreas image because the truth data only extended from 400nm-900nm. The SWIR spectral range was omitted for the HYDICE runs due to unresolved issues with the radiometric calibration in these bands. For all the following plots, the definition of spectral reflectance error is the recovered reflectance from the inversion minus the ground truth.

The spectral reflectance RMS error was calculated for all cases from 400nm- ~1350nm with bands omitted that had estimated optical depths greater than 0.4. Because the 940nm water vapor bands were used to estimate columnar water vapor, they were not omitted in the RMS computation.

4.1 HYDICE Run 29 ARMs Site Image

The atmospheric characterization and reflectance inversion tools were applied to a June 24, 1997 HYDICE data collection over the DOE ARM site in Oklahoma. Because of this location, the MODTRAN aerosol selected for the LUT used by the inversion algorithm was the rural model. For this collection, several well-characterized gray reflective panels were deployed for ground truth as shown in Figure 4.1-1.

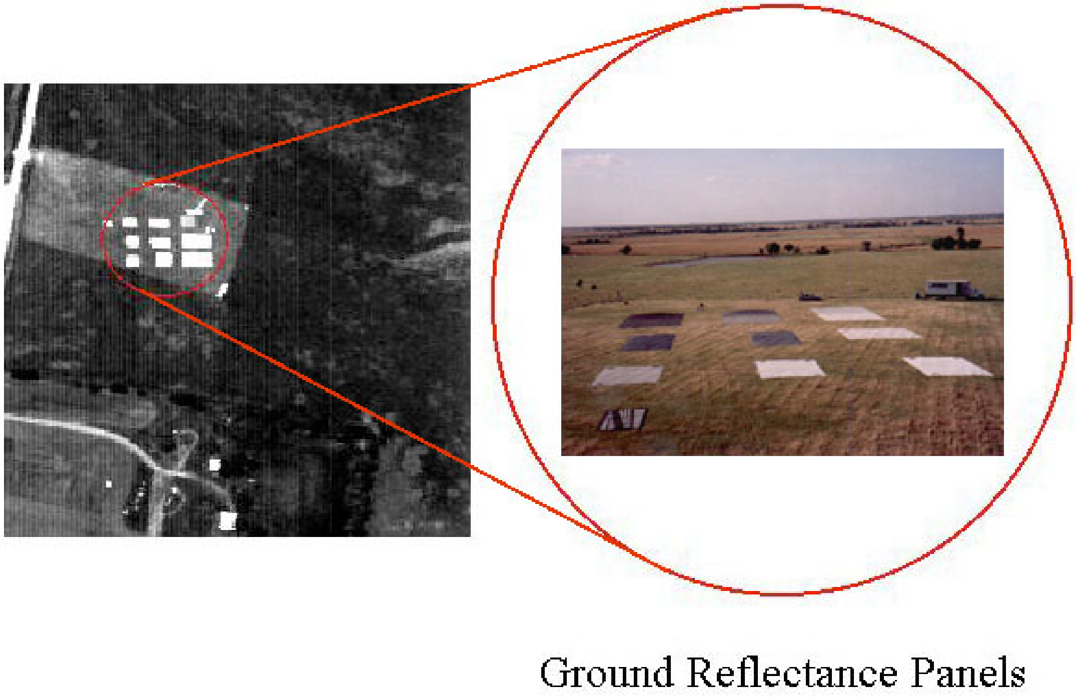

Figure 4.1-1. HYDICE ARM site gray panels (photo on right courtesy of MTL).

These panels had nominal reflectance, of 2, 4, 8, 16, 32, and 64%. For evaluation purposes, the difference in reflectance in each band was computed for each panel. The image selected from this collect was HYDICE Run29 since it is an image that has proved radiometrically reliable in previous research work and has only a few clouds in the sky at horizon level (as seen from ground truth photos). The following are the results of the inversions from sensor radiance to ground reflectance for HYDICE Run 29.

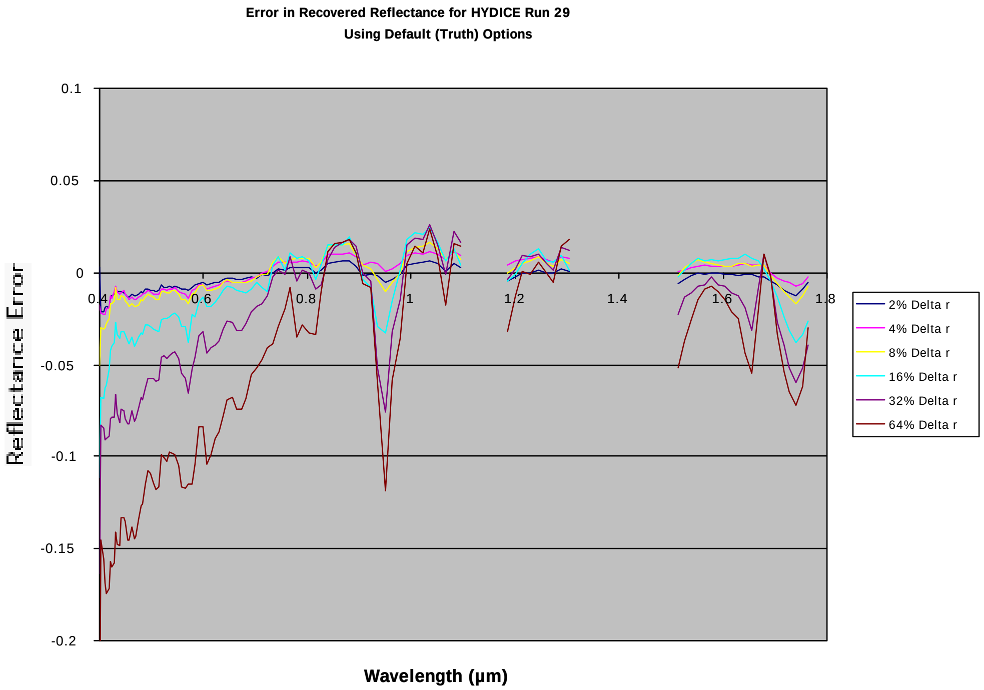

Figure 4.1-2. Plot of reflectance error for the inversion to reflectance using the truth (default) data from the time of acquisition .

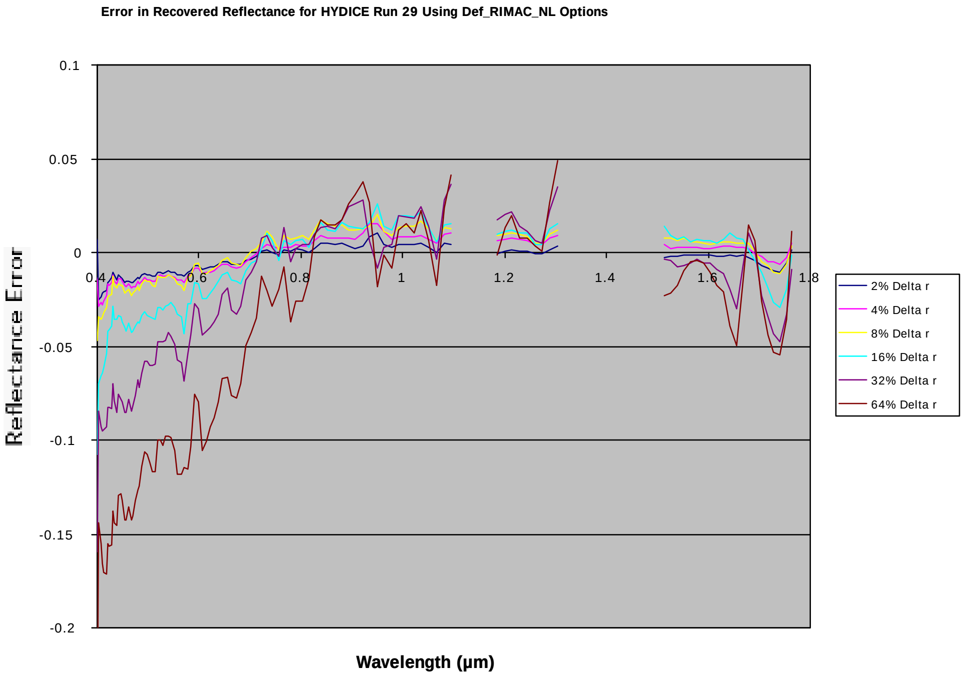

Figure 4.1-3. Plot of reflectance error for the inversion to reflectance using the truth (default) surface elevation, RIMAC for the aerosol visibility, and NLLSSF for the columnar water vapor.

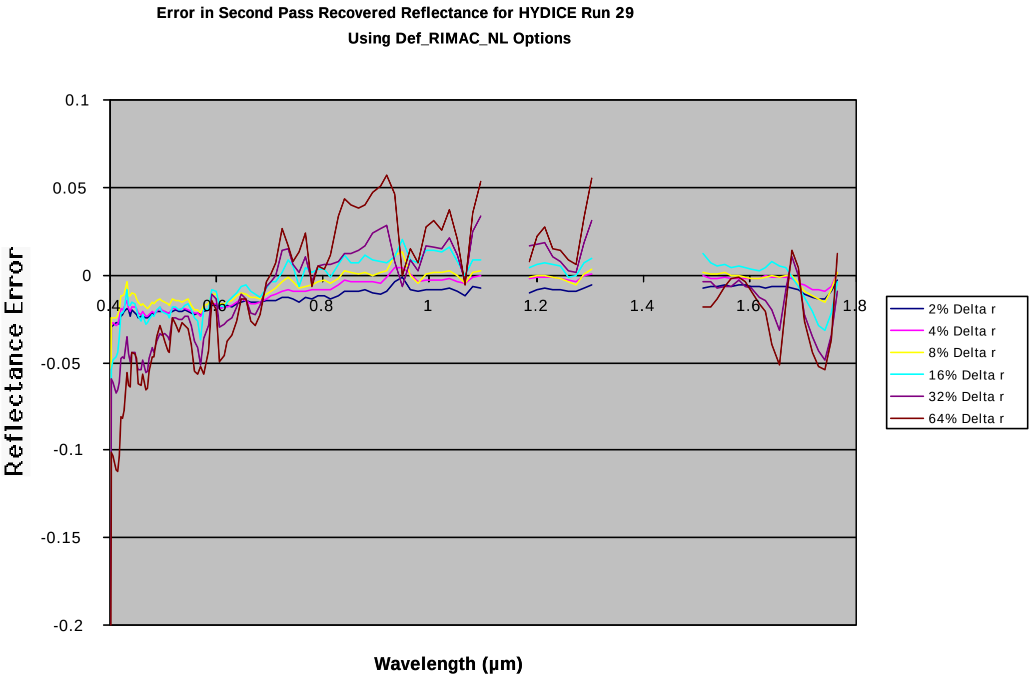

Figure 4.1-4. Same options as 4.1-3 after second pass.

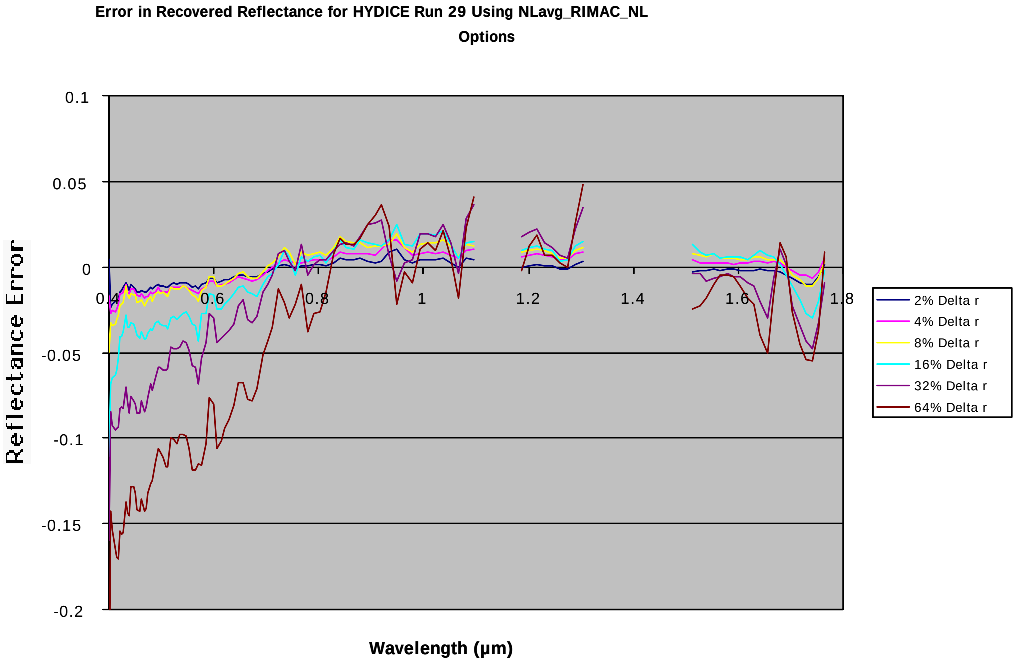

Figure 4.1-5. Plot of reflectance error for inversion to reflectance using the image-wide average NLLSSF for surface elevation, RIMAC for the aerosol visibility, and NLLSSF for the columnar water vapor.

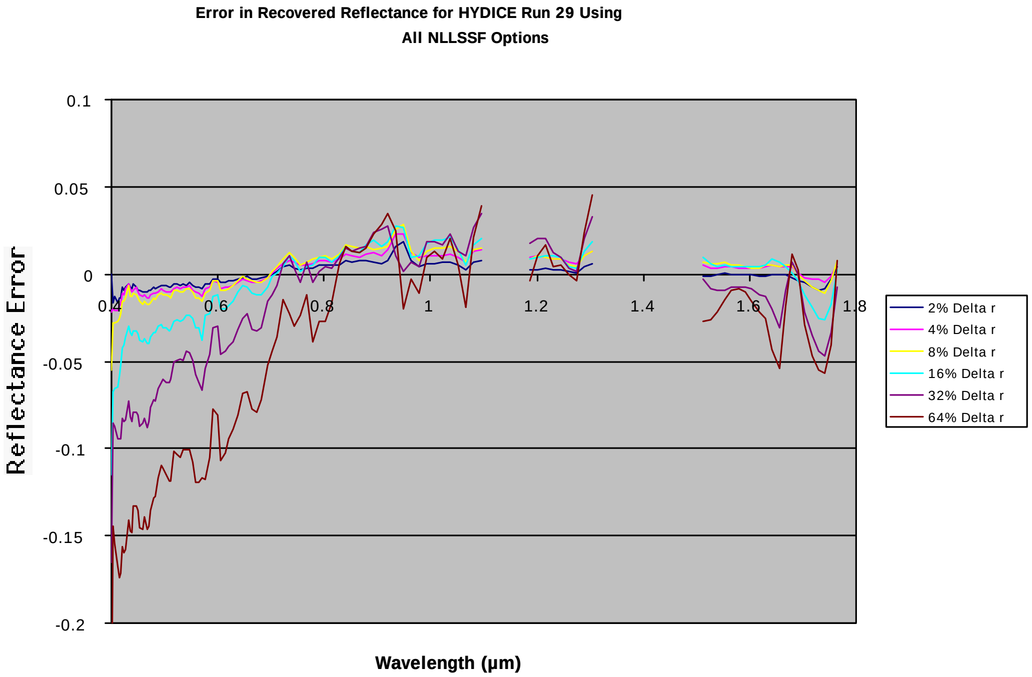

Figure 4.1-6. Run29 plot of reflectance error using NLLSSF for all options.

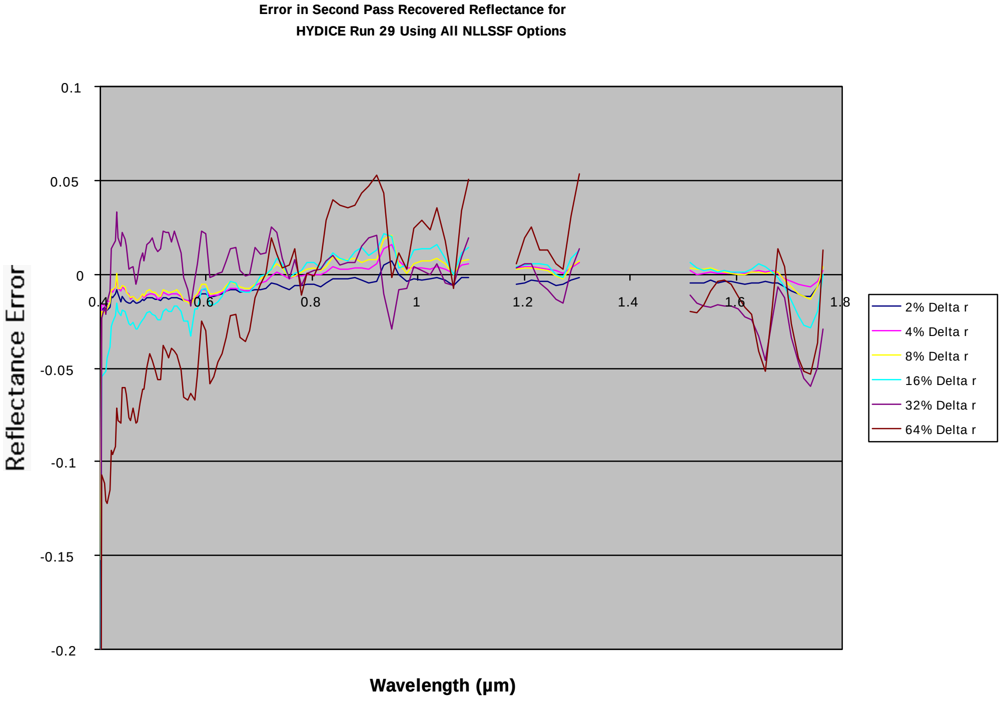

Figure 4.1-7. Run29 plot of reflectance error after second pass with NLLSSF for all options.

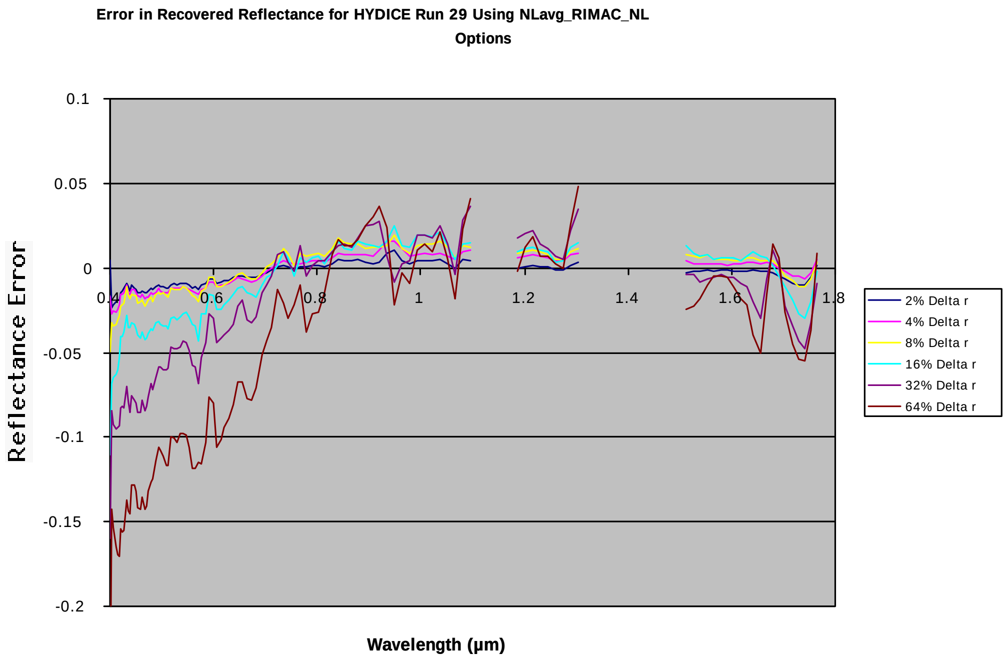

Figure 4.1-8. Run29 plot of reflectance error using image-wide average NLLSSF for elevation, RIMAC for visibility, and NLLSSF for columnar water vapor.

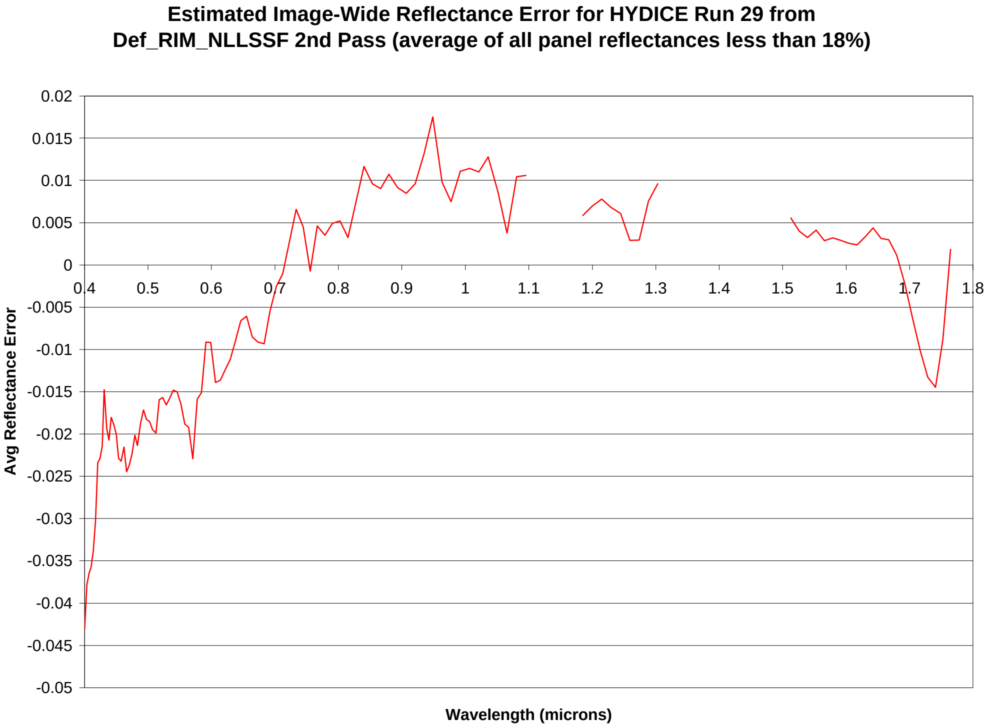

Figure 4.1-9. Estimated image-wide reflectance error for ground targets of 18% reflectance or less.

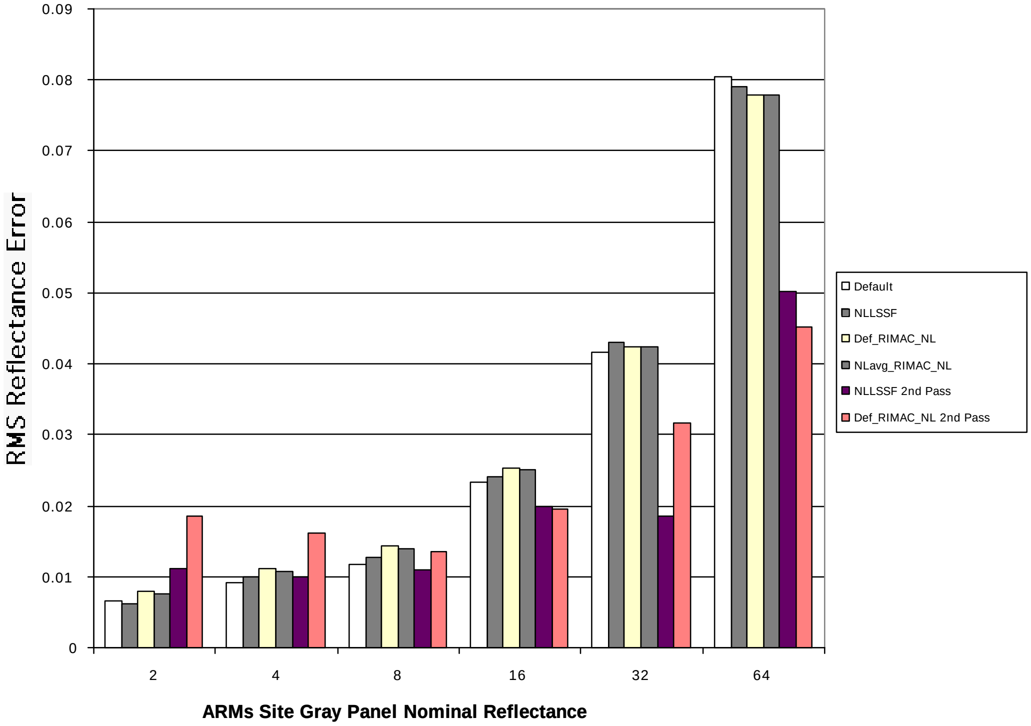

Figure 4.1-10. RMS reflectance error comparison for ARM site panels.

Elevation Aerosol Vis Water Vapor	Default	Default RIMAC NLLSSF	NLavg RIMAC NLLSSF	NLLSSF	Default RIMAC NLLSSF 2nd Pass	NLLSSF 2nd Pass
Surface Elevation (km)	0.315	0.315	0.414	0.417	0.315	1.133
Visibility (km)	58.00	34.56	33.32	47.73	34.62	48.0551
Water Vapor (g/cm^2)	5.146	6.75	6.874	6.803	7.45	6.939

Table 4.1-10. Estimated atmospheric parameters from using different options in the inversion from sensor radiance to ground reflectance algorithm. Note: The surface elevation is also coupled to the pressure profile in the radiosonde and the water vapor amount is the total sun-target-sensor column value.

For all combinations of options used in the inversion, the data show good patterns of agreement that deteriorate somewhat toward the blue region in the first-pass runs. The error in the blue end of the spectrum is largely due to error in the aerosol term. Note how the second pass through the algorithm, which accounts for aerosol scattering from the surround, dramatically improved the errors in this region, though some error persists. The fine spectral shape to the error is most likely to be due to differences between the instrument spectral calibration and the MODTRAN spectral radiometry models. There also is a bit more error in the second pass with the RIMAC option. It appears that some error may be due to assumptions about the aerosol scattering in RIMAC, but the difference in RMS error is only 0.005 reflectance units (which is the error tolerance for this algorithm).

This test case is presented first since the ARM site HYDICE collection represents the best available characterized data set. Extensive ground truth, radiosonde, and weather conditions were logged for this acquisition and the HYDICE sensor has been used for several years, thus improving the reliability of the data. This being the case, the real benchmark for recovering reflectances are the default or truth runs. Figure 4.1-9 has been presented to give a metric of how well the algorithm would perform given a scene with these atmospheric conditions. From Figure 4.1-10, it can clearly be seen that the great majority of the inversions with various options were equal to or better than using the truth data (within standard error). This result is very important since the inversion algorithm yielded equivalent or better recovered spectral reflectance curves of the ground targets as would be retrieved from an expensive and time-consuming extended field campaign.

It is also readily apparent that the RIMAC compares favorably with the NLLSSF method in the recovery of ground target reflectance. The aerosol-dependent visibility is somewhat different between the two (Table 4.1-1), but it must be remembered that the RIMAC visibility is an image-wide parameter and the NLLSSF value is the average of 6 pixels in the center of the gray panels. The results validate that the RIMAC is a useful tool in acquiring an estimate of aerosol-dependent visibility when no close estimate of this parameter is available and when fast computation times are important (NLLSSF has much longer run times).

This test also validates the use of an atmospheric PSF based on the MODTRAN-derived radiometry and the aerosol scattering phase function. The reflectance recovery error in the blue region was reduced significantly by using the second pass through the algorithm and utilizing the spatially varying reflectance contribution of the surround to the radiance at the sensor. As a side note, these trials included an inversion to reflectance which used a simple average over the extent (11×11 pixels). See Appendix C for a very interesting analysis with this single image sample.

4.2 AVIRIS Boreas Image

This image was acquired by AVIRIS on September 17, 1994 for studies of the boreal forest in Canada. The ground truth was taken from observation towers at four different sites in the spectral region from 400-900nm. The chart legends identify each of these ground truth sites by pixel position (column, row) in the original AVIRIS scene. Because of the clarity of the image, a test inversion was run in single scattering mode to compare with the multiple scattering runs. Only one set of options for inverting to reflectance from the single scattering is presented since all combinations of options yielded virtually identical results. A truth or default test was not performed with this image since the radiosonde data did not coincide with the acquisition and the truth aerosol-dependent visibility is unknown. It was assumed that the aerosol model was rural.

Error in Recovered Reflectance for Four Ground Truth Sites in AVIRIS Boreas Imagery (NL_RIMAC_NL Single Scattering Model)

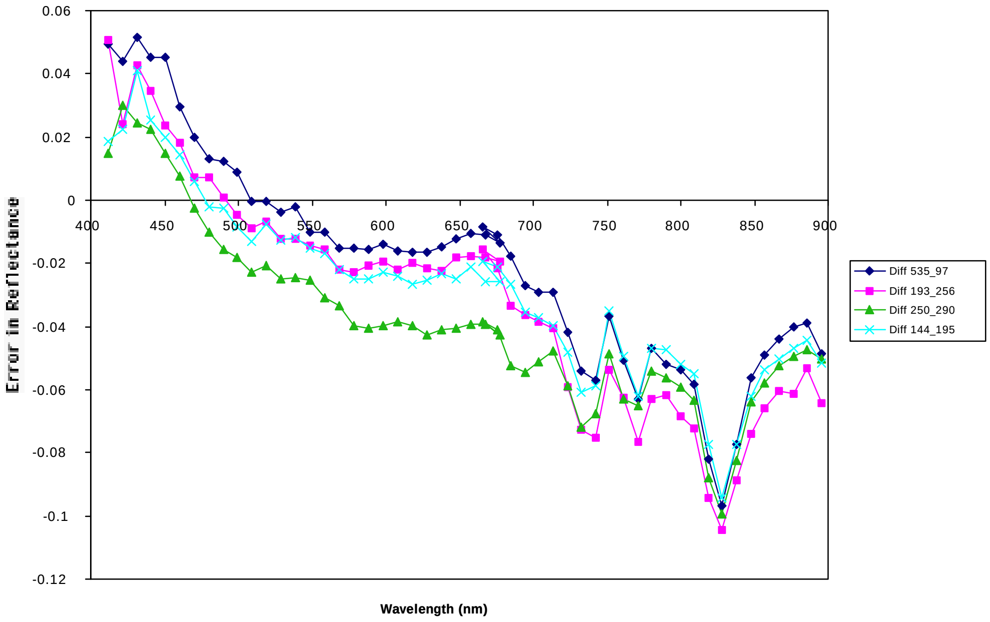

Figure 4.2-1. Boreas plot of reflectance error using the single scattering radiative transfer model from Equation (2-36).

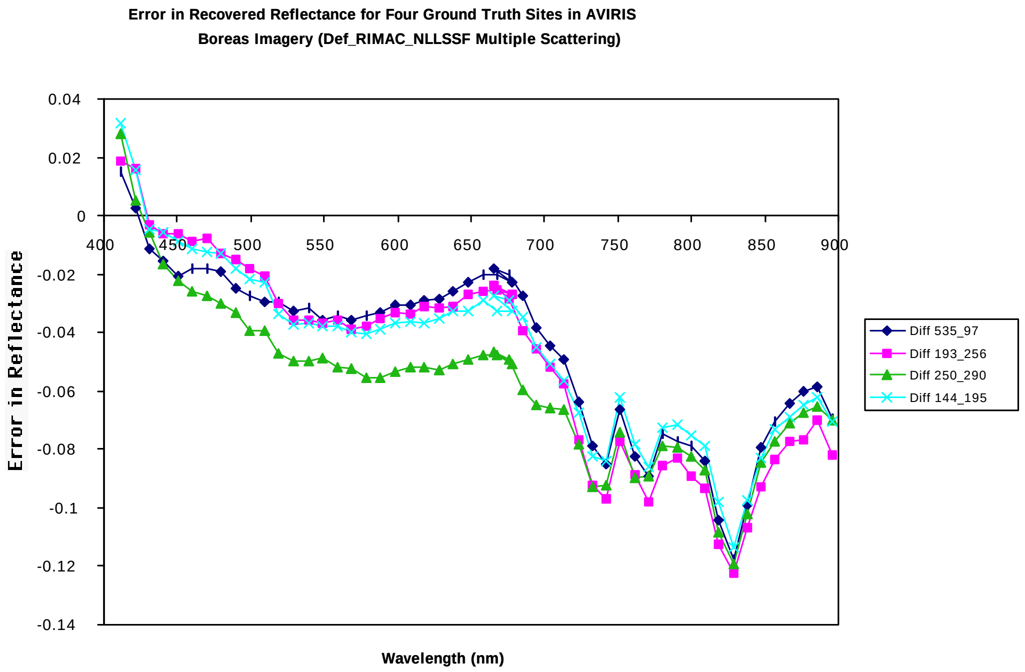

Figure 4.2-2. Boreas inversion error using truth (default) elevation, RIMAC for aerosols, and NLLSSF for columnar water vapor.

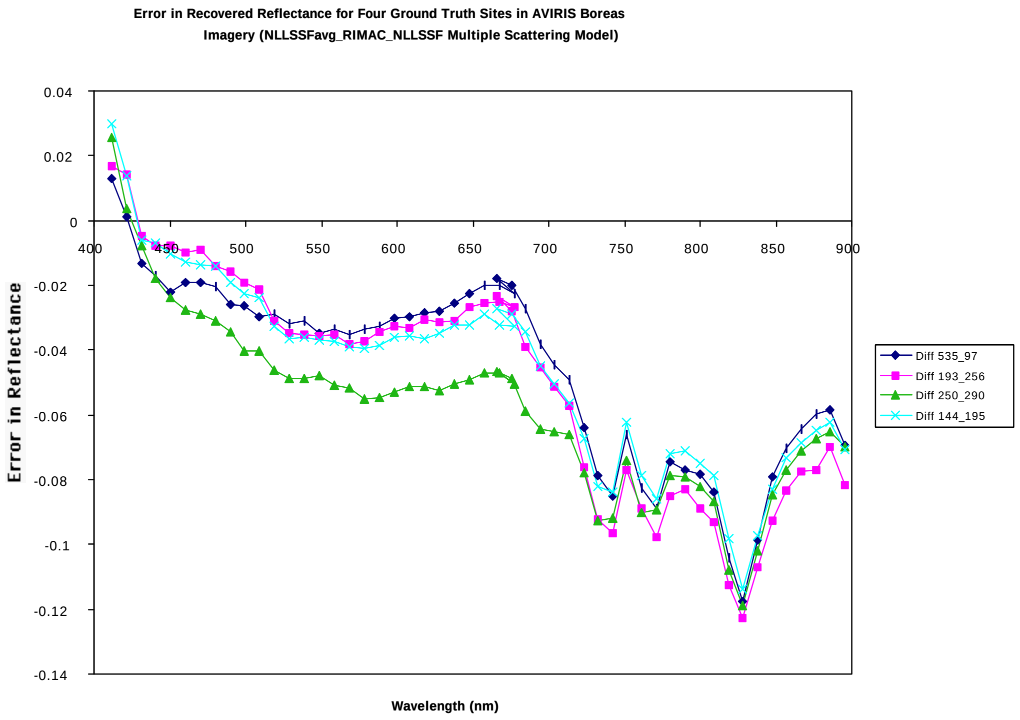

Figure 4.2-3. Boreas error using image-wide average NLLSSF elevation, RIMAC for aerosols, and NLLSSF for columnar water vapor.

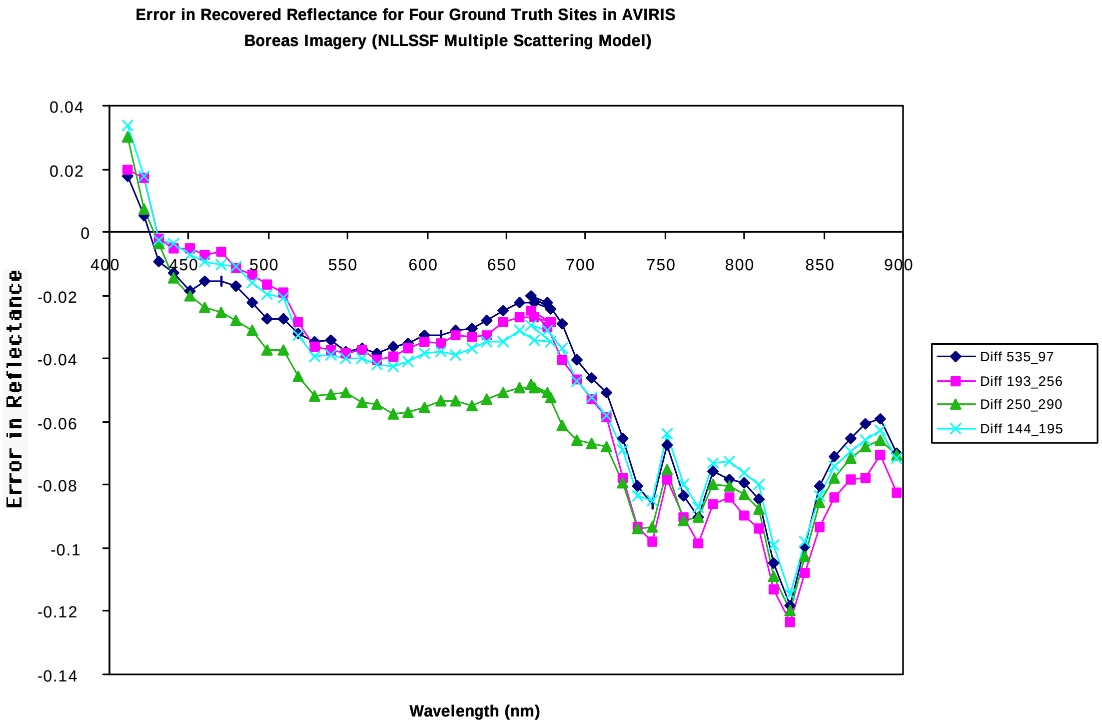

Figure 4.2-4. Boreas inversion error using NLLSSF for all options.

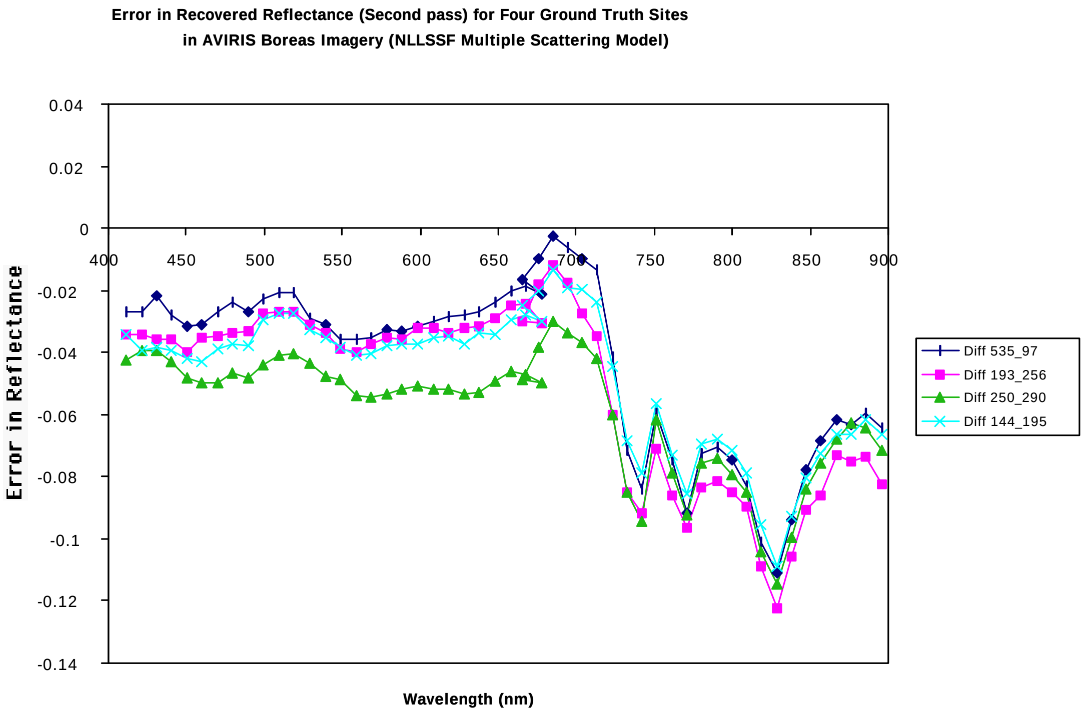

Figure 4.2-5. Boreas inversion error for second pass with all NLLSSF options.

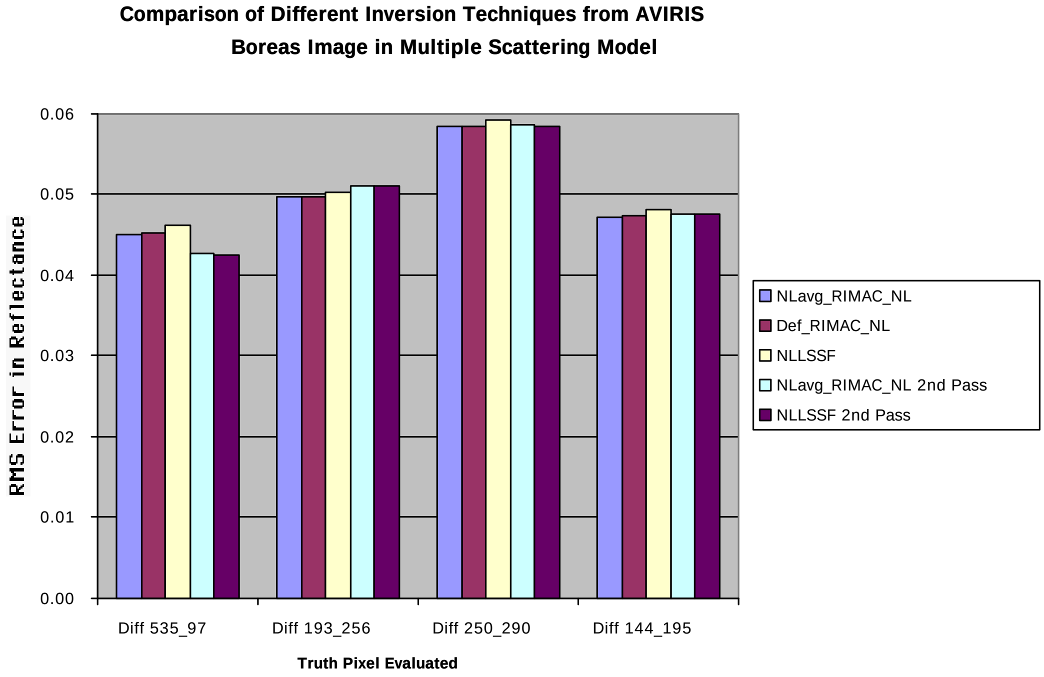

Figure 4.2-6. AVIRIS Boreas multiple scattering RMS recovered reflectance errors.

<u>Elevation</u> <u>Aerosol Vis</u> Water Vapor	Default RIMAC NLLSSF	NLavg RIMAC NLLSSF	NLLSSF	NLavg RIMAC NLLSSF 2nd Pass	NLLSSF 2nd Pass
Surface Elevation (km)	0.315	0.426	0.427	0.324	0.318
Visibility (km)	69.999	69.999	53.73	69.999	69.71
Water Vapor (g/cm^2)	3.313	3.281	3.26	3.26	3.24

Table 4.2-1. Estimated atmospheric parameters from using different options in the inversion from sensor radiance to ground reflectance algorithm. Note: The surface elevation is also coupled to the pressure profile in the radiosonde and the water vapor amount is the total sun-target-sensor column value.

It is clear from viewing the plots from Figures 4.2-1 to 4.2-5 that the spectral reflectance errors were nearly identical for all multiple scattering runs without regard to the choice of atmospheric parameter options. The RMS errors for the single scattering cases (not shown) is actually less than that of the multiple scattering model cases, but the spectral error is considerably flatter over all the wavelengths in the latter cases. The rounded aerosol shape in the blue region is not apparent when the multiple scattering radiative transfer model was used. Thus, the multiple scattering model must be the correct model, but there must be other causes that contribute to the reflectance recovery error.

The most likely explanation for both the magnitude of the reflectance recovery error and the "vegetation" shape of the spectral error is that the AVIRIS pixels include darker (less reflective) ground cover. The area covered by an AVIRIS pixel is a fairly large area of approximately 20 meters square. The total area covered by the spectral reflectance ground truth from the observation tower was much smaller. The inclusion of dark or shaded soil as well as shaded parts of the canopy would decrease the total integrated reflectance spectra of a 20-meter-square area; this is especially true in the more vegetative reflective region above 700nm. The reflectance error is the difference between the estimated reflectance and the truth reflectance. With the thin atmosphere evident in Table 4.2-1, it is obvious that not many more photons can be gained at the sensor (the solar source is largely transmitted). Spectra can only be corrected by mixing the pixel with appropriate fractions of ground dark cover.

This test case only supports the validity of the RIMAC in that it stays with the NLLSSF technique for estimating the aerosol-dependent visibility almost to the maximum at the visibility contained in the MODTRAN-generated LUT.

From the Boreas image, it can plainly be seen that the pixels surrounding the four target pixels are fairly homogeneous. In this case, it would be expected that the use of the PSF and the second pass through the algorithm would not improve recovery of the reflectance. This is observed in Figure 4.2-6 that neither of the two second-pass trials are measurably better than the first-pass results.

4.3 HYDICE Western Rainbow Image (Low Altitude)

The Western Rainbow HYDICE image set is a sample of the collection that took place on October 21, 1995. This first image set was acquired by the HYDICE sensor at an altitude of 1.52 km and is referred to as the low altitude set. Two groups of characterized reflectance panels of nominal reflectance 2%, 12%, 24%, 36%, 48%, and 60% were placed in the desert environment of the Yuma proving grounds in southern Arizona. The MODTRAN LUT used the desert aerosol model.

One group of reflectance panels is referred to as “Old” since these panels have faded due to exposure to the elements. However, they are still well characterized with field-truth reflectance measurements at the time of acquisition. The other group is referred to as “New” since these panels had no apparent fading and were most likely used for the first time in this collection. The images of the "Old" and "New" panels are actually subimages of a single HYDICE scene; if fact the panels were located are fairly close to one another. The reason why two subscenes were cut from the original large scene is that all of the full Western Rainbow HYDICE scenes were reclassified. Permission was granted for this research to use only these two subscenes; this is also the case for the high-altitude Western Rainbow scene cr15m50. The following plots are spectral reflectance errors using different combinations of inversion techniques.

4.3.1 Cr08m33 Old Panels

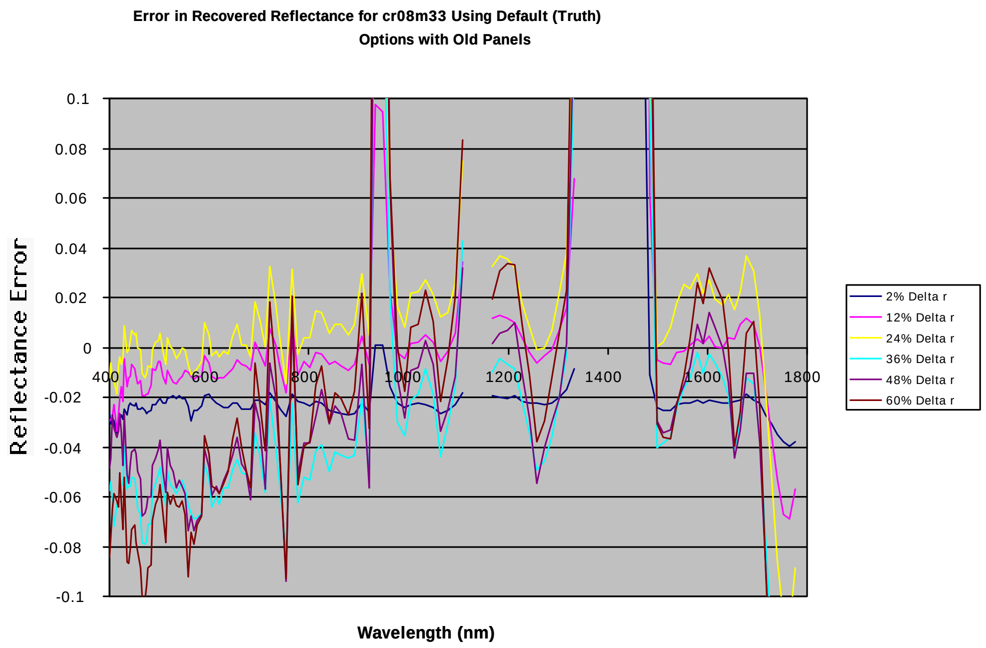

Figure 4.3.1-1. Recovered reflectance error for cr08m33 old panels using all default (truth) for options.

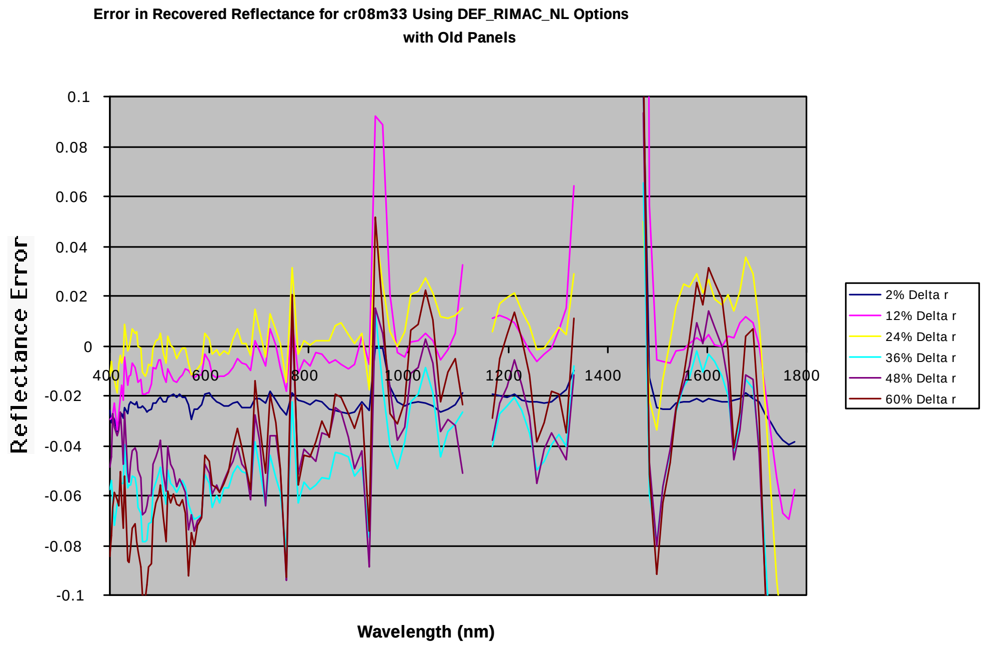

Figure 4.3.1-2. Recovered reflectance error for cr08m33 old panels using default (truth) for elevation, RIMAC for visibility, and NLLSSF for water vapor.

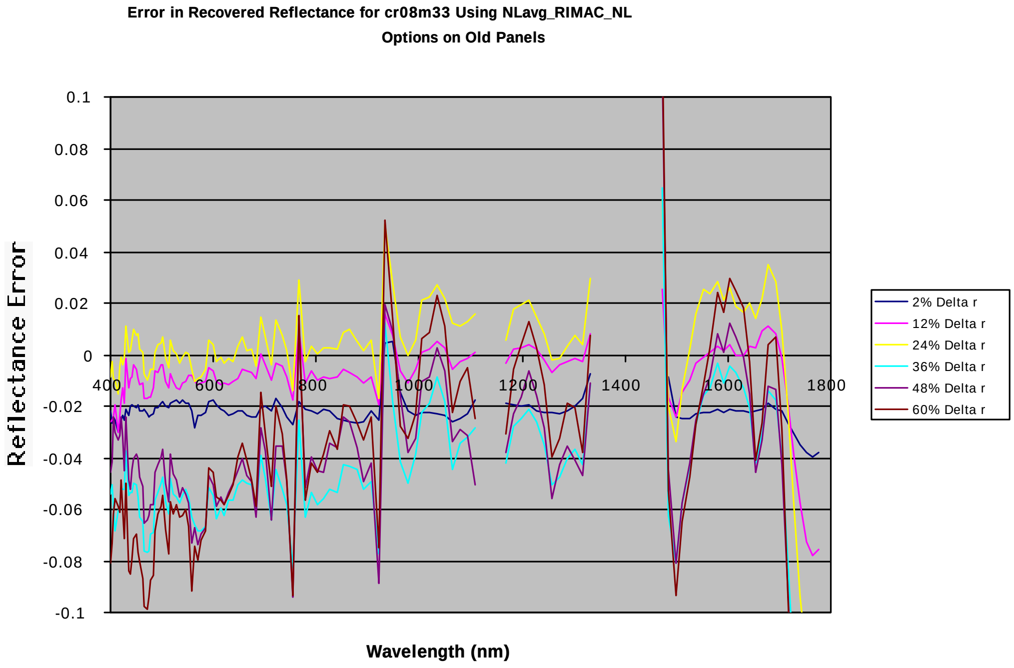

Figure 4.3.1-3. Recovered reflectance error from cr08m33 old panels using image-wide average NLLSSF elevation, RIMAC for visibility, and NLLSSF for water vapor.

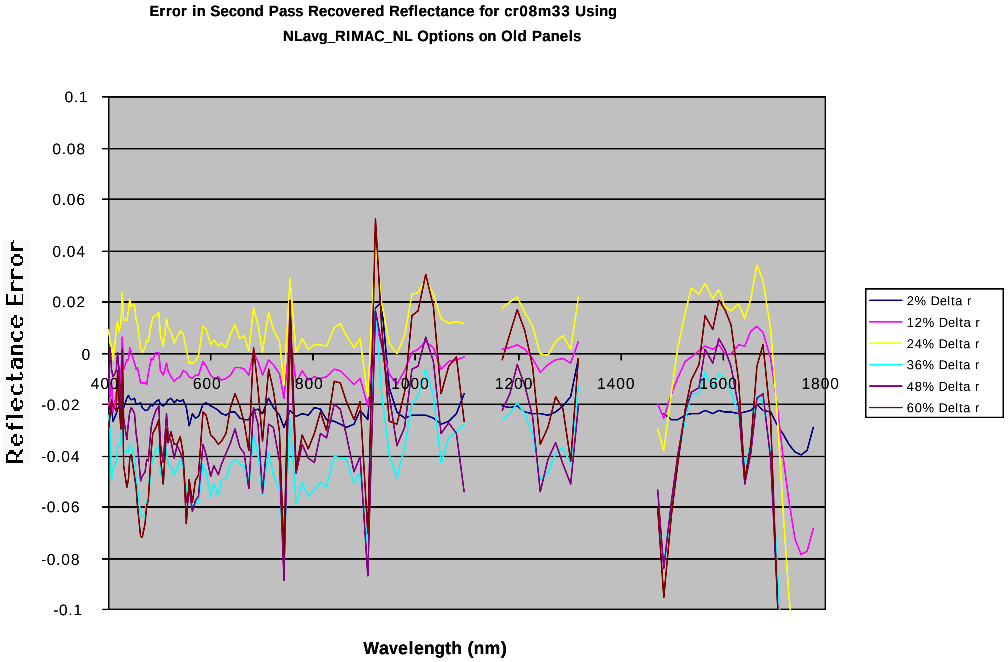

Figure 4.3.1-4. Second pass recovered reflectance error from cr08m33 old panels using image-wide average NLLSSF elevation, RIMAC for visibility, and NLLSSF for water vapor.

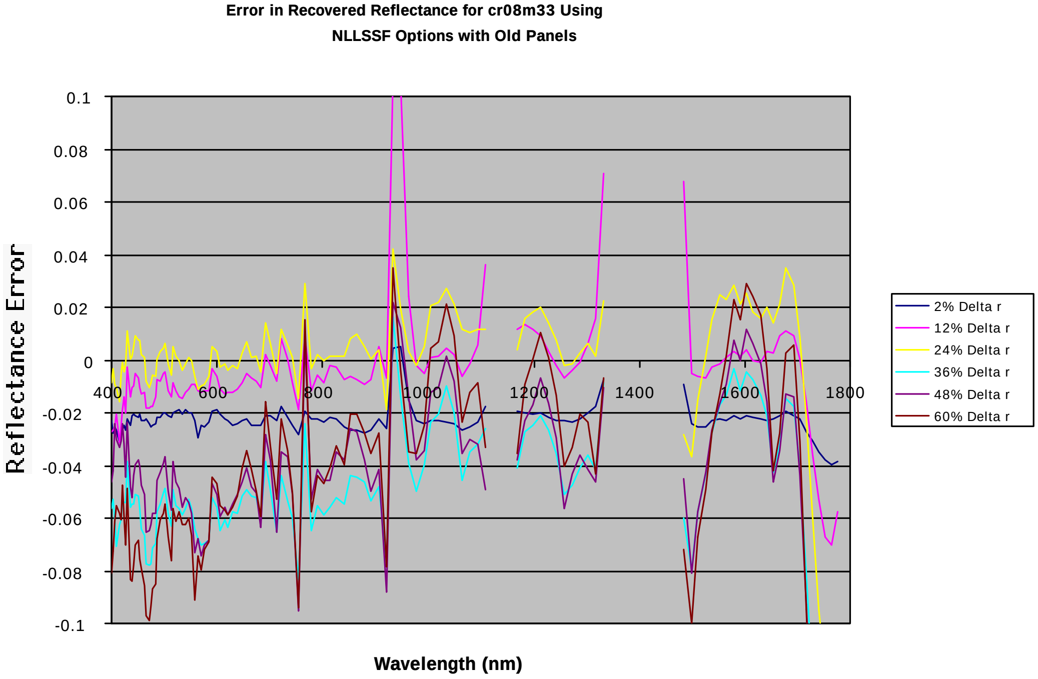

Figure 4.3.1-5. Recovered reflectance error from cr08m33 old panels using NLLSSF for all options.

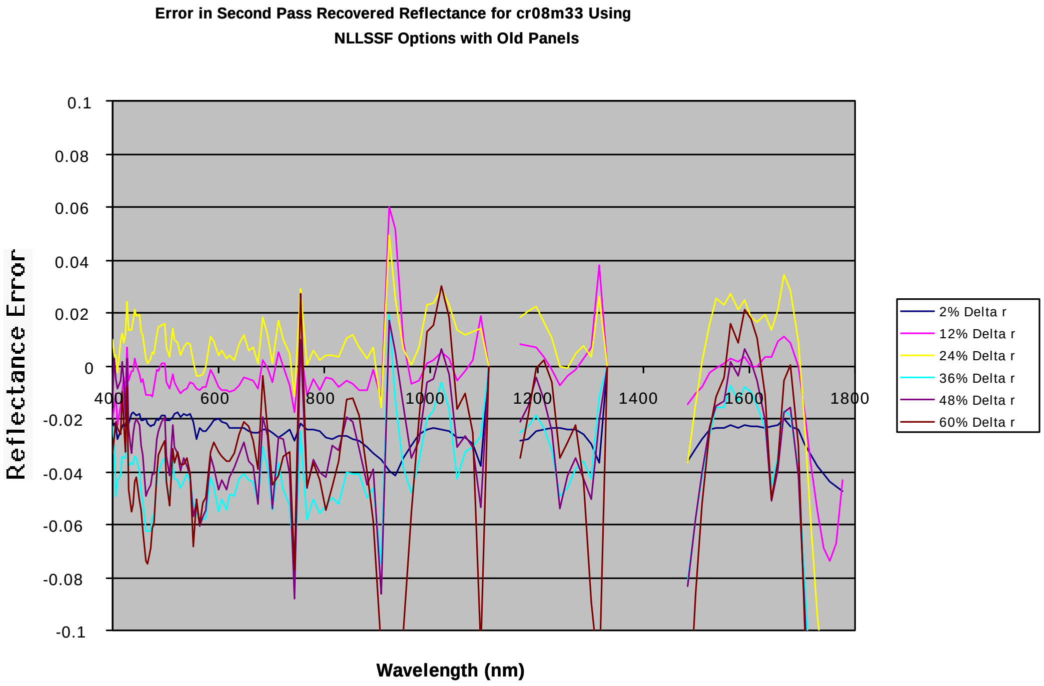

Figure 4.3.1-6. Second pass recovered reflectance error from cr08m33 old panels using NLLSSF for all options.

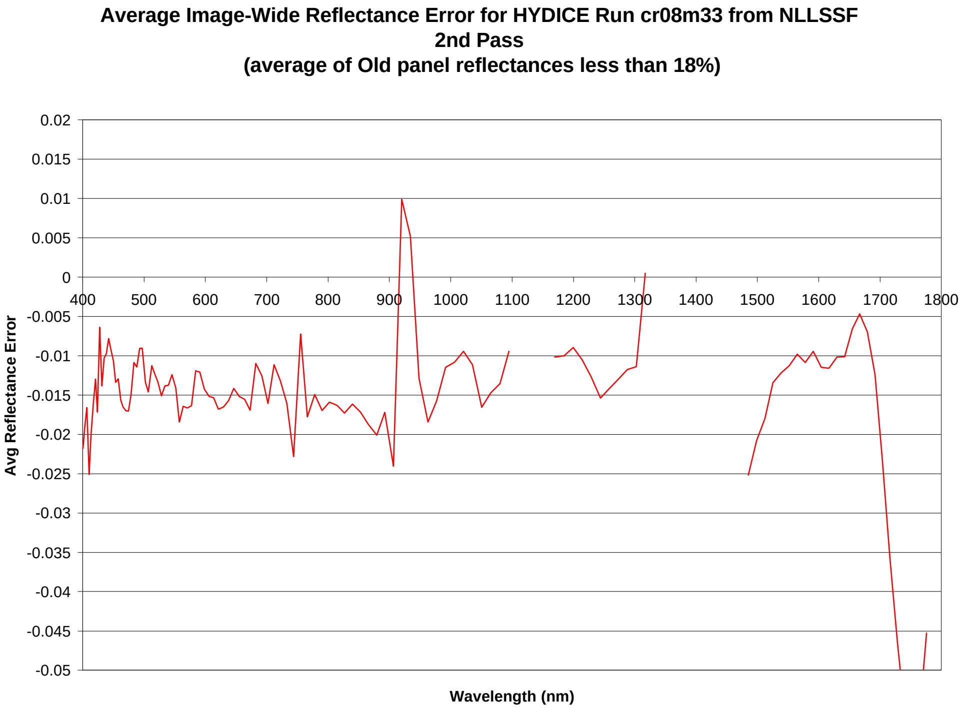

Figure 4.3.1-7. Estimated image-wide reflectance error for ground targets of 18% reflectance or less.

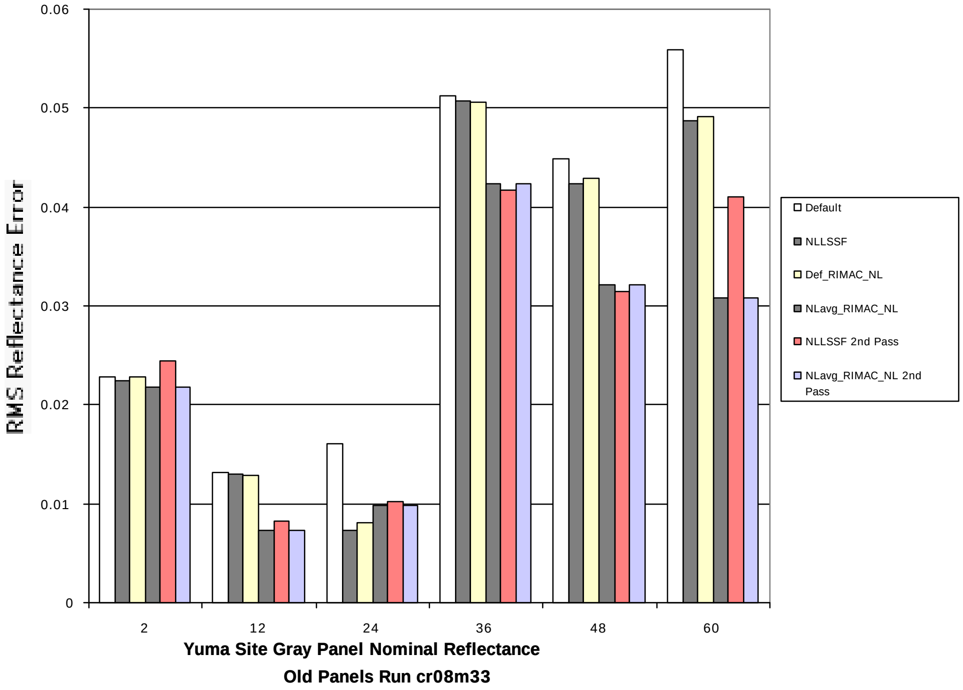

Figure 4.3.1-8. Yuma site run cr08m33 RMS recovered reflectance errors for old panels.

Elevation Aerosol Vis Water Vapor	Default	NLavg RIMAC NLLSSF	NLLSSF	NLavg RIMAC NLLSSF 2nd Pass	NLLSSF 2nd Pass
Surface Elevation (km)	0.265	0.459	0.496	0.797	0.807
Visibility (km)	70.00	68.64	52.779	45.798	51.851
Water Vapor (g/cm^2)	2.146	1.571	1.552	1.431	1.435

Table 4.3.1-1. Estimated atmospheric parameters from using different options in the inversion from sensor radiance to ground reflectance algorithm. Note: The surface elevation is also coupled to the pressure profile in the radiosonde and the water vapor amount is the total sun-target-sensor column value.

4.3.2 Cr08m33 New Panels

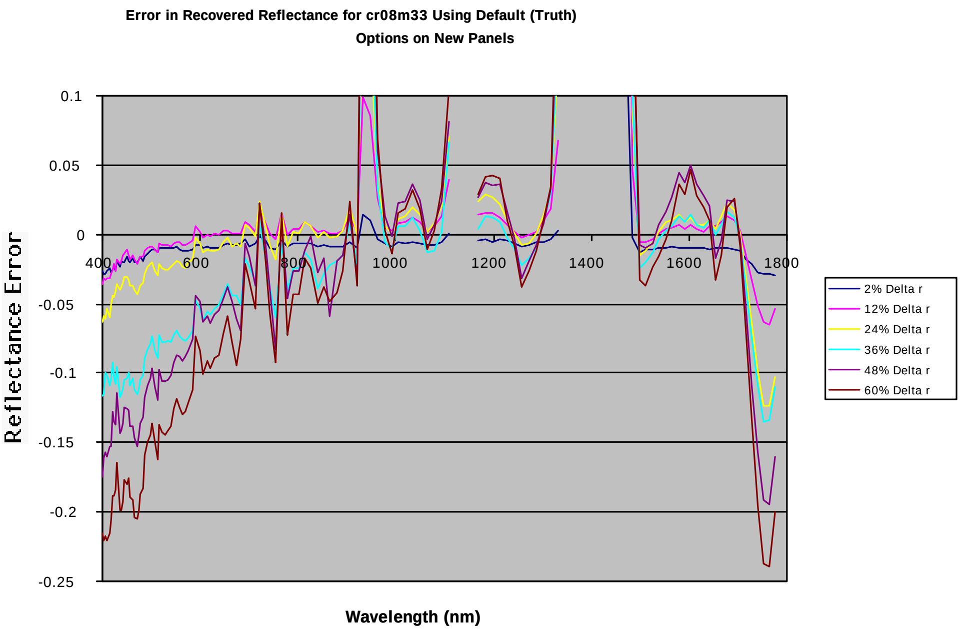

Figure 4.3.2-1. Recovered reflectance error for cr08m33 new panels using default (truth) options.

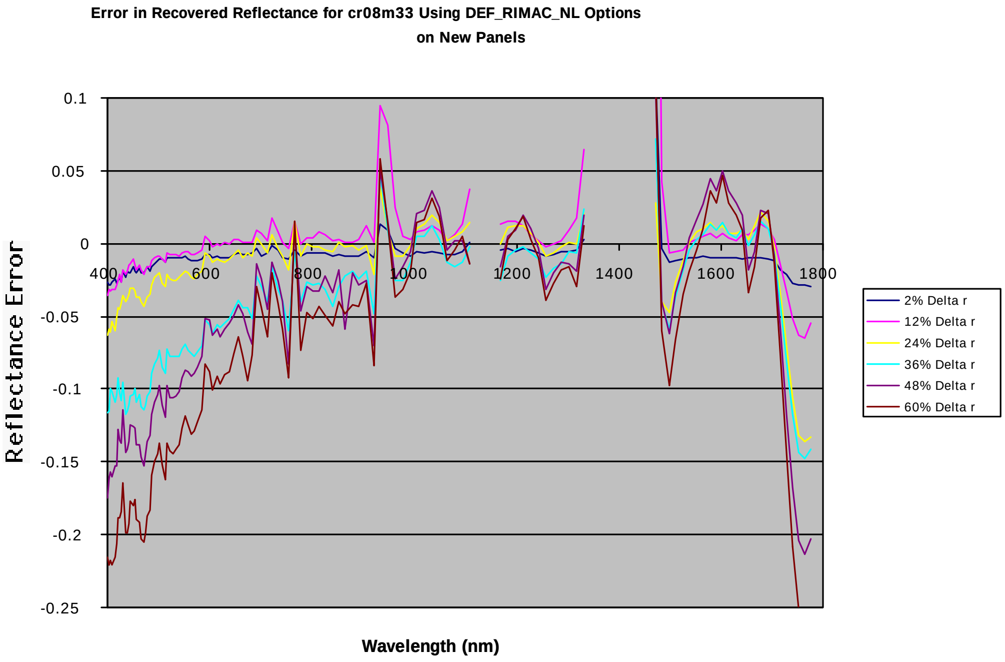

Figure 4.3.2-2. Recovered reflectance error for cr08m33 new panels using default (truth) for elevation, RIMAC for visibility, and NLLSSF for water vapor.

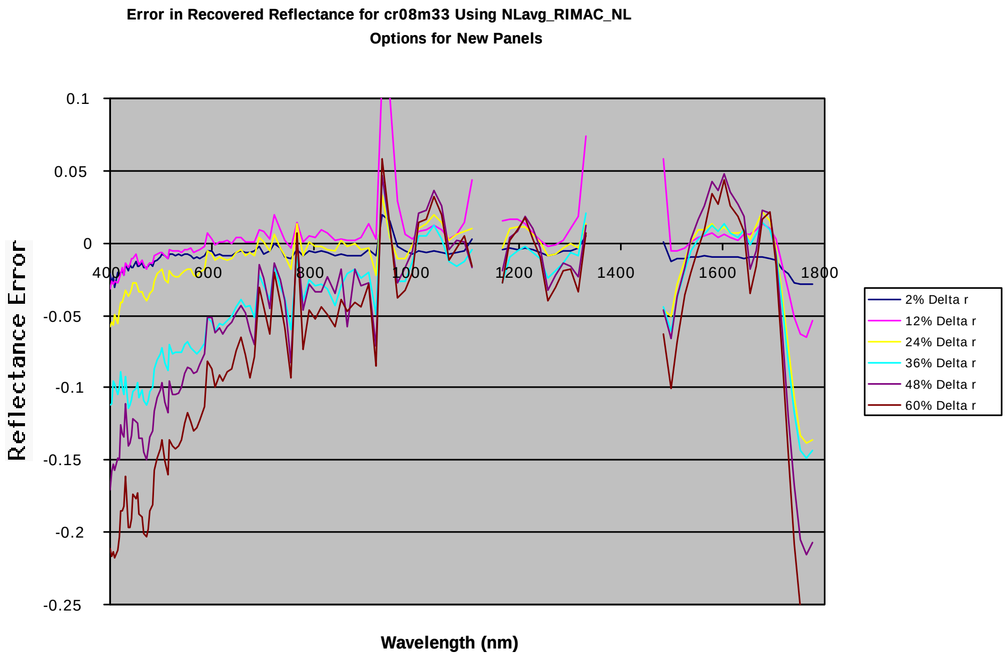

Figure 4.3.2-3. Recovered reflectance error from cr08m33 new panels using image-wide average NLLSSF elevation, RIMAC for visibility, and NLLSSF for water vapor.

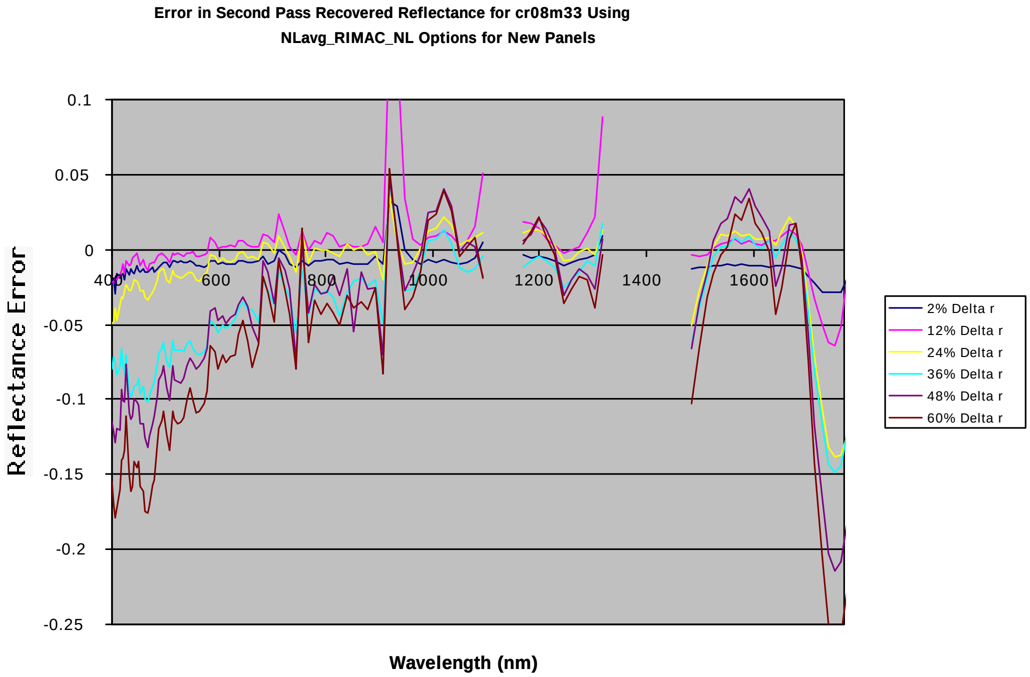

Figure 4.3.2-4. Second pass recovered reflectance error from cr08m33 new panels using image-wide average NLLSSF elevation, RIMAC for visibility, and NLLSSF for water vapor.

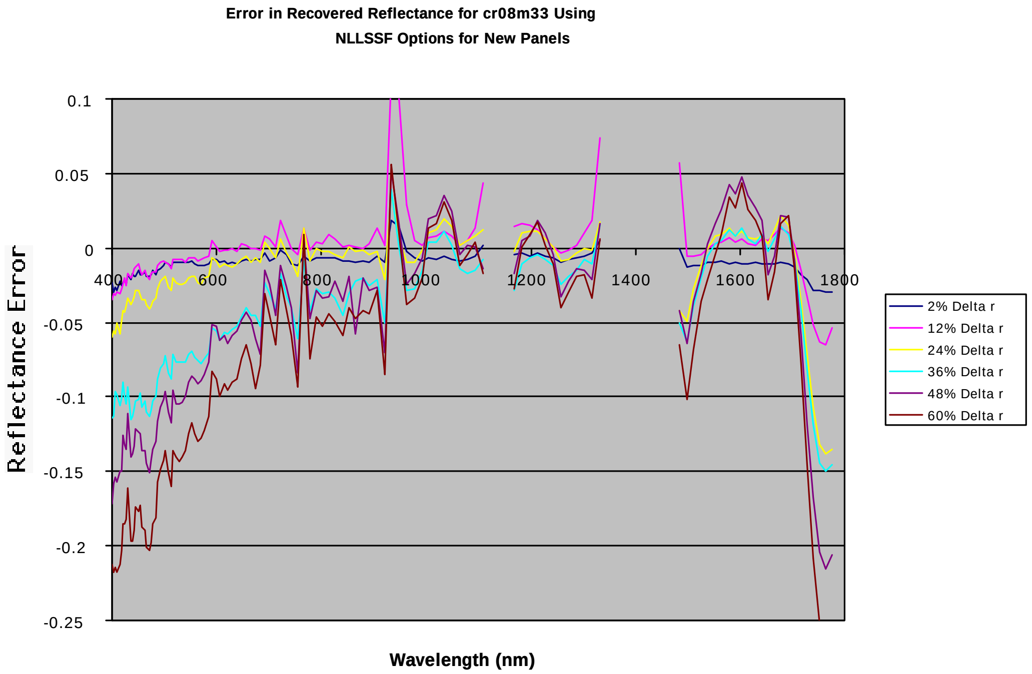

Figure 4.3.2-5. Recovered reflectance error from cr08m33 new panels using NLLSSF for all options.

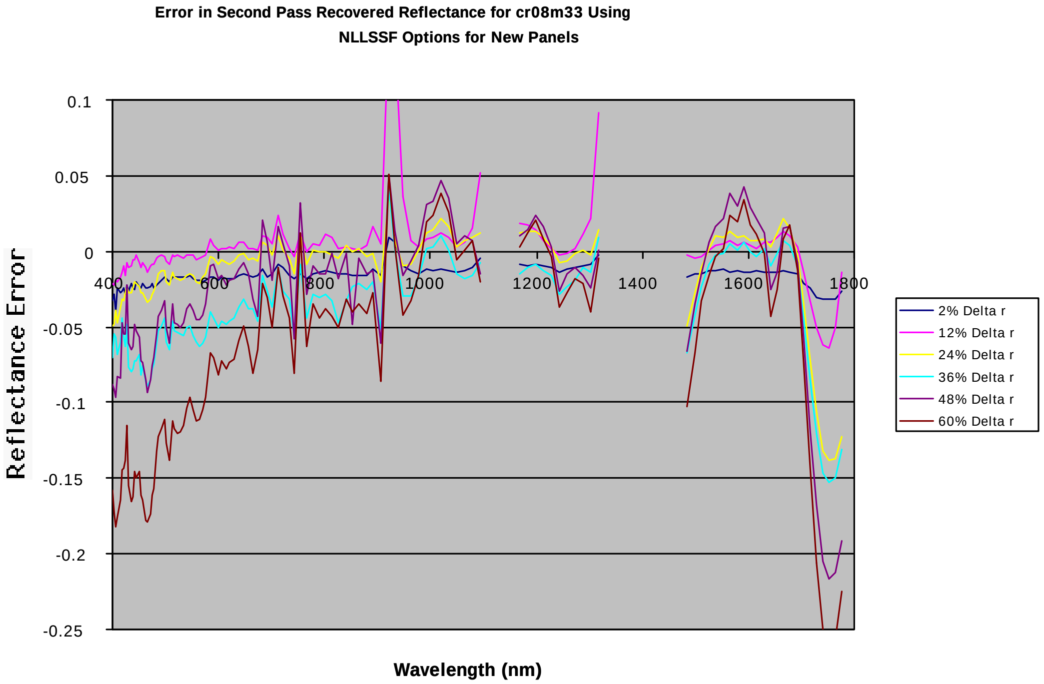

Figure 4.3.2-6. Second pass recovered reflectance error from cr08m33 new panels using NLLSSF for all options.

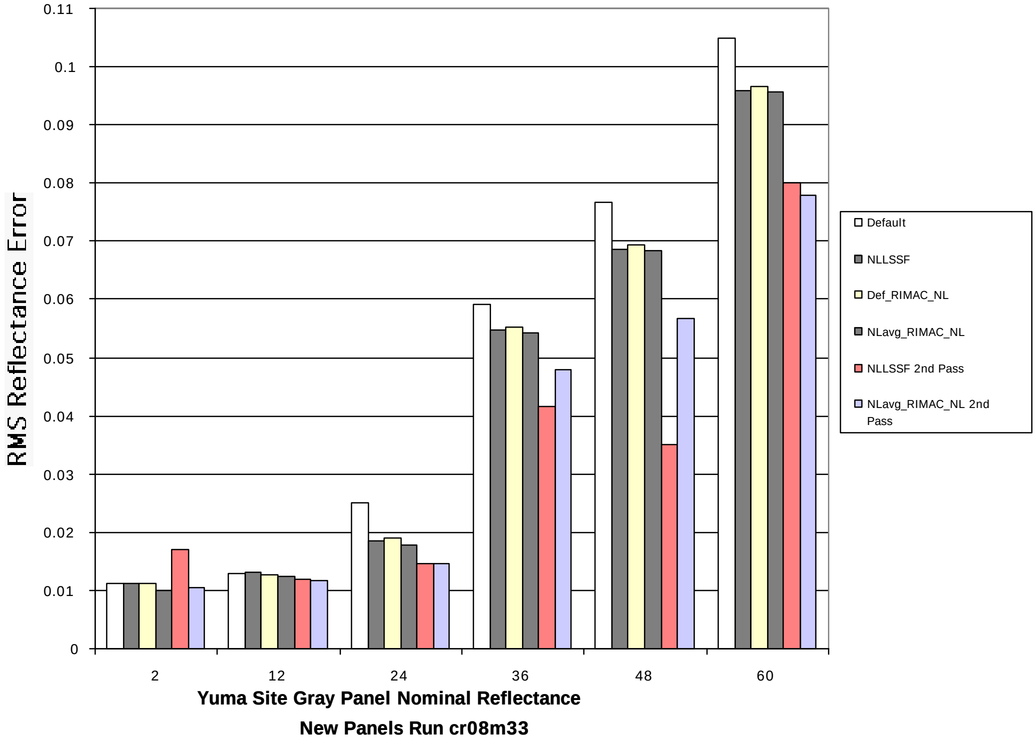

Figure 4.3.2-7. Yuma site run cr08m33 RMS recovered reflectance errors for new panels.

Elevation Aerosol Vis Water Vapor	Default	NLavg RIMAC NLLSSF	NLLSSF	NLavg RIMAC NLLSSF 2nd Pass	NLLSSF 2nd Pass
Surface Elevation (km)	0.265	0.5087	0.514	0.815	0.813
Visibility (km)	70.00	65.08	48.27	44.888	37.37
Water Vapor (g/cm^2)	2.146	1.53	1.504	1.42	1.413

Table 4.3.2-1. Estimated atmospheric parameters from using different options in the inversion from sensor radiance to ground reflectance algorithm. Note: The surface elevation is also coupled to the pressure profile in the radiosonde and the water vapor amount is the total sun-target-sensor column value.

This set of imagery presented a different problem when viewing both the recovered reflectance and reflectance errors for each of the panels. The first observable artifact is the "ringing" at the location of the 760nm oxygen band and the major water-vapor absorption features due to a difference between the spectral locations of these features in the HYDICE imagery and the MODTRAN database. In fact, all recovered spectra for this run are noisy due to this spectral misalignment. This could very likely be a result of a spectral miscalibration with HYDICE at this early acquisition date. The channel wavelength band center locations in HYDICE depend on the atmospheric pressure. This is a consequence of the prism dispersion element used in the HYDICE instrument. Any error in atmospheric pressure or in the pressure compensation calculation for HYDICE would be propagated into a spectral shift from the truth band center(s).

All of the first-pass recovered reflectance spectra had errors that increased as the blue region was approached. The errors in the blue region were decreased significantly by a second pass through the algorithm. Again, this validates the use of the atmospheric point spread function to accounting for the target surround contributions. But, the error still indicates that some parameter(s) were not accounted for or incorrectly calculated.

This error could be due to the MODTRAN database phase function incorrectly modeling the real atmosphere, background effects (*i.e*. shape factor) not accounted for in the radiative transfer equation, the panels having some nonuniform BRDF, or some other radiative transfer modeling error. Since both "Old" and "New" panel images were obtained from the same image and are located in the same general, it would be expected that the recovered reflectance error would be approximately equal for both. This is certainly not the case.

For an example, compare Figure 4.3.1-6 and 4.3.2-6. The error is much greater for the "New" panel image even though the estimates of atmospheric parameters for each image were similar. Since the error is negative, it means that more photons are needed at the sensor to recover a higher reflectance value. Making the atmosphere thinner (*i.e*., increasing the visibility) will not increase the flux at the sensor to any great degree since the visibility is already very high. The most likely path to increase the number of photons in the model is to add a shape factor to the atmospheric downwelling radiance term (Schott, 1997) and account for solar energy reflecting from a nearby structure or object onto the panels. By virtue of the error being highest in the blue, vegetation is excluded from being the object. It is most likely that the newer panels may have been placed in a small gulley or ravine and some sunlight reflected from nearby (minerals?) objects onto the new panels. This explanation would also account for the larger recovered reflectance error being associated with the brighter panels; the higher the reflectance of the panel, the larger the portoin of reflected radiance that would return to the sensor. Presently, the radiative transfer equations included in this atmospheric correction algorithm are inadequate to compensate for this effect. A more complex equation must be incorporated which would include the radiative transfer path from a nearby object scaled by a shape factor that represents (the solid angle fraction of the hemisphere "seen" by the panels), and scaling (reducing) of the atmospheric downwelled radiance by the remaining hemispherical fraction.

The shape factor would also need to be known or closely estimated and the spectral reflectance of the sand would also be required to improve upon the recovered panel spectral reflectance. Another reasonable solution would be that the BRDF for the new panels was not uniform and the reflectance decreased steeply in the blue. Moisture on the panels would certainly affect the BRDF.

Since the error bias is fairly flat and still negative for the "Old" panels, it is safe to assume that some small shape factor due to the presence of sand mounds could have increased the photon flux onto the panels.

As in the HYDICE Run 29 case, the RIMAC method is comparable to the NLLSSF method in that the RMS errors and spectral reflectance errors were usually very similar. The RIMAC aerosol visibility was always closer to the measured ground truth parameter than the result from the NLLSSF method. Also the RIMAC performed very well considering that the recovered reflectance spectra contained so much noise from the spectral misalignment. It should be noted that the bands used in the RMS error calculations were trimmed from that stated at the beginning of this section. An effort was made to exclude the bands that exhibited ringing from the absorption band spectral misalignment where the spectral features from the MODTRAN 4 model(s) were shifted slightly with respect to the sensor spectra.

Figure 4.3.1-7 has been presented to give a metric of how well the algorithm would perform given a scene with these atmospheric conditions and the spectral calibration of the instrument at that time.

4.4 HYDICE Western Rainbow Image (High Altitude)

This is the second Western Rainbow HYDICE image set of the collection effort that took place on October 21, 1995 at the Yuma proving grounds. This image set was acquired by the

HYDICE sensor at an altitude of 3.114km and is referred to as the "high-altitude set". As stated previously in Section 4.3, both the Old and New panel images from this acquisition were cut from the same original HYDICE scene. The following plots are the result of different combinations of parameter estimation techniques used on these images to derive ground reflectance from the sensor radiance. The MODTRAN LUT generated for the inversion used the desert aerosol model.

4.4.1 Cr15m50 Old Panels

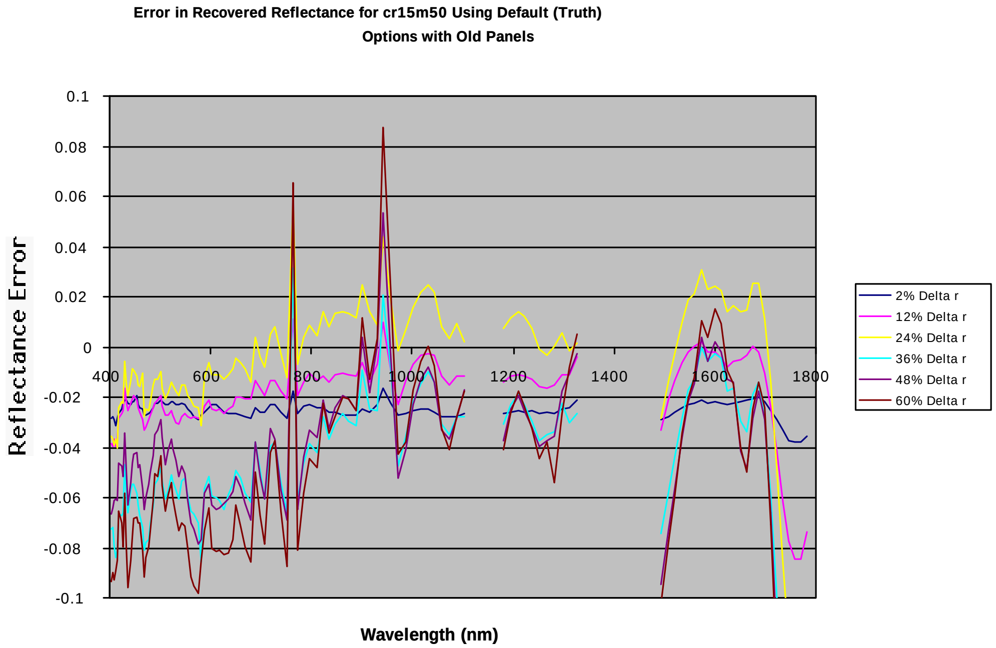

Figure 4.4.1-1. Recovered reflectance error for cr15m50 old panels using default (truth) options.

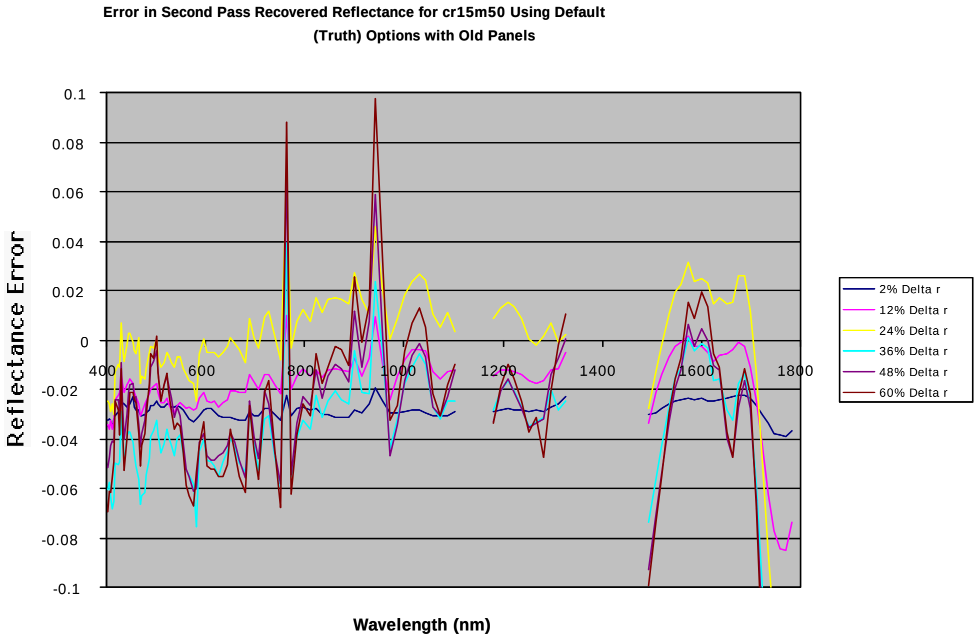

Figure 4.4.1-2. Second pass recovered reflectance error for cr15m50 old panels using default (truth) options.

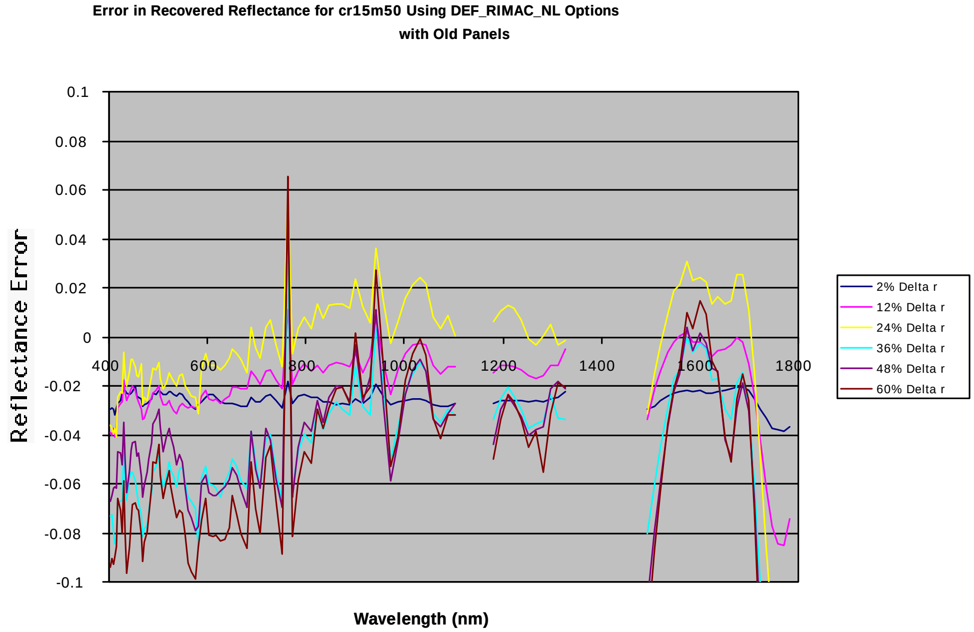

Figure 4.4.1-3. Recovered reflectance error for cr15m50 old panels using default (truth) for elevation, RIMAC for visibility, and NLLSSF for water vapor.

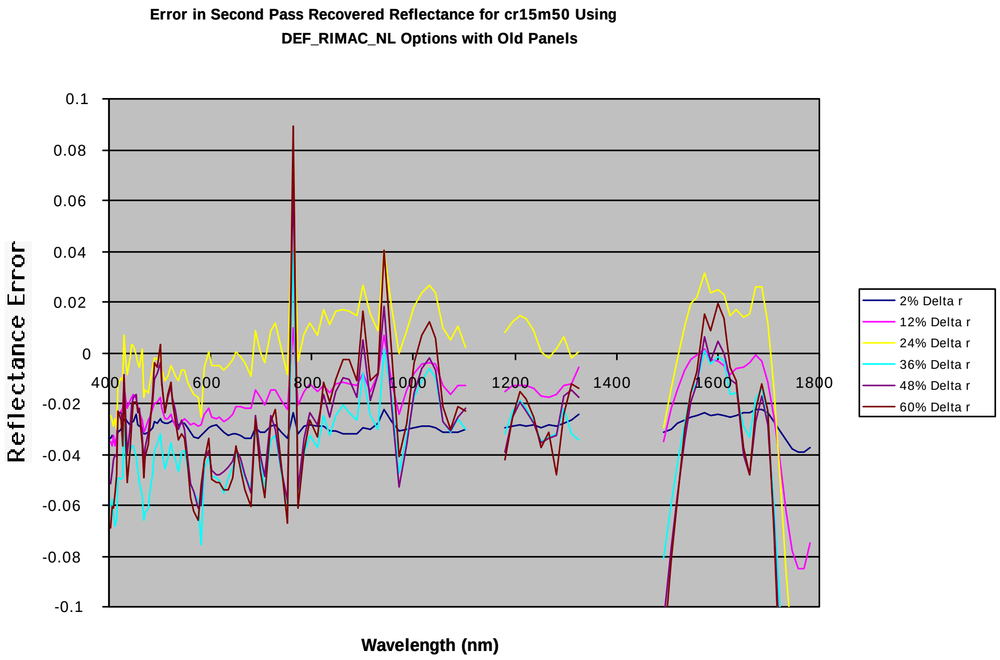

Figure 4.4.1-4. Second pass recovered reflectance error for cr15m50 old panels using default (truth) for elevation, RIMAC for visibility, and NLLSSF for water vapor.

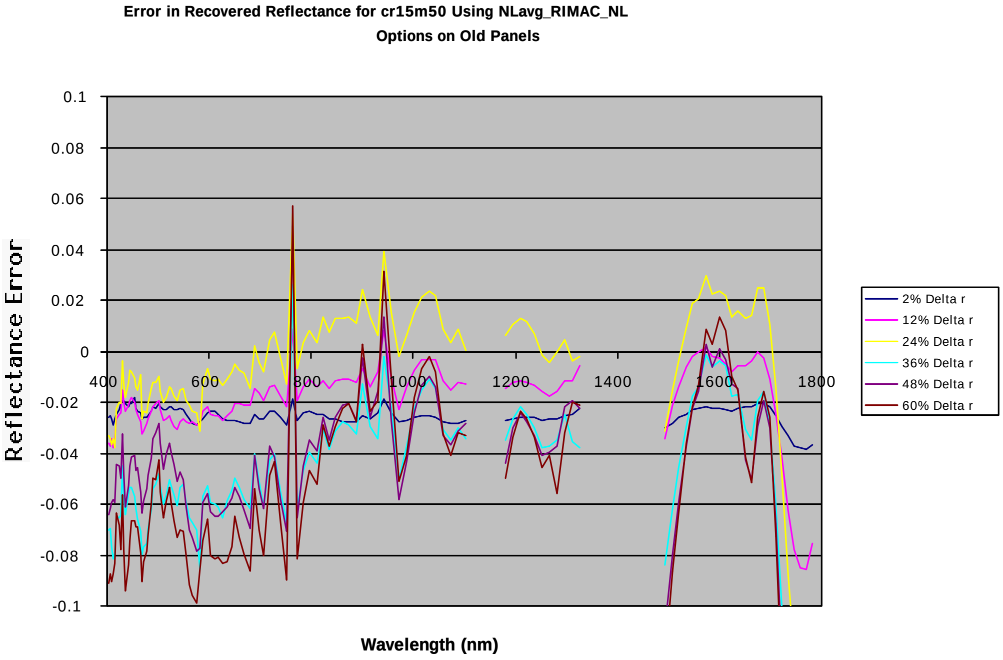

Figure 4.4.1-5. Recovered reflectance error from cr15m50 old panels using image-wide average NLLSSF elevation, RIMAC for visibility, and NLLSSF for water vapor.

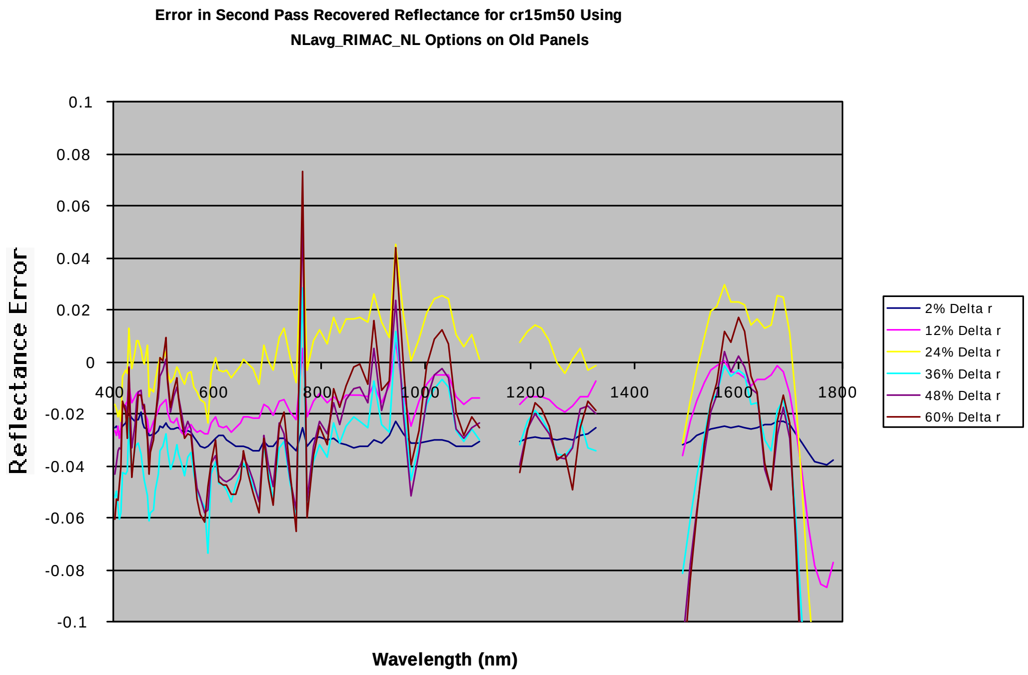

Figure 4.4.1-6. Second pass recovered reflectance error from cr15m50 old panels using image-wide average NLLSSF elevation, RIMAC for visibility, and NLLSSF for water vapor.

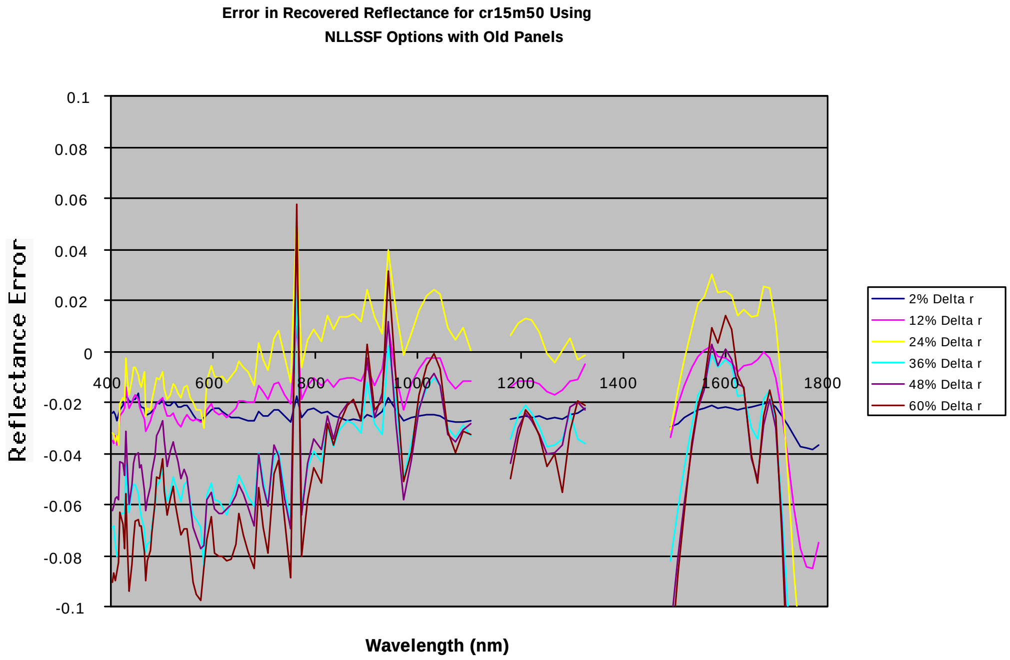

Figure 4.4.1-7. Recovered reflectance error from cr15m50 old panels using NLLSSF for all options.

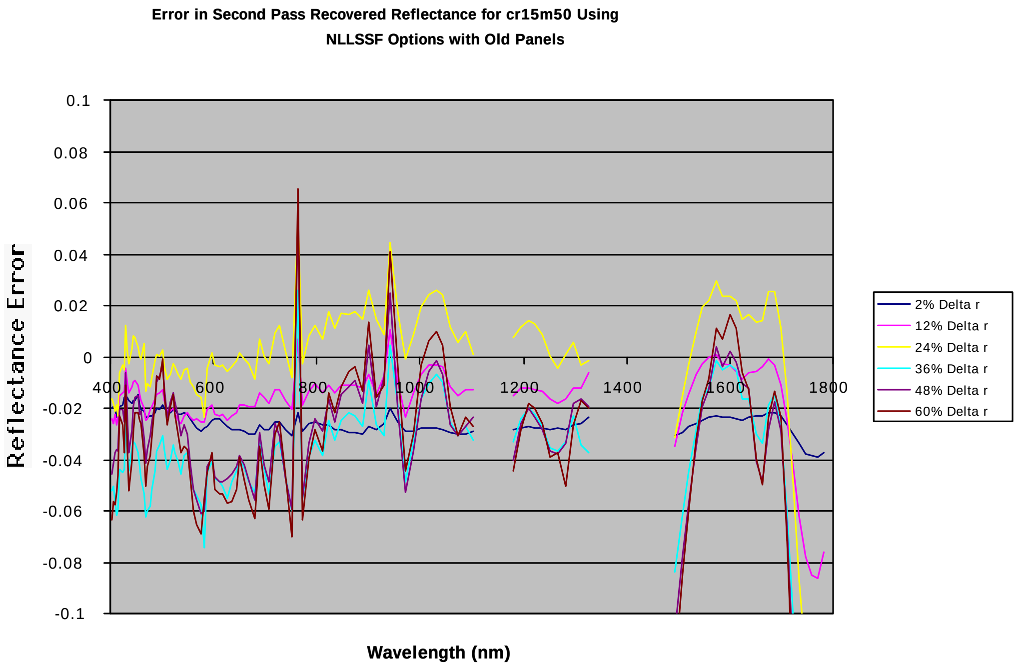

Figure 4.4.1-8. Second pass recovered reflectance error from cr15m50 old panels using NLLSSF for all options.

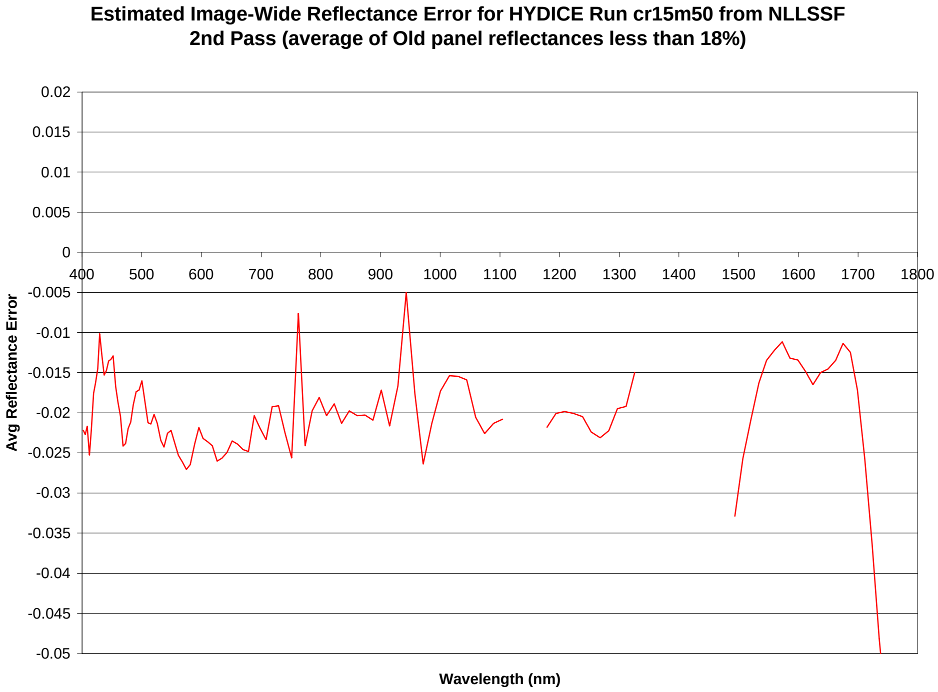

Figure 4.4.1-9. Estimated image-wide reflectance error for ground targets of 18% reflectance or less.

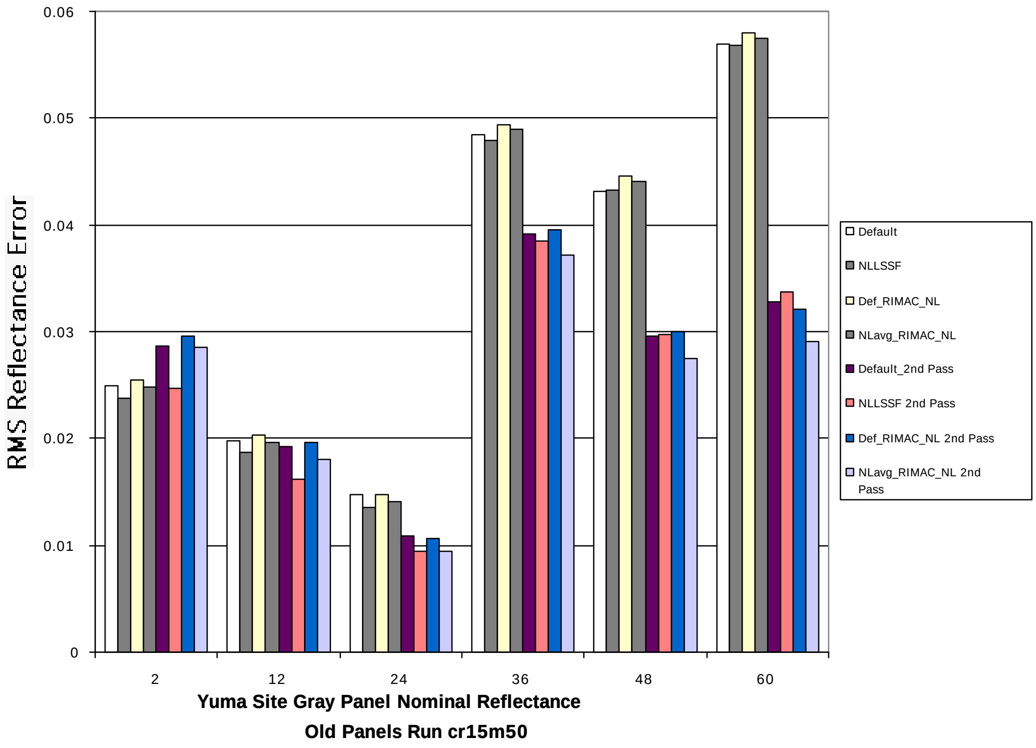

Figure 4.4.1-10. Yuma site run cr15m50 RMS recovered reflectance errors for old panels.

Elevation Aerosol Vis Water Vapor	Default	Default RIMAC NLLSSF	NLavg RIMAC NLLSSF	NLLSSF	NLavg RIMAC NLLSSF 2nd Pass	NLLSSF 2nd Pass
Surface Elevation (km)	0.265	0.265	0.479	0.480	0.787	0.787
Visibility (km)	70.0	66.11	69.83	69.887	69.64	69.64
Water Vapor (g/cm^2)	2.0784	2.103	2.078	2.078	2.02	2.02

Table 4.4.1-1. Estimated atmospheric parameters from using different options in the inversion from sensor radiance to ground reflectance algorithm. Note: The surface elevation is also coupled to the pressure profile in the radiosonde and the water vapor amount is the total sun-target-sensor column value.

4.4.2 Cr15m50 New Panels

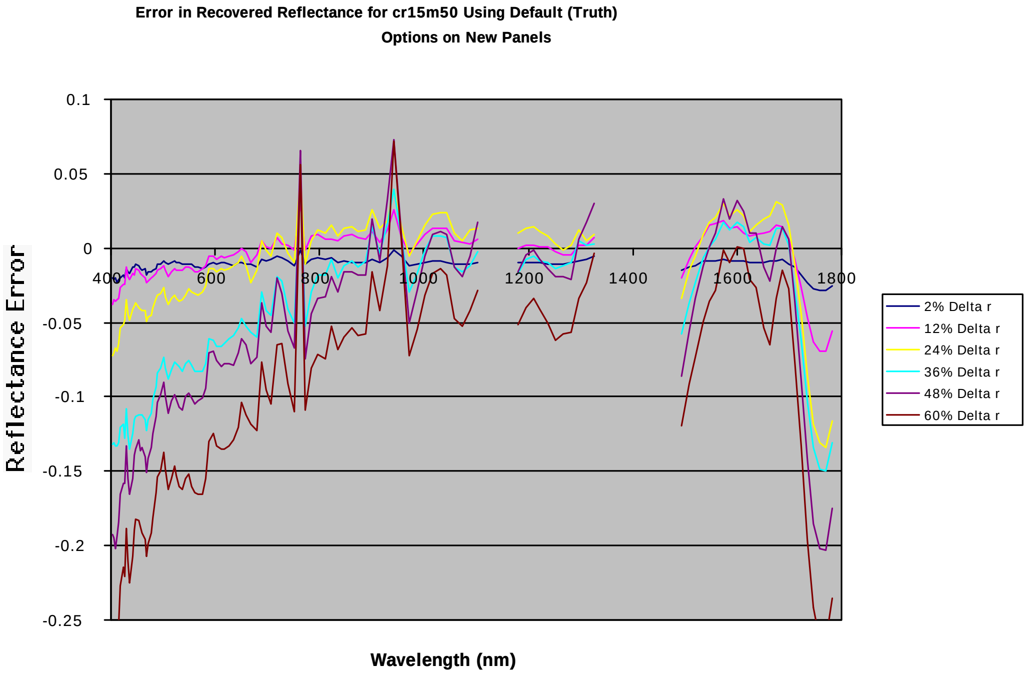

Figure 4.4.2-1. Recovered reflectance error for cr15m50 new panels using default (truth) options.

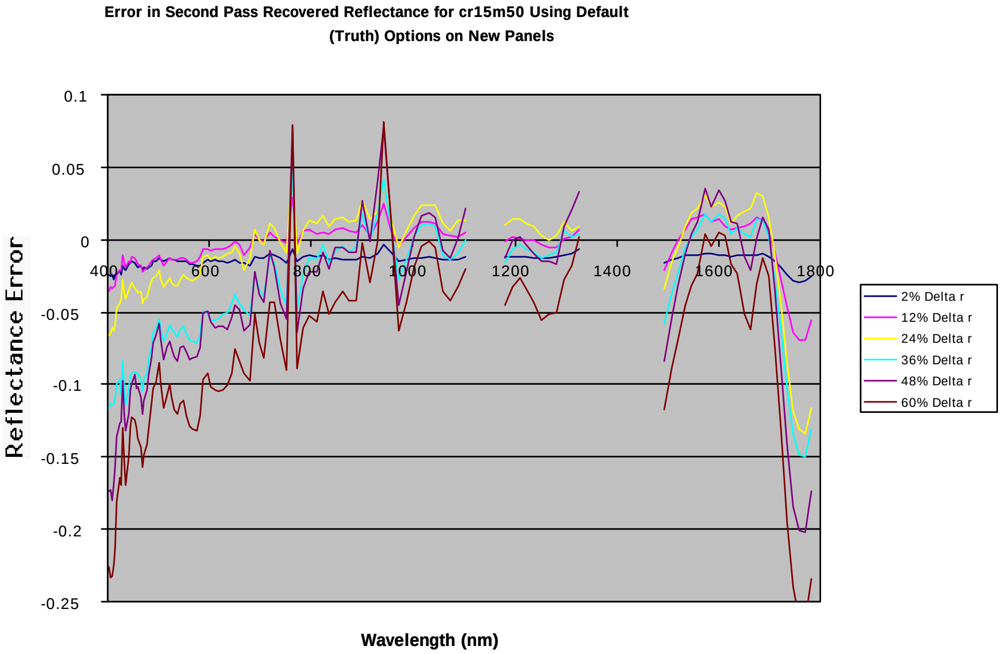

Figure 4.4.2-2. Second pass recovered reflectance error for cr15m50 new panels using default (truth) options.

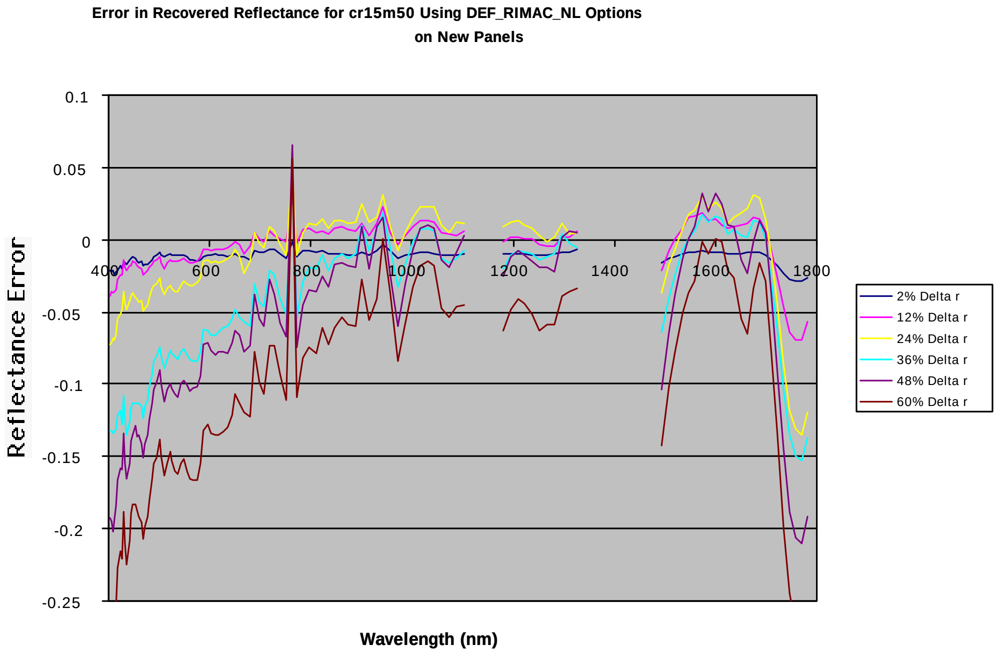

Figure 4.4.2-3. Recovered reflectance error for cr15m50 new panels using default (truth) for elevation, RIMAC for visibility, and NLLSSF for water vapor.

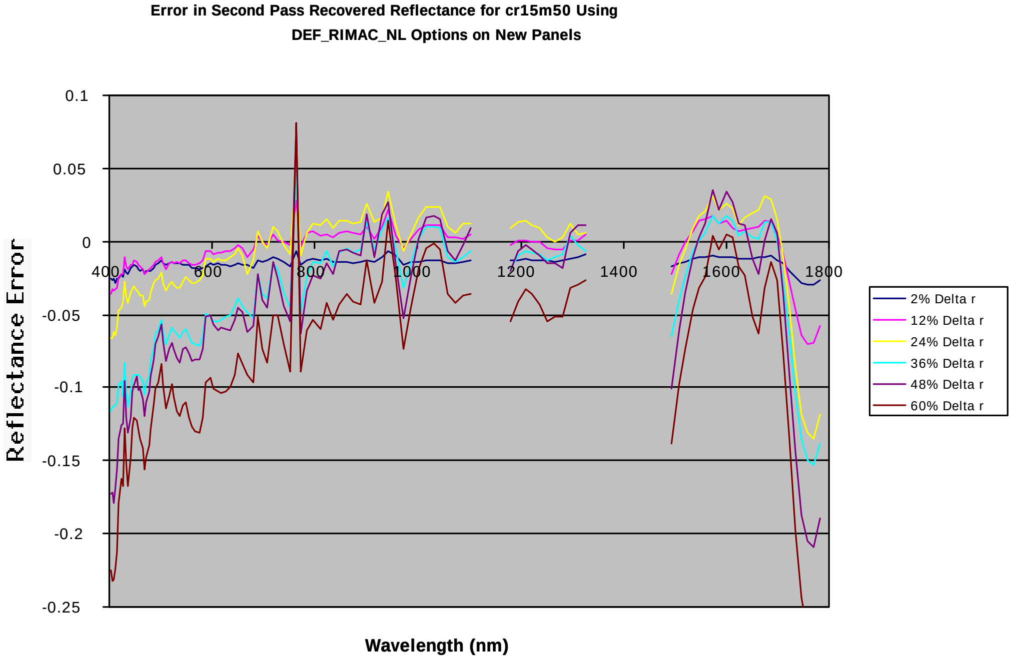

Figure 4.4.2-4. Second pass recovered reflectance error for cr15m50 new panels using default (truth) for elevation, RIMAC for visibility, and NLLSSF for water vapor.

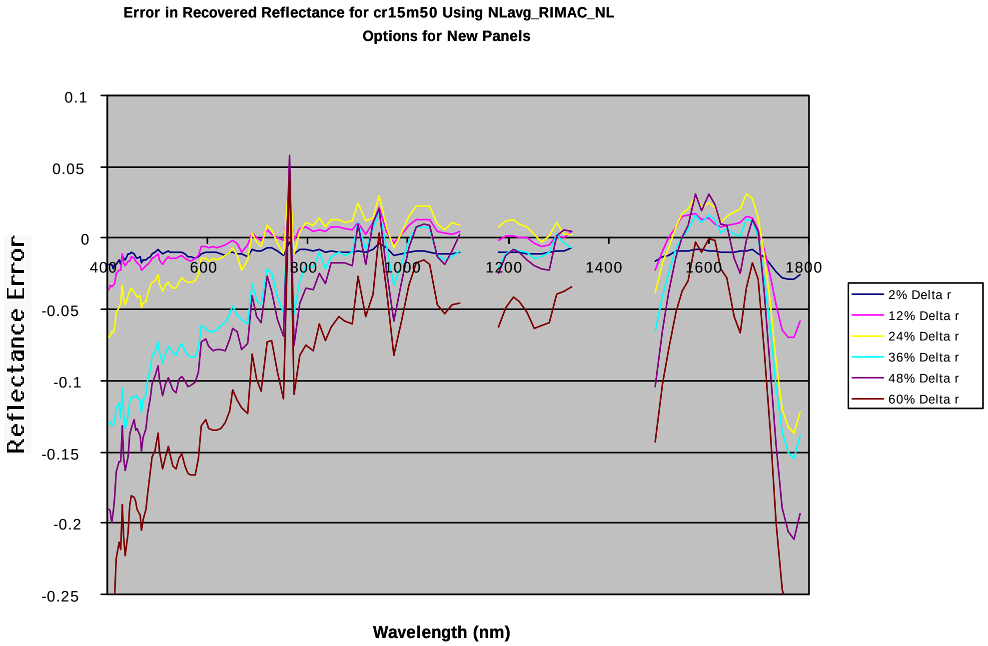

Figure 4.4.2-5. Recovered reflectance error from cr15m50 new panels using image-wide average NLLSSF elevation, RIMAC for visibility, and NLLSSF for water vapor.

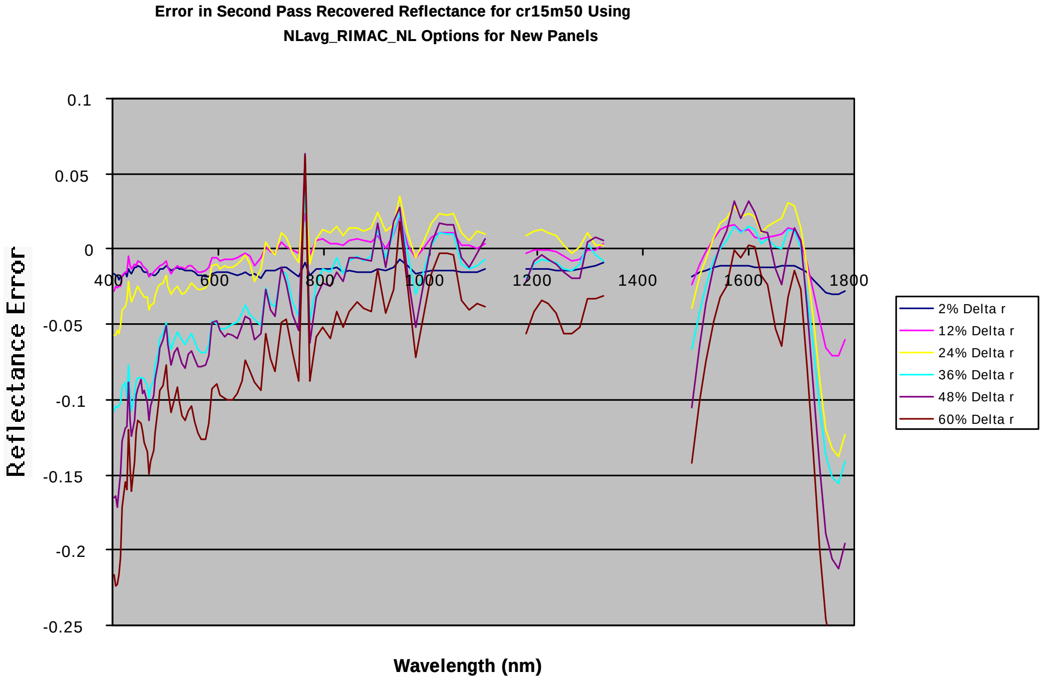

Figure 4.4.2-6. Second pass recovered reflectance error from cr15m50 new panels using image-wide average NLLSSF elevation, RIMAC for visibility, and NLLSSF for water vapor.

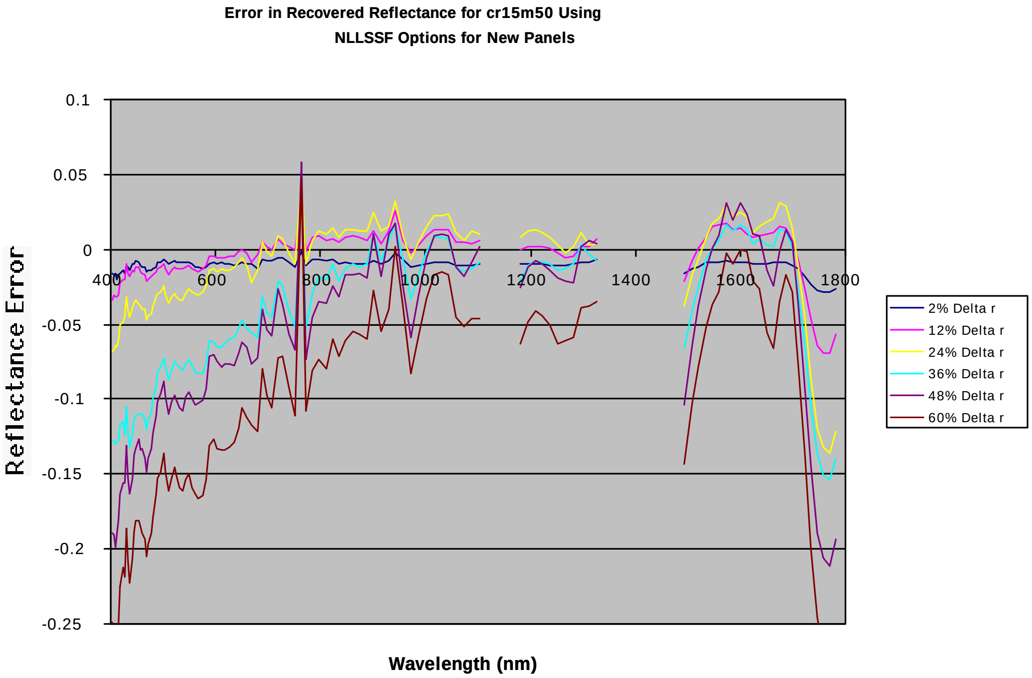

Figure 4.4.2-7. Recovered reflectance error from cr15m50 new panels using NLLSSF for all options.

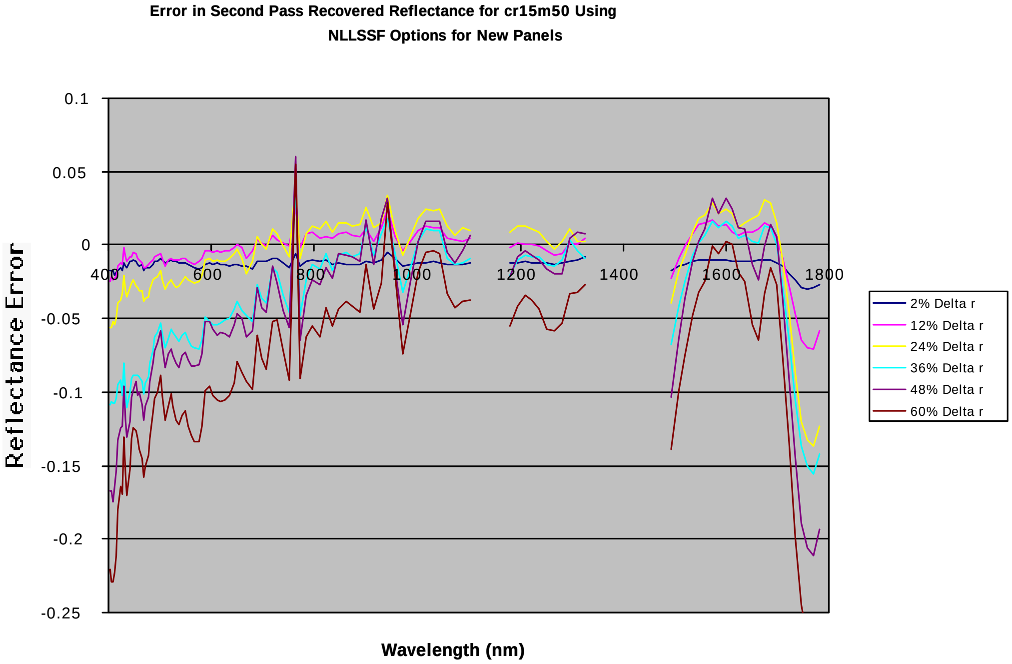

Figure 4.4.2-8. Second pass recovered reflectance error from cr15m50 new panels using NLLSSF for all options.

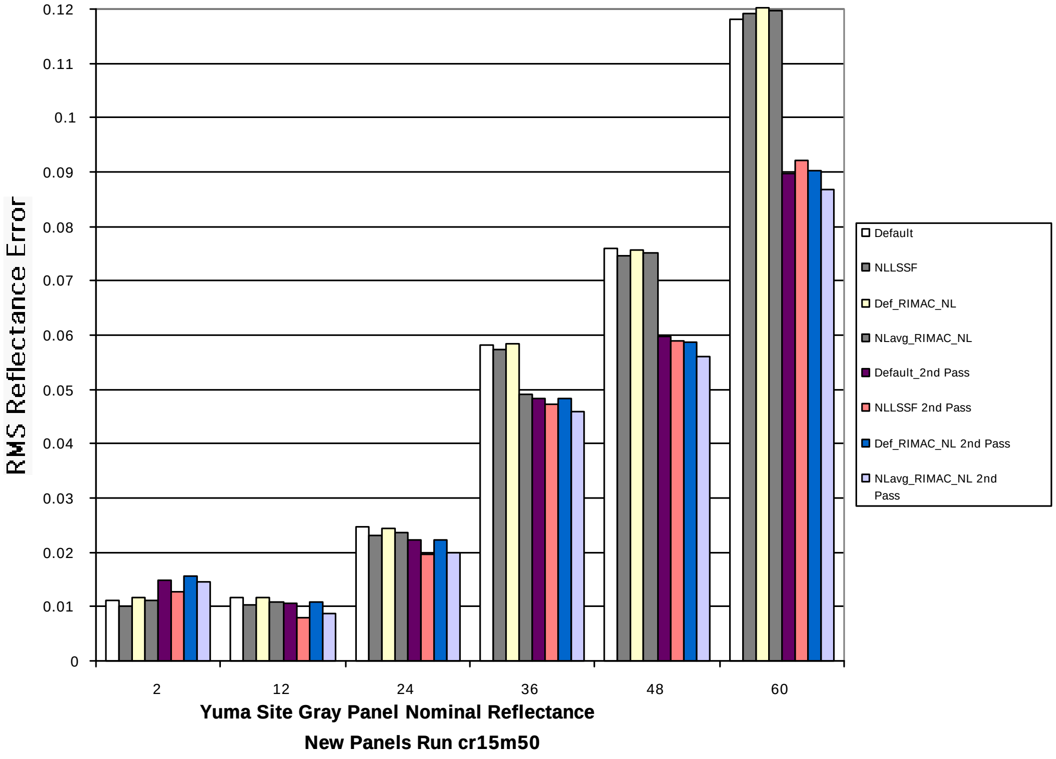

Figure 4.4.2-9. Yuma site run cr15m50 RMS recovered reflectance errors for new panels.

<u>Elevation</u> <u>Aerosol Vis</u> Water Vapor	Default	Default RIMAC NLLSSF	NLavg RIMAC NLLSSF	NLLSSF	NLavg RIMAC NLLSSF 2nd Pass	NLLSSF 2nd Pass
Surface Elevation (km)	0.265	0.265	0.479	0.479	0.812	0.810
Visibility (km)	70.0	66.504	59.79	69.747	49.32	69.58
Water Vapor (g/cm^2)	2.0784	2.097	2.036	2.054	1.986	1.98

Table 4.4.2-1. Estimated atmospheric parameters from using different options in the inversion from sensor radiance to ground reflectance algorithm. Note: The surface elevation is also coupled to the pressure profile in the radiosonde and the water vapor amount is the total sun-target-sensor column value.

The amount of spectral ringing in this set of imagery is much less than in the low-altitude run cr08m33, but some misalignment is still apparent judging from the residual noise in the spectral reflectance errors for all of the panels. However, the recovered reflectance spectra using any combination of options was acceptable. The recovered spectral reflectance error was again larger in the blue region after the first-pass inversion. This was especially true for the "New" panels, and in particular for the 48% and 60% gray panels. Again, this indicates that the "New" panel scene exhibited nonuniform BRDF or some topography that must be considered using a more complex radiative transfer equation (as stated at the end of Section 4.3.2). As in previous examples, Figure 4.4.1-9 &4.4.1-10 are presented as the metric for the expected performance of the algorithm.

The modeled adjacency effect from the PSF and second pass through the algorithm again resulted in less error in the blue region. It appears that using an weighted averaged value of the ground reflectance for the adjacency and the trapping effect radiance results in a better inversion to ground reflectance than staying with the assumption that the surround reflectance is equal to the target reflectance (as in the first-pass run). The total RMS spectral error was less for any of the second-pass combinations with the exception in the reflectance recovery of the nominal 2% panel.

The RIMAC again had comparable results with the NLLSSF technique for aerosols in the spectral reflectance recovery and in the total RMS error.

5. Summary

A complete modular algorithm for inverting hyperspectral imagery from sensor radiance to ground reflectance has been constructed and validated. This algorithm incorporates existing and new methodologies for estimating the atmospheric parameters of surface-pressure depth, aerosol-dependent visibility, and columnar water vapor. It provides a much-needed tool for removing the atmosphere from hyperspectral images and facilitates the analysis of the ground reflectance imagery.

A new method referred to as the Regression Intersection Method for Aerosol Correction (RIMAC) has been developed and has peformed favorably when compared to the existing NLLSSF method. The algorithm option combinations in which the RIMAC has been used has resulted in very acceptable reflectance imagery. The RIMAC is a very useful module in that it is an in-scene method that requires no estimate of aerosol visibility by the user and reduces the computer run times when compared to iterative techniques such as the downhill simplex method in NLLSSF.

A new concept has been tested by adding an environmental/adjacency effect to the radiative transfer equation in MODTRAN 4.0 that does not need Monte Carlo methods or ray tracing to determine the contribution of the surround to the target sensor radiance. It is assumed that the total environmental or adjacency radiance can be estimated by:

1) Assuming that the MODTRAN-derived sensor radiance from a surround with unit 1.0 albedo is the summation of equivalent radiance values from discrete directions on the ground that surround the target within a specified projected solid angle. This quantity can be referred to as the resolved adjacency radiance vector.

2) Convolving a convolution kernel derived from a scattering phase function by a close estimate of the ground (the first-pass reflectance image). This results in an average reflectance weighting value for each pixel that can be multiplied by the resolved adjacency radiance vector to give an estimate of the total scattered radiance contribution from the surround.

A new method and a new term for the radiative transfer equation has been developed for use during a second pass through an algorithm to derive ground reflectance from sensor radiance. The resolved adjacency vector is the environmental/adjacency radiance that is multiplied by the weighted average reflectance of the target surround. The success of the algorithm in reducing the recovered spectral reflectance error in the blue/green regions of the spectrum and reducing the total RMS spectral reflectance error has been documented.

The mean error in recovered reflectance for the earth albedo average of 0.18 (or less) is approximately 0.01 reflectance units (Figure 5-1). This shows that the reflectance recovery compared to truth is very good for average reflectors on the earth surface. Some of this error can be attributed to the sample size of the ground truth being unequal to ground-projected detector pixel on the panel, while the remainder is most likely atmospheric/spectral modeling error.

Another observation can be made from Figure 5-1. One of the reasons that the reflectance recovery is so accurate for targets of 18% reflectance and below is that the surround (*i.e.*, average earth reflectance) is usually very close to 18%. Thus this algorithm has no problem with high reflectance targets themselves, but rather it is the large contrast between the bright target and the (average 18%) surround with the subsequent complexity of atmospheric scattering that is difficult to model. The reflectance recovery of very dark targets on a bright reflecting surround such as sand would also yield higher errors (with a double or multiple scattering atmosphere). This difficult problem has been addressed by deriving an estimated atmospheric PSF from the aerosol scattering phase function in this research work.

6. Considerations for Future Work

The total inversion from sensor radiance to ground reflectance algorithm was built to be modular so that new atmospheric parameter methods could be added as they were developed. However, there is still the consideration of the long MODTRAN run times to construct the LUT for use in the total inversion process. All of the MODTRAN runs have been run with an 8 stream multiple scattering option which is 100 times longer than running Isaac's Two Stream multiple scattering. Further research to find suitable spectral anchor points for a specified sensor range should be undertaken. If these anchor points could be specified, then the spectral scale factors could be calculated to convert an Isaac's Two Stream MODTRAN run into a DISORT run. The radiance error this approximation technique would yield is unknown, but investigation appears attractive if two orders of magnitude of run time could be taken off the LUT generation needed for the total inversion algorithm.

From the standpoint of recovering accurate ground reflectances, one of the largest sources of errors appears to be spectral miscalibration or lack of spectral alignment with the MODTRAN atmospheric model. The AVIRIS spectral match appears to be very good (Figure 4.2-4), however the HYDICE spectral error curves do not appear smooth (Figures 4.1-3 and 4.3.1-4). It is easy to see that the error from the spectral mismatch (the “jaggys” in the recovered reflectance curve) is almost a large as the mean level error of the reflectance for many of the HYDICE cases (especially in the Western Rainbow data). Before too much more research effort is devoted to the atmospheric radiative transfer model included in this total inversion algorithm, a focused study and correction needs to be developed for spectral alignment or spectral re-calibration. Once a good spectral correction algorithm adjusts for the spectral misalignment, it will be much easier to analyze the recovered reflectance error in terms of adjusting or adding some parameter(s) in the radiative transfer equation.

It is clear in all the plots on recovered reflectance error that most of the error is located in the blue region which is where scattering due to aerosols are dominant. More work needs to be done with aerosols in composition, relative abundance, and especially the scattering phase function of the particles to recover truth reflectances more accurately in the blue-green spectral region.

Further research could also be done in the generation of the atmospheric point spread weighting function for multiple scattering. Possibly the Henyey-Greenstein function could be added with input for MODTRAN-generated spectral asymmetry parameters which is all that is needed for this simple function. The challenge would be to determine what the kernel size should be to convolve with the first pass reflectance image. Related to this topic is that fact that the 11x11 pixel window size selected for this research work was chosen for convenience of use and moderate coverage. For multiple scattering solutions particularly in the blue-green region of the spectrum, it is very likely the window size for the PSF will have to be optimized.

Another module that could be investigated is incorporating a cloud shape factor in the radiative transfer equation so that inversions to reflectance could be done with imagery where the sky was contaminated with clouds. In this case the radiance coming from the cloud could be modeled as:

$$L_{cloud} = \frac{E_s \cos(\sigma)\tau_1\tau_2\rho_{cloud}}{\pi} \tag{6-1}$$

where E_S is the solar irradiance, σ is the solar zenith angle, τ_1 is the sun-cloud target path, τ_2 is target sensor path and ρ_{cloud} is the average reflectance of the cloud. The cloud shape factor or fraction of the sky covered in clouds would be F and the downwelling radiance component would be scaled by 1-F. If the cloud/sky fraction was not known, possibly some type of iterative technique such as NLLSSF could be utilized to fit the sensor radiance.

These ideas are only a few that are shared in this text. Research into new and faster techniques is taking place as this document is being written. It is hoped that this algorithm will be a steeping stone and a useful tool for imaging scientists in the remote sensing field to use and build on.

7. Appendix

7.1 Appendix A: Computation of Off-Axis Solid Angle of Sensor IFOV Cross-Section

The IFOV (instantaneous field-of-view) of the sensor at some altitude H2 can be thought of as a projected four-sided pyramid with the peak at the sensor and the base being the ground-projected object pixel at surface elevation H1. A source can be defined as the radiance reflecting from a surround pixel at distance y from the object pixel. At some layer altitude h, the source "sees" the altitude projected object as a slice of the IFOV at some angle θ (see Figure 3.5-3). The angle θ is measured at the center of the altitude projected object pixel at height h between the optical axis line at nadir to the line projected from the center of the object pixel at height h to the center of the surround pixel at ground level. The area of the object pixel at height h can be defined as:

$$A_{object} = ((H2-h)\varphi)^2 \qquad \text{(A-1)}$$

where φ is the IFOV in radians. The squared distance from the object pixel center at height h to the center of the surround pixel at altitude H1 can be defined as:

$$r^2 = (h-H1)^2 + y^2 \qquad \text{(A-2)}$$

The easy method for this computation is to first compute the total fraction of the hemisphere that the surround pixel sees of the object pixel at height h. The total area of the hemisphere is:

$$A_{hemi} = 4\pi r^2 \qquad \text{(A-3)}$$

Then the fraction of the hemisphere that the object pixel at height h and angle θ is:

$$F = \frac{A_{\text{object}} \cos(\theta)}{A_{\text{hemi}}} = \frac{((H2 - h)\varphi)^2 \cos(\theta)}{4\pi\left((h - H1)^2 + y^2\right)} \tag{A-4}$$

Since the total steradians in a hemisphere is 4π, then the solid angle subtended by the object pixel at height h and angle θ as viewed by the "source" is:

$$\Omega = \frac{F}{4\pi} = \frac{((H2 - h)\varphi)^2 \cos(\theta)}{\left((h - H1)^2 + y^2\right)} \tag{A-5}$$

which can be simplified further by using an identity:

$$\Omega = \frac{((H2 - h)\varphi)^2 \cos^3(\theta)}{\left((h - H1)^2\right)} \tag{A-6}$$

7.2 Appendix B: Addition to Loop.f of MODTRAN 4.0 Source Code

```
SMSOLL=SMSOLL+SUBINT(INTRVL)*SOLLAY                LOP 0580
 160       CONTINUE                               LOP 0581
          IKP1=IK+1
          ANGLE=0.0
          TEMP_PHASE=PHASEF(1,V,AH1(IKP1),ANGLE,ARH(IKP1))
          GRND_PIX=(H1-H2)*IFOV*0.001
C    Test to see if the phase function value is greater than zero.
C    This algorithm uses only aerosol 1 which goes from 0-2km in
C    altitude.
     IF(TEMP_PHASE.GT.0.0)THEN
       IF((TEMP_PHASE.GT.0.0).AND.(HOLDER.EQ.0))HOLDER=IK
          IF(TX(9).NE.0.0)OPT_UPLYR(IK)=-LOG(TX(9))
          DO 162 J=1, 11
           DO 163 K=1,11
C             PRINT*, V
C           Calculate the distance from the center (target) pixel
C           on the ground to the surround pixel.
            DIST=SQRT((((K-6)*GRND_PIX)*((K-6)*GRND_PIX)+
    1        ((J-6)*GRND_PIX)*((J-6)*GRND_PIX)))
C           Calculate the slant angle from nadir that the surround
C           pixel is located from the layer height object pixel.
            SLANT_ANGLE(IK,J,K)=ATAN(DIST/(AH1(IK)-H2))
C             PRINT*, "DIST=", DIST
C             PRINT*, AH1(IKP1), H1,H2
C             PRINT*, H1-AH1(IK), AH1(IK)-H2
C           Find the solid angle that the "source" surround pixel
C           sees of the layer height object pixel.
            OMEGA_PIX=((H1-AH1(IK))*IFOV*0.001)*
    1            ((H1-AH1(IK))*IFOV*0.001)*
    2            COS(SLANT_ANGLE(IK,J,K))*
    3            COS(SLANT_ANGLE(IK,J,K))*
    4            COS(SLANT_ANGLE(IK,J,K))/((AH1(IK)-H2)*
    5            (AH1(IK)-H2))
C             PRINT*, "OMEGA=",OMEGA_PIX
C           Calculate the phase function value for the radiance
C           vector at the layer height (AH1(IK)-H2) coming from
C           ground grid position J, K.
            TEMP_PHASE=PHASEF(1,V,AH1(IKP1),SLANT_ANGLE(IK,J,K)*
    1                   DEG,ARH(IKP1))
C           Multiply the phase function value by the solid angle
C           subtended by the layer height object pixel.
            SCAT_FUNC(IK,J,K)=TEMP_PHASE*OMEGA_PIX
C             PRINT*, "PHASE FUNC=",SCAT_FUNC(IK,J,K)
            IF((J.EQ.1).AND.(K.EQ.1))THEN
C             PRINT*, AH1(IKP1), TEMP_PHASE, SCAT_FUNC(IK,J,K)
C             PRINT*, OMEGA_PIX
```

```
                ENDIF
  163           CONTINUE
  162          CONTINUE
C              PRINT*, " "
      ENDIF
       IF(IK.EQ.IKMAX)THEN
C       Loop to begin summing the unitless scattering phase function
C       values over all the layer heights for the entire 11x11 grid.
         DO 164 LAYER_INCR=HOLDER, IKMAX
          DO 165 J=1, 11
           DO 166 K=1, 11
            IF(TX(9).NE.0.0)THEN
C             Calculate the total transmittance from the surround pixel
C             at grid position J, K to the layer height object pixel to
C             the sensor height.  This is only the ground-to-sensor
C             transmission; the transmission from sun to ground is
C             assumed to be the same for all the ground pixels on the
C             grid.
             TEMP_TAU=EXP(-((OPT_UPLYR(IKMAX)-OPT_UPLYR(LAYER_INCR))
     1                  /COS(SLANT_ANGLE(LAYER_INCR,J,K))+
     2                  OPT_UPLYR(LAYER_INCR)))
            ENDIF
            IF(TX(9).EQ.0.0)TEMP_TAU=0.0
C             Multiply the phase by the total transmission term.
             SUM_PHASE_FUNC(J,K)=SUM_PHASE_FUNC(J,K)+
     1                      SCAT_FUNC(LAYER_INCR,J,K)*TEMP_TAU
             IF((J.EQ.1).AND.(K.EQ.1))THEN
C             PRINT*, "SUM PHASE"
C             PRINT*, SLANT_ANGLE(LAYER_INCR,J,K)*DEG
C             PRINT*, AH1(LAYER_INCR+1), OPT_UPLYR(IKMAX)
C             PRINT*, OPT_UPLYR(LAYER_INCR), TEMP_TAU,
C    1                SCAT_FUNC(LAYER_INCR,J,K)
C             PRINT*, SUM_PHASE_FUNC(J,K)
C             PRINT*," "
             ENDIF
  166        CONTINUE
  165       CONTINUE
C           PRINT*," "
  164      CONTINUE
       ENDIF
C      PRINT*, " "
              IF(NOPRNT.LE.-1)THEN                                LOP 0582
```

7.3 Appendix C: Analysis of the HYDICE Run 29 NLLSSF 2nd Pass Reflectance Inversion Using An Isotropic Atmospheric PSF.

Much time and effort has been spent attempting to model the atmospheric PSF to more rigorously implement the radiance contribution at the sensor due to the adjacency effect. This brief addendum is added to answer the question of: Why go through all the bother of deriving and extracting the scattering due to the aerosol phase function when possibly a simple averaging kernel might do just as well (or better)? Figure 7.3-1 shows the results in the form of recovered reflectance error in the manner of Section 4.

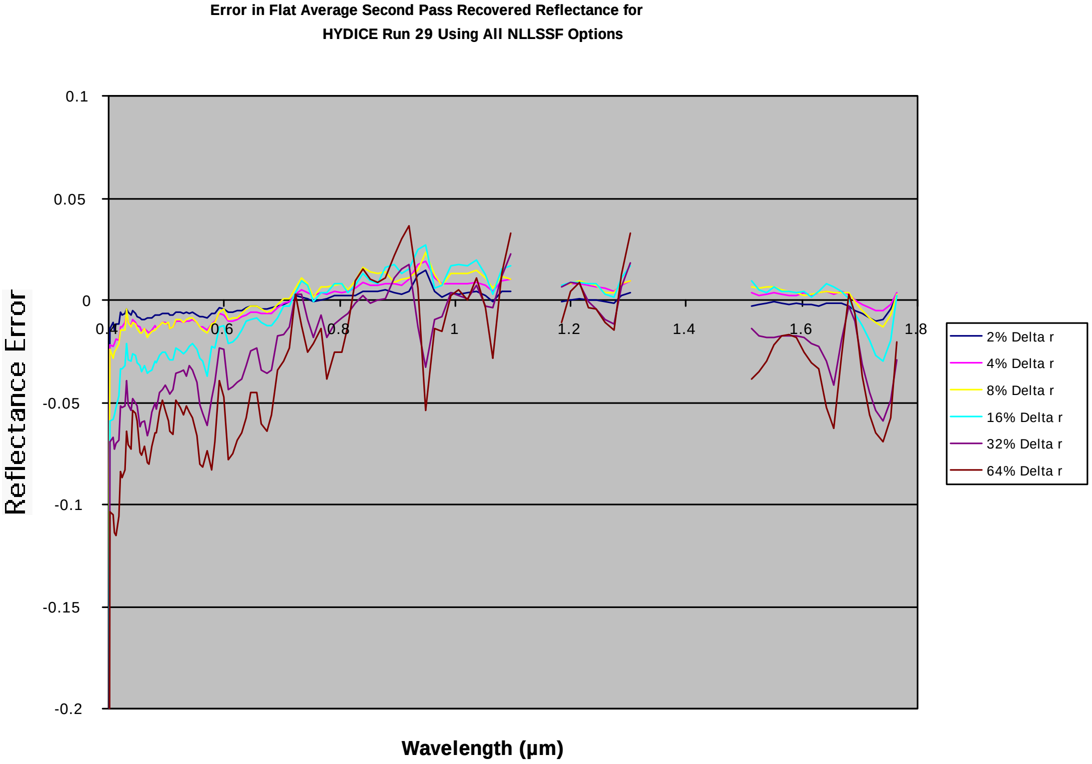

Figure 7.3-1. 2nd pass recovered reflectance error for HYDICE Run 29 using NLLSSF for all options and an isotropic averaging kernel for the PSF.

When these results are compared directly with Figure 4.1-7, it can be seen that the simple kernel actually has a bit less error in the far blue region than when using the phase function-derived kernel. The spectral reflectance errors are approximately equal at around 0.450µm and from there to about 0.8µm the error for the simple kernel is progressively the poorer performer. Then , an interesting thing happens at around 0.825µm out to about 1.3µm. The recovered reflectance error becomes much less for the simple averaging kernel. The matches to the truth reflectance for the 64% gray panel are clearly seen in Figure 7.3-2 with the "flat_avg" curve being the one derived from the isotropic PSF.

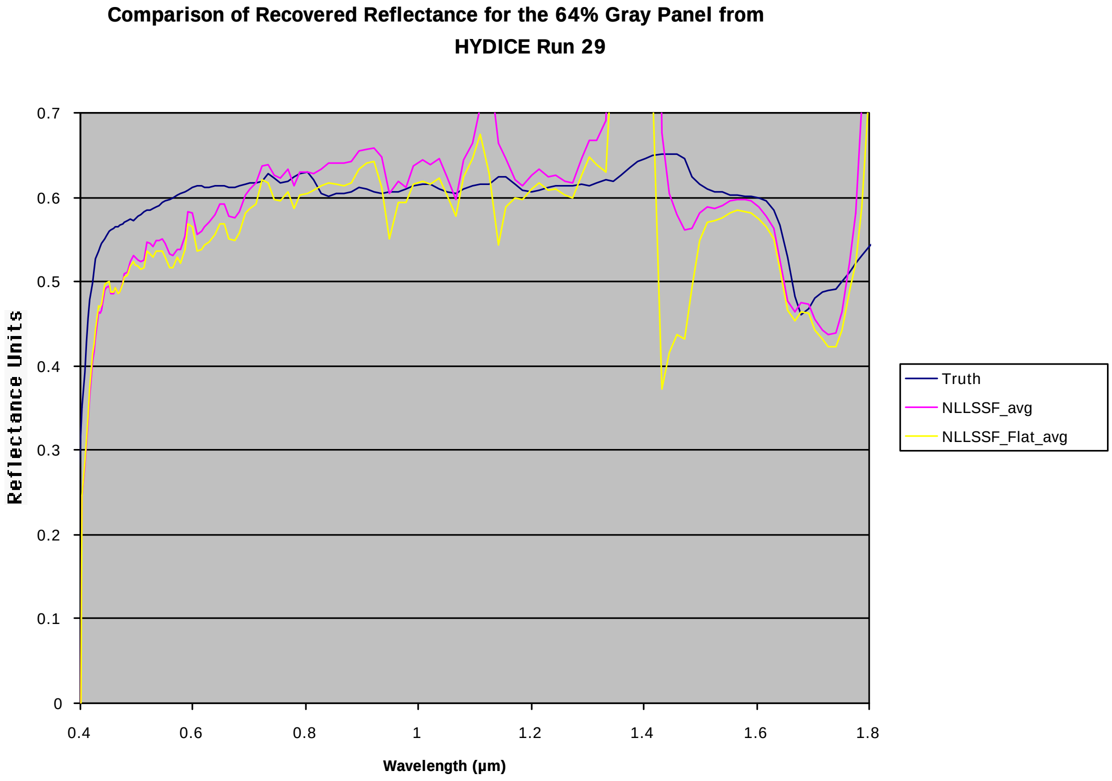

Figure 7.3-2. The 64% gray panel recovered reflectances from the 2nd pass NLLSSF with the phase-function PSF and the flat averaging PSF.

It is this researcher's opinion that there are two different things happening at different places in the spectrum with the effectiveness of the radiative transfer equation process. First, in the region from 0.4-0.45µm it is quite obvious from looking at the corresponding optical depths in MODTRAN tape7 from this scene that double and multiple scattering is occurring (Van de Hulst, 1957). The PSF that is derived in this research work models only a single scattering event from the surround pixel to the sensor. As explained at the end of Section 3.5, the PSF for multiple scattering is much broader and isotropic than the single scattering models. Thus, in this trial, the isotropic averaging kernel did a better job modeling the multiple scattering events below 0.45μm. But, as the spectral optical depths decreased with increasing wavelength and a single scattering effect became dominant, the phase function derived PSF was a better performer. This result would be expected.

But, explaining the better performance in reflectance recovery from 0.825-1.3μm is requires some thought into another process. In Figure 3.5-6, it can clearly be seen that the magnitude of the resolved environmental radiance is very small above 0.8μm. It is certainly not of the order to make a noticeable difference in the recovery of reflectance. However, refer to Equation 2-39. The ρ_{avg} term was not only used in the environmental/adjacency radiance parameter. It was substituted for ρ (the ground target reflectance) in the trapping effect radiance series as well. Here is where the answer may lie.

In theory, the atmospheric PSF when applied to the trapping effect is very broad. The series in the denominator of equation 2-37 and 2-39 models the multiple reflections of the "trapped" photons from the surround and the target until they head in the nadir direction toward the sensor. In a small 11x11 pixel window of the scene it may very well appear that this particular PSF appears almost isotropic. This may explain why the isotropic averaging PSF worked so well in this region of the spectrum; it more correctly modeled the trapping effect PSF than the one derived from the aerosol phase function. Thus, from this one sample image, the conclusion could be drawn that a ρ_{avg} derived from a different PSF must be used in the trapping effect series to correctly model this process in the radiative transfer equation. Given these preliminary results with this well characterized hyperspectral image, a further investigation into the trapping effect radiance PSF certainly is in order.

7.4 Appendix D: The User's Manual for the Atmospheric Correction Algorithm "Total Inversion"

User's Manual for
Total Inversion

A Modular Algorithm for Retrieving Ground Reflectance from Calibrated Sensor Radiance

By Lee C. Sanders and Rolando Raqueño
August 11, 1999

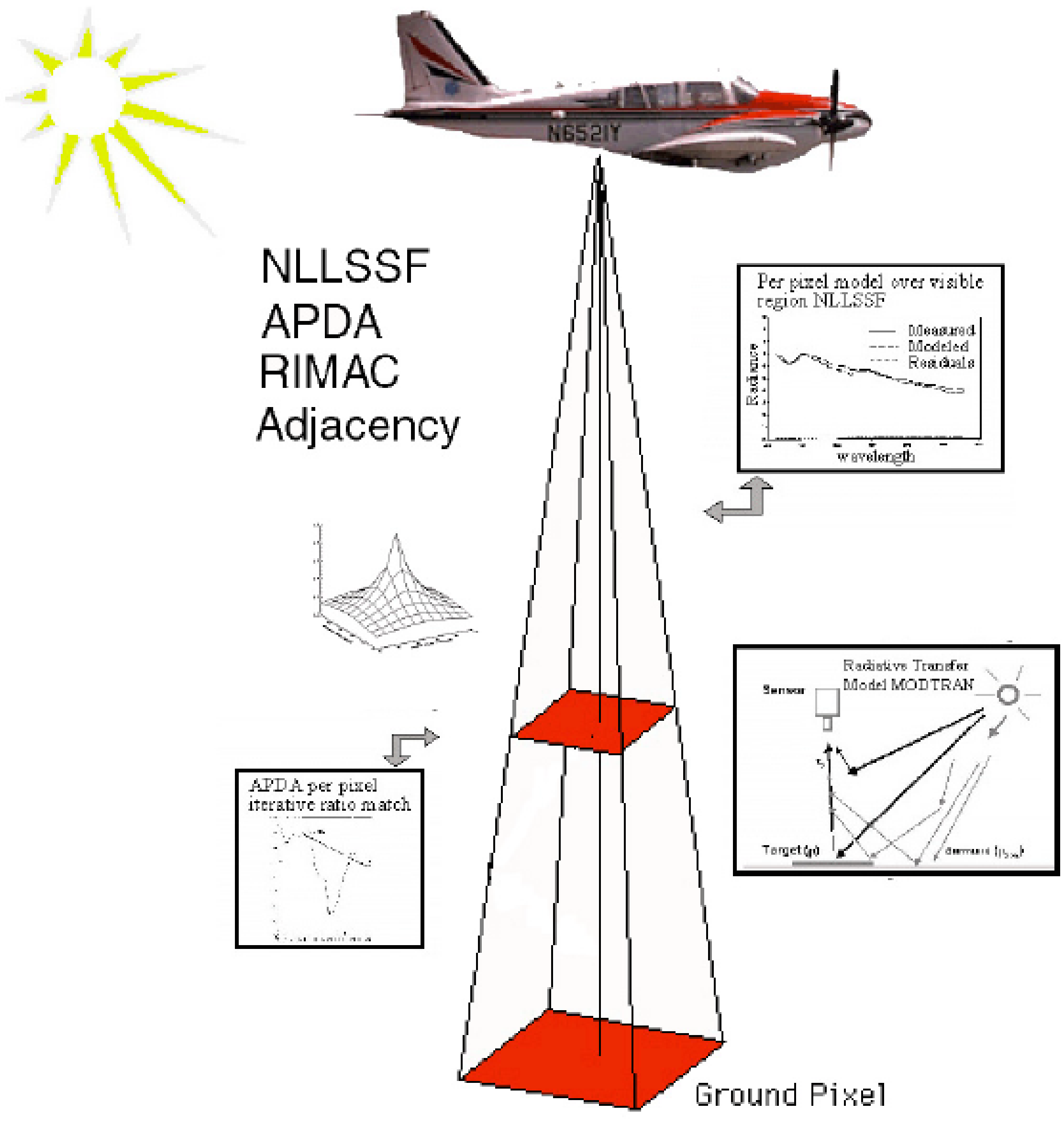

TABLE OF CONTENTS

1. Introduction

Total inversion is a modular program designed to be used on radiometrically calibrated hyperspectral images in order to invert the sensor radiance to estimated ground reflectance. Since the algorithm has components that are in IDL, Fortran, C++, non-interactive ENVI calls, and Unix awk scripts, it is highly recommended that the user set up this algorithm on a system running Unix with the appropriate compilers and ENVI installed. No guarantees are forwarded for this algorithm as it now stands to be installed and used in a Windows, DOS, or Macintosh OS. It should be noted that it is assumed that the user already has MODTRAN 4.0 revision 3 installed on their system; it is necessary since the environment variables for the MODTRAN databases need to be set for the user's system.

This algorithm has three subsections that are optionally selected to solve for the parameters of surface-pressure depth (elevation given a pressure profile in radiosonde), aerosol model-dependent visibility, and columnar water vapor. The package also includes the Look-Up Table (LUT) generator for creating the radiometric database needed by Total Inversion. The Total Inversion algorithm has three different selections for the radiative transfer equation which depend either the appropriateness of the model (single or multiple scattering) or whether the user is in the first pass or second pass of the algorithm. The second pass of the algorithm is designed to use the weighted average reflectance image to scale the adjacency and trapping effect radiance.

The first pass of the algorithm produces for output a reflectance cube of the same dimensions as the input hyperspectral image, an average reflectance image derived from the 11x11 convolved input image, an image information cube that contains the solved parameters for each pixel (defined in the header file), a scaled water vapor tiff image, and a scaled surface elevation tiff image. After running the routine to generate the atmospheric PSF, the average reflectance image from the first pass is over-written with the PSF-weighted average reflectance image for input into the second pass. The second pass algorithm produces a new reflectance cube and new image info cube.

2. Atmospheric MODTRAN LUT Generation Steps

Modified:
Fri Jun 4 08:56:02 EDT 1999

The following document describes the procedures to create an MODTRAN atmospheric lookup table (LUT) for use as input into the APDA, GREEN. and RIMAC methods implemented by Lee Sanders. The current version supported for this implementation is MODTRAN 4.0 revision 3 for UNIX workstations (OSF alpha's, Sun sparcs, and LINUX alphas).

Because these lookup tables can take over 1600 MODTRAN runs to create,
the procedures outlined here have been developed to ease the logistics of distributing these MODTRAN runs over the different CPU's in the center. You will have the flexibility of targeting some or all of the CPU's at your disposal (you should contact the appropriate person if you plan to use CPU's under the ownership of labs outside of DIRS). This distribution of processes insures a timely generation of LUT data and also allows portions of the LUT cases to be processed should an error be encountered in some of the runs or some of the CPU's become

unavailable. Tools have also been developed to check the validity of the MODTRAN runs
and also monitor the number of MODTRAN cases that have been completed.

Once the runs have been completed, an assembly process is applied to the finished lookup table. This will generate a single file that contains all the necessary data extracted from each of the MODTRAN runs.

The following sections will describe in detail each of the steps that are necessary to produce a final LUT file. These sections will cover the following topics

2.1 Creating the MODTRAN Lookup Table Tree (LUTT).
2.2. Distributing, Monitoring, Restarting, and Verifying the MODTRAN LUTT
2.3. Assembling and Applying a Sensor Response the Final LUT file

N.B. Any scripts that are referenced in this document will reside in /dirs/common/bin. Please make sure that this is in your path and that it
comes before ~rvrpci/bin (this will insure that you are using the most stable version of the scripts and not running some experimental version that we may be working with).

2.1 Create a MODTRAN LUT tree

The process involves creating a directory tree for a given baseline atmospheric case. This is accomplished by invoking the shell script called "make_modtran_lut_tree.csh" which require two files as part of its input arguments.

The first part is a baseline MODTRAN card deck and the second part is a configuration file. The usage is shown below

```
        % create_modtran_lut_tree.csh baseline_case baseline.cdk \
                baseline.config
```

The first argument, "baseline_case", is the root name of the atmospheric case which will be created (this directory should not exist yet). This is a directory that will contain subdirectories of the different MODTRAN cases.

The second argument is a standard MODTRAN input card deck "baseline.cdk" which will be used as the starting point of all the subsequent cases defined by the third argument "baseline.config". Before running "create_modtran_lut_tree.csh" it would be wise to check if this MODTRAN carddeck will run on all the architectures that you plan to use. There are some cases in which the code will run to completion on some architectures (most likely OSF alpha's) and abort on others (Linux-alpha's and SUN sparc's). While this will not screen out all cases, it will give an initial indication of whether or not your carddeck is valid.

N.B. A common error that has been encountered by users is forgetting to set the multiple scattering flag (5th field of the first card) to 1 to activate multiple scattering. If you do not do this, the file spheralb.dat will not be generated and no spherical albedo data will be available.

This third file configures how specific parameters in the card decks are modified and how the directory structure of the tree will be arranged.

The following shows how "baseline.config" might look like

```
############################################################
#
        #Minimum Aerosol Value
        #Maximum Aerosol Value
        #Aerosol Value Increment
        10.0
        20.0
        10.0

        #Mininum Elevation Value
        #Maximum Elevation Value
        #Elevation Value Increment
        0.315 1.215 0.1

        #Minimum Water Vapor Value
        0.05
        #Maximum Water Vapor Value
        2.25
        #Water Vapor Value Increment
        0.2

        #Minimum Albedo Value
        #Maximum Albedo Value
        0.0 1.0
        #Albedo Value Increment
        1.0
        #######################################################
######
```

The entry of the values is free format with leading "#" for comments. The structure of the tree is currently setup such that the the subdirectory names at the different depths reflect the parameters listed below

- aerosols
- elevations
- water_vapor
- albedo

Each of the above subdirectories will contain children directories which have numeric names reflecting the appropriate parameter value for that case. The range of values and number of directories are determined by the minimum, maximum, and increment values specified in the configuration file ("baseline.config").

As this directory tree is created, the different versions of "baseline.cdk" are modified and placed in the appropriate directory. Makefiles are also created at each level to allow the MODTRAN runs to be started at any level of the tree.

The following is an example run and output of "create_modtran_lut_tree.csh"

```
% create_modtran_lut_tree.csh boreas_mult boreas_mult.cdk
boreas_mult.conf

Aerosol directories are [km visibility] 10.0 20.0 30.0 40.0 50.0 60.0 70.0
```

```
Elevation directories are [km] 0.315 0.415 0.515 0.615 0.715 0.815
0.915 1.015 1.115 1.215

Water vapor directories are [scale factor] 0.05 0.25 0.45 0.65 0.85 1.05
1.25 1.45 1.65 1.85 2.05 2.25
Processing [aerosol, elevation, water vapor] directory [10.0, 0.315, 0.05]
Processing [aerosol, elevation, water vapor] directory [10.0, 0.315, 0.25]
Processing [aerosol, elevation, water vapor] directory [10.0, 0.315, 0.45]
Processing [aerosol, elevation, water vapor] directory [10.0, 0.315, 0.65]
Processing [aerosol, elevation, water vapor] directory [10.0, 0.315, 0.85]
Processing [aerosol, elevation, water vapor] directory [10.0, 0.315, 1.05]
Processing [aerosol, elevation, water vapor] directory [10.0, 0.315, 1.25]
Processing [aerosol, elevation, water vapor] directory [10.0, 0.315, 1.45]
Processing [aerosol, elevation, water vapor] directory [10.0, 0.315, 1.65]
Processing [aerosol, elevation, water vapor] directory [10.0, 0.315, 1.85]
Processing [aerosol, elevation, water vapor] directory [10.0, 0.315, 2.05]
Processing [aerosol, elevation, water vapor] directory [10.0, 0.315, 2.25]


Water vapor directories are [scale factor] 0.05 0.25 0.45 0.65 0.85 1.05
1.25 1.45 1.65 1.85 2.05 2.25
Processing [aerosol, elevation, water vapor] directory [10.0, 0.415, 0.05]
Processing [aerosol, elevation, water vapor] directory [10.0, 0.415, 0.25]
Processing [aerosol, elevation, water vapor] directory [10.0, 0.415, 0.45]
Processing [aerosol, elevation, water vapor] directory [10.0, 0.415, 0.65]
.
.
.
```

```
Water vapor directories are [scale factor] 0.05 0.25 0.45 0.65 0.85 1.05
1.25 1.45 1.65 1.85 2.05 2.25
Processing [aerosol, elevation, water vapor] directory [70.0, 1.215, 0.05]
Processing [aerosol, elevation, water vapor] directory [70.0, 1.215, 0.25]
Processing [aerosol, elevation, water vapor] directory [70.0, 1.215, 0.45]
Processing [aerosol, elevation, water vapor] directory [70.0, 1.215, 0.65]
Processing [aerosol, elevation, water vapor] directory [70.0, 1.215, 0.85]
Processing [aerosol, elevation, water vapor] directory [70.0, 1.215, 1.05]
Processing [aerosol, elevation, water vapor] directory [70.0, 1.215, 1.25]
Processing [aerosol, elevation, water vapor] directory [70.0, 1.215, 1.45]
Processing [aerosol, elevation, water vapor] directory [70.0, 1.215, 1.65]
Processing [aerosol, elevation, water vapor] directory [70.0, 1.215, 1.85]
Processing [aerosol, elevation, water vapor] directory [70.0, 1.215, 2.05]
Processing [aerosol, elevation, water vapor] directory [70.0, 1.215, 2.25]
```

N.B. Because the runs may take several days, it is sometimes wise to create a MODTRAN LUT tree (LUTT) case that has a "coarse" increment for the various parameters in the configuration file and an input carddeck that has a very coarse sampling of the spectral range. By doing this, you can make a quick validation to establish that the ranges that you are trying to use are reasonable and will run to completion. This is especially helpful if this is your first time running a LUTT because you can quickly run through all the steps without having to wait for a full LUT.

Once this process is complete, the different cases can now be run as detailed in Section 2.2.

2.2 Distributing, Monitoring, Restarting, and Verifying the MODTRAN LUT

Now that you have the "tree" created, you will need to start the different cpu's processing this tree. Before you can do this, you will need to identify the cpu's that you want to use and create what is known as an ".rhosts" file in your home directory (cf. man rhosts). An example ".rhosts" file might look like the following.

```
rocky.whatsomattau.edu your_username
bullwinkle.whatsomattau.edu your_username
.
.
.
natasha.whatsomattau.edu your_username
boris.whatomattau.edu your_username
```

This file essentially allows you to "rsh" commands on other machines. In other words, you can execute commands on another CPU without logging in with a password. If you have this file set correctly, you can test it by giving a command similar to the one below.

```
% rsh rocky.whatsomattau.edu w
```

This will execute the "w" command on the CPU "rocky.whatsomattau.edu"

You will only need to setup this file once, but you will need to update it with new CPU names if you find other CPU's that you want to be able to use.

Checking for MODTRAN Availability on different CPU's:

Because the state of these machines may not always be known, it would be prudent to find out if MODTRAN is accessible in the form of the command "modtran4.bat". This can be done by executing the command called "check_modtran_availability.csh"

The usage of this command is as follows.

```
% check_modtran_availability.csh cpu_list
```

The file, "cpu_list", will contain the candidate CPU's that you want to utilize. As an example, you can group the fast CPU's into a file called "fast_cpus" such as the one below. (A file called all_cpus is located in /dirs/common/bin and contains a list, probably outdated, of some of the CPU's in the Center).

```
titan
saturn
exeter
defiant
reliant
excelsior
```

```
cdom
haise
crippen
grissom
lovell
```

It is customary to put this file inside the root of the MODTRAN tree directory that will be processed just to keep things in a centralized location.

Now let us assume that the computer "haise" is not working properly either because it is offline or the disk containing "modtran4.bat" is not mounted properly.

When you execute this command using the CPU list "fast_cpus"

```
% check_modtran_availability.csh fast_cpus
```

You will get a file called "fast_cpus.good" and "fast_cpus.bad". The file "fast_cpus.good" will contain the CPU list.

```
titan
saturn
exeter
defiant
reliant
excelsior
cdom
crippen
```

```
        grissom
        lovell
```

The other file, "fast_cpus.bad" will contain the CPU list

```
        haise
```

You now have a list of valid CPU's that should, in theory, be able to process
your MODTRAN runs. As for the CPU's in "fast_cpus.bad", report it to Bob K. or Sue Michel so that they can make modtran4.bat accessible to you so that you can utilize these additional CPU's. It may also be prudent to see
if a particular CPU is heavily loaded with jobs. For this, you can use the monitor_loads.csh command which will give you the following output.

```
        % monitor_loads.csh

titan : 14:39  up 4 days,  6:32,  12 users,  load average: 1.43, 1.28, 1.23
saturn : 14:39  up 4 days,  6:25,  8 users,  load average: 0.37, 0.15, 0.13
exeter : 14:39  up 4 days,  6:04,  8 users,  load average: 0.00, 0.00, 0.00
defiant : 14:39  up 4 days,  6:04,  1 user,  load average: 0.00, 0.00, 0.00
reliant : 14:39  up 4 days,  6:04,  2 users,  load average: 0.02, 0.18, 0.18
excelsior : 14:39  up 4 days,  6:04,  8 users,  load average: 0.32, 0.35, 0.39
pile1 :   2:31pm  up  5:47,  0 users,  load average: 0.00, 0.00, 0.00
pile2 :   2:31pm  up  5:46,  0 users,  load average: 0.08, 0.02, 0.01
pile3 :   2:32pm  up  2:36,  0 users,  load average: 0.00, 0.00, 0.00
```

```
cdom :  2:39pm  up 4 day(s), 18:08,  1 user,  load average: 0.66, 0.80,
0.79
hubble :  2:36pm  up 4 day(s),  5:42,  0 users,  load average: 0.21, 0.15,
0.16
corona :  2:37pm  up 4 day(s),  5:42,  0 users,  load average: 0.24, 0.16,
0.16
keyhole :  2:38pm  up 4 day(s),  5:42,  0 users,  load average: 0.08, 0.02,
0.02
narwhal :  2:41pm  up  5:48,  0 users,  load average: 0.10, 0.03, 0.02
lacrosse : lacrosse.cis.rit.edu: Connection timed out
haise :  2:40pm  up 4 day(s),  6:07,  0 users,  load average: 0.11, 0.09,
0.09
crippen :  2:39pm  up 4 day(s),  6:06,  2 users,  load average: 0.18, 0.09,
0.09
lovell :  2:49pm  up 4 day(s),  6:07,  0 users,  load average: 0.02, 0.01,
0.01
grissom :  2:41pm  up 4 day(s),  6:06,  1 user,  load average: 2.86, 2.86,
3.02
carpenter :  2:38pm  up 4 day(s),  6:03,  0 users,  load average: 0.08,
0.02, 0.02
aldrin :  2:40pm  up 4 day(s),  6:05,  0 users,  load average: 0.09, 0.02,
0.02
young :  2:41pm  up 4 day(s),  6:05,  0 users,  load average: 0.11, 0.03,
0.02
cooper :  2:42pm  up 4 day(s),  6:05,  0 users,  load average: 0.10, 0.02,
0.02
ride :  2:44pm  up 4 day(s),  6:03,  0 users,  load average: 0.08, 0.02,
0.02
```

```
schirra :  2:45pm  up 4 day(s),  6:03,  0 users,  load average: 0.09, 0.02,
0.02
swigert :  2:56pm  up 4 day(s),  6:04,  0 users,  load average: 0.06, 0.02,
0.02
shepard :  2:56pm  up 4 day(s),  6:06,  0 users,  load average: 0.06,
0.02, 0.02
slayton :  2:58pm  up 4 day(s),  6:05,  0 users,  load average: 0.06, 0.02,
0.02
kepler :  2:40pm  up 4 day(s),  6:05,  2 users,  load average: 0.00, 0.05,
0.29
white :  2:39pm  up  2:19,  0 users,  load average: 0.05, 0.02, 0.02
conrad :  2:45pm  up  2:19,  0 users,  load average: 0.08, 0.02, 0.02
```

Depending on the load averages (the numbers represent of jobs in the run queue for the past 5, 30, and 60 seconds) you may want to delete a CPU from the list if it already has a job running. You can start the jobs specifically for a given CPU later when the process load goes down.

We can now start the MODTRAN runs by giving the following command.

The command that you will be using initially is called "distribute_modtran_runs.csh"

The usage for this command is the following

```
    % distribute_modtran_runs.csh cpu_list_file absolute_path_to_tree
```

The cpu_list_file in this case would be the "fast_cpus.good" that has been screened and generated by "check_modtran_availability.csh"

Now you want to choose a slow CPU that you will not be using for MODTRAN processing and designate this as your MASTER CPU. It should
not be in either your "good" or "bad" cpu list. It's role will be
to spawn the different MODTRAN processes so you don't want it to do any other processing other than just spawning. You can then execute the following command

The argument absolute_path_to_tree would be something like
/dirs/home/rvrpci/boreas/boreas_mult

From any machine, you should now be able to give the command that looks like something below.

```
% distribute_modtran_runs.csh all_cpus.good
/dirs/home/rvrpci/boreas/boreas_mult &
[1] 16897
% Processing titan
[1] 16787
[1] 16813
[1]  + Done                start_modtran_runs.csh titan
/dirs/home/rvrpci/boreas/boreas_mult
Processing saturn
[1] 19777
[1] 16566
```

.
.
.

Note that there will be a slight delay between each of the CPU's. This delay is intentional in order to keep too many processes from being created at one time.

Once the runs have been started, you will want to monitor the progress of the runs as well as the loads on the CPUS. There are two commands that you will be able to use for this.

The first command is "verify_modtran_runs.csh". You should run this in the root directory of the LUT because this will generate a file called "verify_modtan_runs.log"which looks like the file below

```
Tue Jun  1 08:52:29 EDT 1999
**** 1680 MODTRAN runs are currently running or have been succesfully
completed ****
**** out of 1680 runs ****
++++++++++++++++++++++++++++++++++++++++++++++++++++++++++++
++++++
++++++++++++++++++++++++++++++++++++++++++++++++++++++++++++
++++++
```

```
++++++++++++++++++++++++++++++++++++++++++++++++++++++++++++
++++++
        .
        .
        .
++++++++++++++++++++++++++++++++++++++++++++++++++++++++++++
++++++
++++++++++++++++++++++++++++++++++++++++++++++++++++++++++++
++++++
++++++++++++++++++++++++++++++++++++++++++++++++++++++++++++
++++++
STARTED on grissom: Sun May 30 23:50:24 EDT 1999 -------------------- :
./aerosols/50.0/elevations/1.215/water_vapor/0.25/albedo/1.0/proces
s.log
++++++++++++++++++++++++++++++++++++++++++++++++++++++++++++
++++++
STARTED on corona.cis.rit.edu: Tue Jun 1 03:17:38 EDT 1999 ------------
------ :
./aerosols/70.0/elevations/1.215/water_vapor/0.25/albedo/1.0/proces
s.log
+++++++++++++++
STARTED on lacrosse.cis.rit.edu: Tue Jun 1 04:17:36 EDT 1999 ----------
-------:
./aerosols/70.0/elevations/1.215/water_vapor/1.85/albedo/1.0/proces
s.log
++++
```

This log will tell you how many processes have completed or are currently running. The CPU name and starting times of the processes currently running are also listed. In some cases, the process may have actually terminated. You can determine this by looking at the start day and see if it makes sense. If the start date is more than a day old, then the process probably terminated prematurely. You can also use "monitor_loads.csh" to check if there is anything running on the specific CPU's. If the loads are low, then the MODTRAN process probably aborted.

There are several ways of restarting these aborted processes. You can restart it by logging into a fast CPU that is not heavily loaded and going directly to that directory (e.g. ./aerosols/50.0/elevations/1.215/water_vapor/0.25/albedo/1.0/)

and giving the command

```
% gmake clean
```

command followed by a

```
% gmake &
```

or if you know that all the processes in the "verify_modtran_runs.log" are all stalled or dead, you can give the following command.

```
% clean_stalled_cases.csh
```

This command will go to all the listed directories and "clean up" the files so that they can be restarted again. Since you may only have

a few cases left to rerun, you may want to send them to a few
fast CPU's using the following command

```
        % start_modtran_runs.csh titan
/dirs/home/rvrpci/boreas/boreas_mult
```

The usage is similar to distribute_modtran_runs.csh except the first argument is an actual CPU name instead of a file containing CPU names. You can also conceivably give an absolute path to the specific directory of the case (e.g. /dirs/home/rvrpci/boreas/boreas_mult/aerosols/50.0/elevations/1.215/water_vapor/0.25/albedo/1.0) or you can give the absolute path to the tree root directory. In the latter case, the process will traverse the tree until it finds the unprocessed cases.

You will know that you have a fully processed MODTRAN tree when you have run "verify_modtran_runs.csh" and have a log file that contains
all "+"'s , i.e.,

```
Tue Jun  1 12:52:29 EDT 1999
**** 1680 MODTRAN runs are currently running or have been succesfully
completed ****
**** out of 1680 runs ****
++++++++++++++++++++++++++++++++++++++++++++++++++++++++++++
++++++
++++++++++++++++++++++++++++++++++++++++++++++++++++++++++++
++++++
++++++++++++++++++++++++++++++++++++++++++++++++++++++++++++
++++++
```

```
          .
          .
          .
++++++++++++++++++++++++++++++++++++++++++++++++++++++++++++++++++
++++++
++++++++++++++++++++++++++++++++++++++++++++++++++++++++++++++++++
++++++
++++++++++++++++++++++++++++++++++++++++++++++++++++++++++++++++++
++++++
++++++++++++++++++++++++++++++++++++++++++++++++++++++++++++++++++
++++++
++++++++++++++++++++++++++++++++++++++++++++++++++++++++++++++++++
++++++
++++++++++++++++++++++++++++++++++++++++++++++++++++++++++++++++++
++++++
++++++++++++++++++++++++++++++++++++++++++++++++++++++++++++++++++
++++++
++++++++++++++++++++++++++++++++++++++++++++++++++++++++++++++++++
++++++
++++++++++++++++++++++++++++++++++++++++++++++++++++++++++++++++++
++++++
```

You can now proceed to the next step which is the assembly of the final lookup table from the results of all these MODTRAN runs.

2.3 Apply the appropriate sensor response to create the final APDA/GREEN LUT

Once all the data is in place in the modtran tree directories, the final sensor specific lookup table can now be generated.

In order for this to be generated, a sensor response file need to be created and copied into the MODTRAN case root directory.

Below is a sample head and tail of an AVIRIS response file giving the number of spectral points followed by the band centers and FWHM values (in [nm])at each spectral point.

```
224
373.4 9.9
382.94 9.82
392.51 9.76
...
2483.6 11.78
2493.43 11.75
2503.26 11.72
```

The command to start this process given a sensor response called "baseline.rsp" (which should also be placed in the directory "baseline_case") is the following

```
% assemble_lut.csh baseline_case baseline.rsp
```

This will create a file called "baseline.rsp.lut" in the directory "baseline_case"

This process will take a while because it has to convolve the file "spheralb.dat" into a file called "spherical_albedo.dat". The process is currently serial and has not been parallelized.

This will be one of the improvements that needs to be incorporated in future upgrades.

To check if the LUT is valid, you should run the command "verify_assemble_lut.csh" which has the following usage.

```
        % verify_assemble_lut.csh boreas_mult.rsp.lut
```

If the script completes without any errors such as the output below, the you should now have a lookup table that is compatible with the APDA and GREEN atmospheric corrections methods.

```
% verify_assemble_lut.csh hydice_cr15m50.rsp.lut
a = read_aerosol_elevation_water_vapor_data( 'hydice_cr15m50.rsp.lut' )
IDL Version 5.0 (sunos sparc). Research Systems, Inc.
Installation number: 13722-0.
Licensed for use by: RIT Center for Imaging Science

For basic information, enter "IDLInfo" at the IDL> prompt.

% Compiled module:
READ_AEROSOL_ELEVATION_WATER_VAPOR_DATA.
% Compiled module: STRIP_OUT_COMMENTS.
Number of Visibibility Entries =       7.00000
Number of Elevation Entries =       10.0000
Number of Water Vapor Entries =       12.0000
Number of Spectral Points =       209.000
Fri Jun  4 09:43:50 EDT 1999
```

N.B. A log of this output is also saved in the file called
"verify_assemble_lut.log" in your current working directory
(just a reminder, unless specified, you should be working inside
the top of your modtran lut tree).

The rest of this documents contains miscellaneous notes that you may need to refer to in unusual cases. For the most part, however, you will only need to follow the steps presented to this point.
In the event that you find any anomalous behaviors, please contact mailto:rolando@cis.rit.edu and notify him of the specific conditions that are causing the process to fail.

MISCELLANEOUS NOTES:
Dead Process Cases:

On occasion, you will inadvertently put the master CPU that spawns all the processes in your CPU list. When you do this, what you will find is that you will run out of process slots when it tries to process the different cases. When you do a "verify_modtran_runs.csh" and look at the file "verify_modtran_runs.log" you will show cases that look like the following.

```
.
.
.

:
```

```
./aerosols/60.0/elevations/0.615/water_vapor/1.45/albedo/0.0/process.log

:
./aerosols/60.0/elevations/0.615/water_vapor/1.45/albedo/1.0/process.log

.
.
.
```

You would usually see a hostname and start date in these cases. But because the CPU has maxed out the user process slots, it cannot generate the appropriate information. Unfortunately, these cases get tagged as if they executed to completion. So, in order to restore them back to an uncompleted state, you can use the "clean_dead_process_cases.csh"

This command will go to all these directories and restore them back for other CPU's to process. In general, you should not have to use this command as long as you make sure that you have one CPU as your master CPU.

Utility routines:

distribute_modtran_runs.csh
start_modtran_runs.csh
verify_modtran_runs.csh
monitor_loads.csh

```
  clean_stalled_cases.csh
```

Utility routines to be implemented:

```
  check_carddeck.csh     # This routine will run a single carddeck
                         # case on an alpha (titan), sun (crippen),
                         # and a linux-alpha (pile1)

  count_modtran_cases.csh # This routine will look for "makefiles"
                         # to get a tally of the number of modtran
                         # runs that need to be executed in a
                         # particular tree.
```

According to Lee S. the units of radiance coming out of the tape 7 files generated by modtran35 is in Watts/(cm^2 sr cm^-1)

3.0 Setting Up for Running Total Inversion

There are a number of objects the user must have in a working directory in order to run Total_Inversion. Some are required and others are optional depending on what combination of parameter estimation techniques are selected. Be sure to check the source code package to see if there are sample files already included that can be edited for the user's purpose. The following is a list of objects required for the total_inversion.pro command line (these are all the files or options that prompt the user when the program "mk_total_inv_cddk.pro" is run), files that the program will look for, and a detailed description of the program's output(s). If all the required images and file are checked off, the Total Inversion algorithm can be initiated.

3.1 Required Command Line Inputs

Check over the list in this section and then run the program "mk_total_inv_cddk.pro" in order to build a carddeck to run Total Inversion.

O2_image_file -	An PxMxN hyperspectral image in integer (2-byte) data format and band-interleaved-by-pixel (.bip). This image is used for the NLLSSF method in calculating the surface-pressure elevation from the 760nm oxygen band. (Typically a 5x5 convolved version of the original hyperspectral image [real_image].)
image_file -	An PxMxN hyperspectral image in integer (2-byte) data format and band-interleaved-by-pixel (.bip). This image is used for the NLLSSF method in calculating the total columnar water vapor from the 940nm band.

The original NLLSSF by Green did not specify a convolved image for this module. If it is desired to retain the original NLLSSF, the same image file name as [real_image] may be used here. Otherwise, this file name should be possibly a 3x3, 5x5 or other convolved image that is derived from real_image. This option is included mainly in case the user finds it desirable to use a convolved image for an improved SNR.

real_image - An PxMxN hyperspectral image in integer (2-byte) data format and band-interleaved-by-pixel (.bip) used for inversion from sensor radiance to ground reflectance.

image_11x11_file - An PxMxN hyperspectral image in integer (2-byte) data format and band-interleaved-by-pixel (.bip). This image is used for the NLLSSF method in calculating the visibilty from a given aerosol type in the spectral range of 400-700nm. (Typically an 11x11 convolved version of the original hyperspectral image [real_image].)

spectral_rsp_file - A 2xP ascii data file defining the Gaussian spectral response function for each channel. The first column is the band center wavelength (in nanometers) and the second column is the Full-Width Half-Maximum of the Gaussian (in nanometers).

channels - P; the number of channels (bands in ENVI terms) in the hyperspectral image.

col M; the number of columns (samples in ENVI terms) in the hyperspectral image.

rows - N; the number of rows (lines in ENVI terms) in the hyperspectral image.

gain - The scalar needed to convert the integer (2-byte) digital count into floating point radiance units. (This value is

	usually defined in AVIRIS or HYDICE .gain files that are received with the images.) If gain value is not constant, see below under FILE INPUT and the file gain.dat. *NOTE: The program does expect a scalar value for this term even if you have a pre-determined "gain.dat" file. If the file gain.dat exists in the working directory, the program will use it for input and over-write the scalar value.
conversion_fac-	Floating point value to convert image radiance units to Watts/cm^2/sr/nm. For AVIRIS images: 0.001 For HYDICE images: 0.0001
LUTname-	Filename of the existing 3-D Look-Up Table with various atmospheric spectral radiometeric parameters generated by MODTRAN 4.0.
cst_elevation -	Integer value to select the method of surface elevation in the scene: -1 Set to default constant (truth or estimated surface elevation value in km contained in "surf_scene_info.dat") [Fast] 0 Run NLLSSF for surface-pressure depth, but do it once with an image-wide average. [Medium] 1 Run NLLSSF for surface-pressure depth for each pixel. [Slow]
wv_switch -	Integer value to select the method of extraction for columnar water vapor: 0 Set to default constant (truth or estimated total columnar water vapor amount) value in "wv_scene_info.dat". Total columnar water vapor is defined as the sum of the sun-target

and target-sensor vertical water columns in grams/cm^2. [Fast]

1 Run NLLSSF for columnar water vapor for each pixel. [Slow]

2 Run APDA for columnar water vapor for each pixel. [Medium]

use_rim_data - Integer value to select the method of determining atomspheric visibility:

-1 Set to default constant (truth or estimated visibility value for the aerosol type) in "aerosol_scene_info.dat" [Fast]

0 Run NLLSSF to derive visibility for each pixel. [Slow]

1 Use RIM method to derive visibility to be used for the whole scene. [Medium]

inv_selection - Integer value to select the radiative transfer equation to use when inverting from sensor radiance to ground reflectance. For a first run, this option MUST be set to 0 or -1. If it is desired that the adjacency effect in the radiative transfer equation use the average surround reflectance from a previous total inversion run (rho_avg_image.bip), total_inversion.pro can be run a second time with this option set to 1.

-1 Use the Big Equation without Lenv (this option may also be selected if the LUT was generated with a single scattering atmosphere model).

0 Lenv is included in the Big Equation (for use with a multiple scattering atmosphere model LUT only).

1 (Second pass ONLY) Make second pass through total_inversion.pro and invert to reflectance using the average reflectance of the surround and Lenv.

3.2 Files Needed for Program Input

'leaf_water.dat'	A 2xN ascii data file of reflectance for green grass.

The first column is wavelength in microns where the wavelength range is greater than that of spectral response file and the unit increment is 0.001 micron. The second column consists of the grass reflectance where the range of from 0 (no reflectance) to 1.0 (100% reflectance). *NOTE: This file should be an included part of the Total_Pkg directory.

'surf_scene_info.dat' The 2x3 ascii data file where the first column data are the starting values for the NLLSSF for: reflectance bias, reflectance gain, and the terrain elevation [km], respectively. The second column consists of the respective plus/minus range for each parameter.

'wv_scene_info.dat' The 2x4 ascii data file where the first column consists of starting values for NLLSSF for: reflectance bias, reflectance gain, scalar for liquid water vapor amount, and the total columnar water vapor amount in [g/cm^2], respectively. The second column consists of the respective plus/minus range for each parameter.

'aerosol_scene_info.dat' The 2x4 ascii data file where the first column data are starting values for NLLSSF for: reflectance bias, reflectance gain, scalar for liquid water vapor amount, and visibility in units of [km], respectively. The second column consists of the respective plus/minus range for each parameter.

3.3 Optional Files:

'gain.dat' - A 1xP column vector file containing the gain coefficients for each channel that is multiplied by the DC in the image to get radiance for each pixel. If this file does not exist, the gain is set to the required scalar value from the command line input. This file may be needed for sensors that have different gain factors due to separate spectrometers.

'classmap.bsq' -	If you are using the RIMAC option, it is required that the program find the file 'classmap.bsq'. If the file does not exist, the program 'm_class.pro' will do an unsupervised classification and create the class map file. If a different classification method than ISODATA in ENVI is wished to be used, the user must then create a class map (before running this inversion code) using the method of their choice and call the file 'classmap.bsq'. The inversion program will then find the user-created file and process it.

3.4 Outputs

If inv_selection=0 or inv_selection=-1 (First Pass)

'ModBE_wAdj.bip'	Spectral reflectance image where the reflectance of the surround was assumed to be the same as the target in the radiative transfer equation. Size: MxNxP
'ModBE_rho_av.bip'	If this is after the first pass through the algorithm and the atmospheric PSF has not yet been calculated, then this file is the spectral reflectance image derived from the input 11x11 convolved hyperspectral image. This image will be over-written when the Phase Function algorithm is invoked. This image is **required** input for a second run of total_inversion.pro when inv_selection=1.
'image_info2.bsq'	An MxNx12 image that contains solved parameters for each pixel in the hyperspectral image for the first pass through the algorithm. (See ENVI header at the end of total_inversion.pro for a description for each layer.)

'image_z.tif'	An MxN TIFF image representing a scaled monchromatic typographic map of the image scene.
'image_wv2.tif'	An MxN TIFF image representing a scaled monchromatic map of the atmospheric water vapor.

<u>If inv_selection=1 (Second Pass)</u>

'ModBE_wNew_Adj.bip'	Final spectral reflectance image where the average reflectance value of the target was used for the surround reflectance in the radiative transfer equation.
'*.*.hdr'	ENVI file headers for any of the previously mentioned reflectance images.
'image_info2_2ndpass.bsq'	An MxNx12 image that contains solved parameters for each pixel in the hyperspectral image for the 2nd pass through the algorithm. (See ENVI header at the end of total_inversion.pro for a description for each layer.)
'image_z.tif'	An MxN TIFF image representing a scaled monchromatic typographic map of the image scene.
'image_wv2.tif'	An MxN TIFF image representing a scaled monchromatic map of the atmospheric water vapor.

3.5 Optional Output

When building the carddeck, the program will ask if the user wishes to have amoeba iteration information output for one pixel position. If the user chooses yes [Y], then the IDL keywords SET_PIXEL_COL and SET_PIXEL_ROW are set. When set, all the information from EACH iteration in amoeba is output to the screen for this pixel position in the image. This information can be used for debugging purposes or to plot some of the data to see how well amoeba is fitting the feature curves. It is strongly suggested that you redirect this data into a file at the start of the program since it amoeba outputs a great deal of data.

Ex: If the total inversion carddeck is called inversion.cdk:

Enter at the command prompt:

```
idl<inversion.cdk>output_data.dat
```

Also, if you selected wv_switch=2, a file called 'mch.dat' and 'refch.dat' were created that contain a list of the array positions of the measurement channels and the reference channels, respectively. To find which channel wavelength these correspond to, simply type

```
nl –v0 name_of_spectral_response_file
```

and then the line numbers will correspond to the file numbers. The channel wavelengths should be within these constraints:

> For 'refch.dat', the first grouping should be for the atmospheric window before the 0.94µm water vapor absorption feature between 0.86 and 0.886µm. The second grouping (there are no spaces or gaps between the groupings) should be between 0.986 and 1.04µm for the atmospheric window after the 0.940µm water vapor feature.
>
> For 'mch.dat', the file numbers should correspond to wavelengths on the trough of the 0.94µm water absorption feature between 0.93 and 0.96µm.

If you have corrupted data (e.g. noisy bands, pattern noise, bad pixels) in ANY of these bands in your image, you need to edit those out of your images (and the .rsp file AND the LUT!).

3.6 Other Considerations:

For CIS users, your IDL_DIR variable must be set to the DIRS copy of IDL in order to enable the non-interactive ENVI calls. As of 7/8/99, you can change this by typing: setenv IDL_DIR /dirs/archs/rsi/idl_5 at the command prompt.

This set of programs contains Unix commands that are spawned from IDL as well as non-interactive ENVI calls. The non-interactive ENVI calls are only with the RIM option, but Unix commands are laced throughout the code. If you run on an OS **other** than Unix, you MUST go through the source code and see if you can make appropriate changes that work in that operating system. (Highly suggest a grep on the word "spawn" to see where the Unix calls are made.) No guarantees on this code if run on any other OS than Unix.

Also, make sure if you created your .bip images on a Sun, you use a Sun when you run total_inversion. If you created them on an alpha, make sure you run total_inversion on an alpha. The header files for the images are not read in to check the endian type. If you have images created on a different architecture than you are running this algorithm on, it is easier to run ENVI on the native architecture, take in the image, and write them out again. The other option is to use the “swap_endian.pro” routine in IDL in the source code to swap the endians for each of the input images, but this option is discouraged unless it is unavoidable.

In the event that amoeba does not converge for a pixel, you will see values of -1 in the information vector in image_info2.bsq at the same position. The program will not abort when this occurs, but the reflectance data (which will be bogus)will still be saved in image_info2.bsq.

4.0 Procedure

This is a suggested procedure to assist the user in running Total Inversion with a minimum of run-time mistakes that result in restarting the program. A sample Unix script is included in the Appendix to help the user along.

1) Create a working directory. Copy the entire contents of Total_Pkg, Phase_Pkg, and your default value MODTRAN 4.0 carddeck (the one that the LUT generation was based) into the working directory. Copy the MODTRAN_Phase folder and RIMAC folder into your working directory. Compile the code in each of the folders using the provided makefiles. Copy “rim” into the working directory from RIMAC.

2) Open the LUT in a text editor to determine the range and number of sensor channels that have radiometric parameters. Then inspect and change the .rsp file **and** all the images to be used to make sure the exact bands (that are in the LUT) are in each one. If one image or .if the .rsp file is different, the spectral misalignment will cause “ringing” by the absorption features in the resulting recovered reflectance cube.

3) Start IDL in your working directory and run the program “mk_total_inv_cddk.pro”. (There are no arguments for this procedure, but you should have a list from Section 2.0 of the pathnames to the needed files and images.) Answer all the questions at the prompt. Make sure the full pathnames of the images or files are typed in if those images or files are not found in the working directory. After the procedure is complete, a new file called “inversion.cdk” is created in the working directory (which the user may rename at their convenience).

4) Set up the default (truth or estimated) surface elevation, visibility, and columnar water vapor values in “surf_scene_info.dat” (1st column, 3rd row), “aerosol_scene_info.dat” (1st column, 4th row), and “wv_scene_info.dat” (1st column, 4th row), respectively. If you do not know the values, refer to the MODTRAN carddeck you copied into the working directory in step 1 or use the values supplied in the sample files.

5) For debugging purposes or to just get a data file to track amoeba as it does iterative fits on the absorption features, vi into total_inversion.pro and go a few lines down from where the procedure begins to where you see ‘set_pixel_row’ and ‘set_pixel_col’. If you set the row and column of one pixel of interest in the image you are working on, the fit data will print to the screen (or may be redirected into a file). Remember that these variables are array indices, so you have to subtract 1 from the actual row and column numbers when you set the values for ‘set_pixel_row’ and ‘set_pixel_col’.

6) Because this program has non-interactive ENVI calls, you must run with the DIRS version of IDL. To do this, simply set the IDL_DIR environment variable with this command: setenv IDL_DIR /dirs/archs/rsi/idl_5.

7) Now you should be ready to run the first pass by typing at the prompt:

```
idl<inversion.cdk>debug.data
```

(See step 5 for a description of the redirect into debug.data.)

8) When the first run is complete and you wish to do the second pass through the algorithm, you may opt to run the Phase Function programs that generate the new rho_average_image and over-writes the image

created during the first pass. The user at this point may also choose to just use rho_average image from the first pass which is a smoothed version of the ModBE_wAdj.bip (with an 11x11 averaging kernel). To get the atmospheric PSF weighted rho average image made, you must start by editing the file 'idl_script2' which is included as a sample. The first argument for the "mk_rho_avg_image.pro" program is the instantaneous field of view (IFOV) of the sensor in milliradians. The second argument is the name of the MODTRAN 4.0 carddeck you copied into the directory in step 1. The third argument is the name you wish the new MODTRAN 4.0 carddeck that this program creates. The fourth argument is the filename (full path name) of the spectral response file.

9)..Start the phase program by typing: idl<idl_script2 . The program will create a new MODTRAN 4.0 carddeck with the information from image_info2.bsq, run a special MODTRAN 4.0 routine to extract the scattering phase function data, and then convolves the first pass reflectance image with the spectral kernels (or scaled atmospheric PSFs). The output is a reflectance cube called "ModBE_rho_av.bip". (This output over-writes the file of the same name created at the end of the first pass.)

10) When step 9 is completed, simply put inversion.cdk into a text editor and change the second to last entry (the last numerical entry) from0 or –1 to a 1. Then run this slightly changed inversion.cdk through the algorithm again: idl<inversion.cdk>debug_2ndpass.data At the end of the program, a reflectance cube called "ModBE_wNew_Adj.bip" is created which is the second pass estimation of the ground reflectance.

5.0 Appendix

5.1 Sample Script

```
Script started on Fri Jul 16 11:09:41 1999

Yes, Master [201] % Yes, Master [201] % mkdir Def_cr050
Yes, Master [202] % cp Total_Pkg/*  Def_cr050
Yes, Master [203] % mkdir Old
Yes, Master [204] % mkdir New
Yes, Master [205] % cp ../Total_Pkg/* Old
Yes, Master [206] % cp ../Total_Pkg/* New
Yes, Master [207] % cp /dirs/home/lcs3555/Phase_Func/Phase_Pkg_Execute/* Old
Yes, Master [208] % cp /dirs/home/lcs3555/Phase_Func/Phase_Pkg_Execute/* New
Yes, Master [209] % cd Old
Yes, Master [210] % idl
IDL Version 5.0.3 (OSF alpha). Research Systems, Inc.
Installation number: 10230-0.
Licensed for use by: The Digital Imaging and Remote Sensing Lab

For basic information, enter "IDLInfo" at the IDL> prompt.

IDL> mk_total_inv_cddk
% Compiled module: MK_TOTAL_INV_CDDK.
This IDL program constructs an input carddeck for the total
radiometric inversion to ground reflectance algorithm "total_inversion.pro".

NOTE: Before this step is executed, make sure that the bands in
      your LUT correspond EXACTLY to those in the image(s).
      (e.g. if your LUT only includes bands 5-15, then your
       .bip images should only have bands 5-15.


Enter the name of the .bip image to be used for the 760nm
oxygen band surface-pressure depth NLLSSF algorithm.
By Greens example, this image is usually a 5x5 convolved
version of the original.
: /dirs/home/lcs3555/Western_Rainbow/cr15m50/old_cr15m50_5x5_crppd.bip

Enter the name of the .bip image to be used for the 940nm
water vapor band NLLSSF algorithm.  This option is included
in the case that the signal-to-noise ratio needs improvement
from the original image.  This may be a 5x5 kernel or greater
convolved image from the original.  If no improvement in SNR is
needed, simply enter the name of the original .bip image.
: /dirs/home/lcs3555/Western_Rainbow/cr15m50/old_cr15m50_5x5_crppd.bip

Enter the name of the .bip image for inversion from sensor
radiance to ground reflectance.
: /dirs/home/lcs3555/Western_Rainbow/cr15m50/old_cr15m50_crppd.bip

Enter the name of the .bip image to be used for the 400nm-700nm
NLLSSF algorithm.  This image is typically an 11x11 convolved
version of the original.
```

```
: /dirs/home/lcs3555/Western_Rainbow/cr15m50/old_cr15m50_11x11_crppd.bip

Enter the name of the spectral response file.
NOTE: this file must be a two column array with the first column
     the center wavelength of the band in nm and the second
     column the FWHM in nm.  The number of rows must correspond
     EXACTLY to the number and placement of the bands in the image.
: /dirs/home/lcs3555/Western_Rainbow/cr15m50/hydice_cr15m50_crppd.rsp

Enter the number of columns in the image:50

Enter the number of rows in the image:50

Enter the number of channels:209

Enter the channel gain term to convert image DC to radiance:75.0

Enter the conversion factor to convert radiance to Watts/cm^2/sr/nm:0.0001

Enter the name of the Look-Up
Table:/dirs/home/rvrpci/yuma/new_yuma_cr15m50/new_yuma_cr15m50.rsp.lut

If the elevation of the scene to be:
         Set to default constant (value in "surf_scene_info.dat"); Enter -1
     Constant over the scene, but have NLLSSF figure it out from
     the scene average pixel; Enter 0
     Calculated by NLLSSF for each pixel; Enter 1
: -1

Selection for calculating aerosol visibility:
         Set to default constant (value in "aerosol_scene_info.dat")
         Enter -1
         Use NLLSSF to derive the aerosol visibility;
         Enter 0
         Use the RIM method to derive the aerosol visibility;
         Enter 1
: -1

Selection for columnar water vapor calculation:
         Set to default constant (value in "wv_scene_info.dat")
         Enter 0
         Use NLLSSF to derive the columnar water vapor;
         Enter 1
         Use APDA to derive the columnar water vapor;
     Enter 2
: 0

Selection to use average reflectance in Big Equation (1-S*rho_average)
NOTE:  This option MUST be set to 0 or -1 for any first run!!
          On the first run, total_inversion.pro will make an 11x11
          convolved reflectance image.  If you wish a second run to
          use rho_av; Enter 1
         Otherwise, Enter 0 if you wish Lenv in the Big Equation
     Enter -1 to use a Big Equation without Lenv.
: 0
```

```
Enter the name of the LUT .config file.
: /dirs/home/rvrpci/yuma/new_yuma_cr15m50/new_yuma_cr15m50.conf

IDL> exit

Yes, Master [211] % setenv IDL_DIR /dirs/archs/rsi/idl_5
Yes, Master [212] % idl<rtcr050>junk

IDL Version 5.0.3 (OSF alpha). Research Systems, Inc.
Installation number: 10230-0.
Licensed for use by: The Digital Imaging and Remote Sensing Lab

For basic information, enter "IDLInfo" at the IDL> prompt.

% Compiled module: TOTAL_INVERSION.
% Compiled module: FIND_BANDPASSES_FOR_NLLSSF.
% Compiled module: PRO_CONV_REFL.
% Compiled module: READ_AEROSOL_ELEVATION_WATER_VAPOR_DATA.
% Compiled module: STRIP_OUT_COMMENTS.
% Compiled module: ELEVATION_WATER_SERIES_GIVEN_AEROSOL.
% Compiled module: ELEVATION_SERIES_GIVEN_A_WATER_VAPOR.
% Compiled module: INTERPOLATE_WATER_VAPOR_SERIES.
% Compiled module: INTERPOLATE_ELEVATION_SERIES.
% Compiled module: WATER_VAPOR_SERIES_GIVEN_AN_ELEVATION.
% Compiled module: INVERT_TO_REFLECTANCE.
% Compiled module: CREATE_DYNAM_TIFF.
% Compiled module: LINFIT.
% Compiled module: WRITE_TIFF.
% Program caused arithmetic error: Floating divide by 0
% Program caused arithmetic error: Floating underflow
% Program caused arithmetic error: Floating illegal operand

Yes, Master [213] % idl<idl_script2

IDL Version 5.0.3 (OSF alpha). Research Systems, Inc.
Installation number: 10230-0.
Licensed for use by: The Digital Imaging and Remote Sensing Lab

For basic information, enter "IDLInfo" at the IDL> prompt.

% Compiled module: MK_RHO_AVG_IMAGE.
% Compiled module: MOMENT.
avg_vis=      70.0000
avg_elevation=      265.009
avg_water_vapor=     0.801049
% Compiled module: MAKE_NEW_CARDDECK_FROM_ORIGINAL.
ML & locator=      33       0
   0.00142450

Digital Imaging and Remote Sensing Lab
MODTRAN 4.0
A beta-version developed by Lee Sanders
     (lcs3555@cis.rit.edu) for phase function
      information extraction.
```

```
cond_tape10    5252
/dirs/home/lcs3555/Western_Rainbow/cr15m50/hydice_cr15m50_crppd.rsp     209
     50     50    209
% Compiled module: M_CONVERT.
% Compiled module: FILEPATH.
% Compiled module: STR_SEP.
% Restored file: ENVI_UTL.
exit m_convert

Yes, Master [216] % cp rtcr050 rtcr050b
Yes, Master [217] % vi rtcr050b
total_inversion,
'/dirs/home/lcs3555/Western_Rainbow/cr15m50/old_cr15m50_5x5_crppd.bip',
'/dirs/home/lcs3555/Western
_Rainbow/cr15m50/old_cr15m50_5x5_crppd.bip',
'/dirs/home/lcs3555/Western_Rainbow/cr15m50/old_cr15m50_crppd.bip', '/d
irs/home/lcs3555/Western_Rainbow/cr15m50/old_cr15m50_11x11_crppd.bip',
'/dirs/home/lcs3555/Western_Rainbow/cr15m50/h
ydice_cr15m50_crppd.rsp',    50,        50,       209,  75.0000,        0.000100000,
'/dirs/home/rvrpci/yuma/new_yu
ma_cr15m50/new_yuma_cr15m50.rsp.lut',     -1,            -1,       0,         0,
'/dirs/home/rvrpci/yuma/new_yuma_cr15m
50/new_yuma_cr15m50.conf'
~






~  [H  [53B"rtcr050b" 1 line, 606 characters  [

Yes, Master [220] % idl<rtcr050b>junk_2ndpass

IDL Version 5.0.3 (OSF alpha). Research Systems, Inc.
Installation number: 10230-0.
Licensed for use by: The Digital Imaging and Remote Sensing Lab

For basic information, enter "IDLInfo" at the IDL> prompt.

% Compiled module: TOTAL_INVERSION.
% Compiled module: FIND_BANDPASSES_FOR_NLLSSF.
% Compiled module: PRO_CONV_REFL.
% Compiled module: READ_AEROSOL_ELEVATION_WATER_VAPOR_DATA.
% Compiled module: STRIP_OUT_COMMENTS.
% Compiled module: ELEVATION_WATER_SERIES_GIVEN_AEROSOL.
% Compiled module: ELEVATION_SERIES_GIVEN_A_WATER_VAPOR.
% Compiled module: INTERPOLATE_WATER_VAPOR_SERIES.
% Compiled module: INTERPOLATE_ELEVATION_SERIES.
% Compiled module: WATER_VAPOR_SERIES_GIVEN_AN_ELEVATION.
% Compiled module: INVERT_TO_REFLECTANCE.
% Compiled module: CREATE_DYNAM_TIFF.
% Compiled module: LINFIT.
% Compiled module: WRITE_TIFF.
```

```
% Program caused arithmetic error: Floating divide by 0
% Program caused arithmetic error: Floating underflow
% Program caused arithmetic error: Floating illegal operand
Yes, Master [221] % exit
Yes, Master [222] %
script done on Fri Jul 16 17:27:31 1999
```

8. References

Bohren, C., Huffman, D., *Absorption and Scattering of Light by Small Particles*, Wiley and Sons, (1983).

Bruegge, C.J., Conel, J.E., Margolis, J.S., Green, R.O., Toon, G., Carrere, V., Holm, R.G., and Hoover, G., “In-situ Atmospheric Water-Vapor Retrieval in Support of AVIRIS Validation”, *Imaging Spectroscopy of the Terrestrial Environment, SPIE Vol. 1298*, pp. 150-163, (1990).

Clark, R.N., and Roush, T.L., “Reflectance Spectroscopy: Quantitative Analysis Techniques for Remote Sensing Applications”, *Journal of Geophysical Research*, **89**, 6329-6340, (1984).

Clark, R.N., Swayze, G.A., Gallagher, A., Gorelick, N., and Kruse, F., “Mapping with Imaging Spectrometer Data Using the Complete Band Shape Least-Squares Algorithm Simultaneously Fit to Multiple Spectral Features from Multiple Materials”, *Proceedings of the Third Airborne Visible/Infrared Imaging Spectrometer (AVIRIS) Workshop, JPL Publication 91-28*, pp. 2-3, (1991).

Clark, R.N., King, T.V.V., Ager, C., and Swayze, G.A., “Initial Vegetation Species and Senescence/Stress Mapping in the San Luis Valley, Colorado Using Imaging Spectrometer Data”, *Proceedings of the Summitville Forum ‘95, Colorado Geological Survey Special Publication 38*, pp. 64-69, (1995).

Crippen, R. E., "The Regression Intersection Method of Adjusting Image Data for Band Ratioing", *International Journal of Remote Sensing*, **8**, No. 2, pp. 137-155, (1986).

Diner, D.J., Martonchik, J.V., “Influence of Aerosol Scattering on Atmospheric Blurring of Surface Features”, *IEEE Transactions on Geoscience and Remote Sensing*, **Ge-23**, pp. 618-624, (Sept. 1985).

Diner, D.J., Abdou, W.A., Ackerman, T.P., Conel, J.E., Gordon, H.R., Kahn, R.A., Martonchik, J.V., Paradise, S.R., Wang, M., West, R.A*., MISR: Level 2 Algorithm Theoretical Basis: Aerosol/Surface Product, Part1 (Aerosol Parameters), JPL Publication D-11400, Rev.A*, (December 1, 1994).

Feng, X., “Design and Performance of a Modular Imaging Spectrometer Instrument”, *Rochester Institute of Technology Dissertation*, (1995).

Fraser, R.S., Kaufman, Y.J., “The Relative Importance of Aerosol Scattering and Absorption in Remote Sensing”, *IEEE Transactions on Geoscience and Remote Sensing*, **Ge-23**, No. 5, pp. 625-633, (1985).

Gao, B., Heidebrecht, K.B., Goetz, F.H., “Derivation of Scaled Surface Reflectances from AVIRIS Data”, *Remote Sensing of Environment*, **44**, pp. 165-178, (1993).

Gao, B.C., Goetz, A.F.H., Westwater, E.R., Conel, J.E., and Green, R.O., “Possible Near-IR Channels for Remote Sensing Precipitable Water Vapor from Geostationary Satellite Platforms”, *Journal of Applied Meteorology*, **32**, p1794, (1993).

Goetz, A.F.H., Rowan, L.C., and Kingston, M.J., “Mineral Identification From Orbit: Initial Results from the Shuttle Multispectral Infrared Radiometer”, *Science*, **218**, pp.1020-1024, (1982).

Goetz, A.F.H., Vane, G., Solomon, J.E., Rock, B.N., “Imaging Spectrometry for Earth Remote Sensing”, *Science*, **228**, no 4704, pp. 1147-1153, (1985).

Green, R.O., Carrére, V., and Conel, J.E., “Measurement of Atmospheric Water Vapor Using the Airborne Visible/Infrared Imaging Spectrometer”, *American Society of Photogrammetry and Remote Sensing*, Workshop Image Processing, Sparkes, Nevada, (1989).

Green, R. O., Conel, J. E, Margolis, J. S., Bruegge, C. J., Hoover, G. L., An Inversion Algorithm for Retrieval of Atmospheric and Leaf Water Absorption from AVIRIS Radiance with Compensation for Atmospheric Scattering”, *Proceeding of the Third Airborne Visible/Infrared Imaging Spectrometer (AVIRIS) Workshop, JPL Publication 91-28*, pp. 51-61, (1991b).

Green, R. O., Roberts, D. A., Conel, J. E, “Estimation of Aerosol Optical Depth, Pressure Elevation, Water Vapor, and Calculation of Apparent Surface Reflectance from Radiance Measured by the Airborne Visible/Infrared Imaging Spectrometer Using a Radiative Transfer Code”, *SPIE Vol. 1937*, *Imaging Spectrometry of the Terrestrial Environment*, pp. 2-11, (1993).

Green, R. O., Roberts, D. A., Conel, J. E, “Characterization of the Atmosphere for the Inversion of AVIRIS Calibrated Radiance to Apparent Surface Reflectance”, *Summaries of the Sixth Annual JPL Airborne Earth Science Workshop*, **1**, (March 4, 1996).

Halthore, R.N., Markham, B.L., Ferrare, R.A., and Aro, T.O., “Aerosol Properties Over the Midcontinental United States”, *Journal of Geophysical Research*, **97**, No. D17, pp. 18769-18778, (1992).

Horvath, H., Kasahara, M., and Pesava, P., “The Size Distribution and Composition of the Atmospheric Aerosol at a Rural and Nearby Urban Location”, *Journal of Aerosol Science*, **27**, No. 3, pp. 417-435, (1996).

Kastner, C. J., “In-Flight Absolute Radiometric Calibration of the Landsat Thematic Mapper”, *University of Arizona Ph.D. Dissertation*, (1985).

Kaufman, Y. J., Wald, A. E., Remer, L. A., Gao, B., Li, R., and Flynn, L., "The MODIS 2.1μm Channel - Correlation with Visible Reflectance for Use in Remote Sensing of Aerosol", *IEEE Transactions on Geoscience and Remote Sensing*, **35**, No. 5, pp. 1286-1298, (1997).

King, M.D., Byrne, D.M., Herman, B.M., and Reagan, J.A., “Aerosol Size Distributions Obtained by Inversion of Spectral Optical Depth Measurements”, *Journal of Atmospheric Science*, **35**, pp. 2153-2167, (1978).

La Baw, C., “Airborne Imaging Spectrometer II: The Optical Design”, *SPIE Vol. 834*, Imaging Spectroscopy II, pp. 16-21, (1987).

Martonchik, J.V., Diner, D.J., “Retrieval of Aerosol Optical Properties from Multi-Angle Satellite Imagery”, *IEEE Transactions on Geoscience and Remote Sensing*, **30**, No. 2, pp. 223-230, (March, 1992).

Martonchik, J.V., “Determination of Aerosol Optical Depth and Land Surface Directional Reflectances Using Multi-angle Imagery”, (Not Yet Published), (1996).

Otterman, J, and Fraser, R.S., "Adjacency Effects on Imaging by Surface Reflecation and Atmospheric Scattering: Cross Radiance to Zenith", Applied Optics, **18**, No. 16, pp. 2852-2860, (1979).

Parameswaran, K., Rose, K.O., and Krishna Murthy, B.V., “Relationship Between Backscattering and Extinction Coefficients of Aerosols with Application to Turbid Atmosphere”, *Applied Optics*, **30**, No. 21, pp. 3059-3071, (1991).

Pieters, C.M., and Englert, P.A.*, Remote Geochemical Analysis: Elemental and Mineralogical Composition*, Cambridge University Press, New York, (1993).

Porter, W. M. and Enmark, H. T., “A System Overview of the Airborne Visible/Infrared Imaging Spectrometer (AVIRIS)”, *SPIE Vol. 834*, Imaging Spectroscopy II, pp. 22-31, (1987).

Press, W.H., *Numerical Recipes in C: The Art of Scientific Computing*, pp. 408-412, Cambridge University Press, (1992).

Reinersman, P.N. and Carder, K.L., "Monte Carlo Simulation of the Atmospheric Point-Spread Function with an Application to Correction for the Adjacency Effect", *Applied Optics*, **34**, No. 21, pp. 4453-4471, (1995).

Rickard, L. J., “HYDICE: An Airborne System for Hyperspectral Imaging”, *SPIE Vol. 1937*, Imaging Spectrometry of the Terrestrial Environment, pp. 173-179, (1993).

Shettle. E.P., Fenn, R.W., *Models for the Aerosols of the Lower Atmosphere and the Effects of Humidity Variations on their Optical Properties*, Air Force Geophysics Laboratory, Publication No. AFGL-TR-79-0214, Hanscom AFB, Massachusetts, (1979).

Schläpfer, D., Borel, C., Keller, J., and Itten, K., “Atmospheric Pre-Corrected Differential Absorption Technique to Retrieve Columnar Water Vapor”, *Summaries of the Sixth Annual JPL Airborne Earth Science Workshop*, **1**, (March 4, 1996).

Schott, J. R., *Remote Sensing: The Image Chain Approach*, Oxford University Press, (1997).

Tanré, D., Deroo, C., Duhaut, P., *et al*., *Simulation of the Satellite Signal in the Solar Spectrum (5S), User's Guide*, Laboratoire d'Optique Atmospherique, U.S.T. de Lille, 59655 Villeneuve d'ascq, France, (1986).

Vane, G., Green, R. O., Chrien, T. G., Enmark, H. T., Hansen, E. G, and Porter, W. M., "The Airborne Visible/Infrared Imaging Spectrometer (AVIRIS)", *Remote Sensing of Environment*, **44**, pp.127-143, (1993).

Van de Hulst, H.C., *Light Scattering by Small Particles*, John Wiley, NY, (1957).

Vermote, E., Tanré, D., Deuzé, J. L., Herman, M., and Morcrette, J. J., *Second Simulation of the Satellite Signal in the Solar Spectrum (6S)*, 6S User Guide Version 1, (1997).